A Facile Synthesis and Application of Protein-Shelled Microbubbles as Temperature-Responsive Drug Carriers with the Aid of a Poly(N-isopropylacrylamide)-block-(acrylic acid) Shell

by

Xiaochen Ma

A thesis submitted in partial fulfillment of the requirements for the degree of

Master of Science

in
Chemical Engineering

Department of Chemical and Materials Engineering
University of Alberta

Abstract

In this study, a novel synthesis of proteinaceous microbubbles (MBs) was introduced in an effort to substantially lengthen the short lifetime of the sonochemically-synthesized microbubbles using surface-treated proteins. Bovine serum albumin (BSA) as a representative protein, was treated with 2-iminothiolane hydrochloride (the Traut's reagent) to convert surface amines to thiols before the synthesis of microbubbles. At a moderate high molar excess of the Traut's reagent, a roughly bimodal size distribution of MBs was shown, concentrated at 0.5 and 2.5 μm. The 0.5 μm portion quickly vanished while the 2.5 μm portion gradually shrank to ~850 nm in ~3 days, stabilized at this size at 4 °C for several months. The 20 times molar excess of the Traut's reagent to BSA was determined to be the optimal reaction ratio because of the largest long-lived portion and the greatest shell thickness of the produced MBs. Characterizations of MBs by Fourier transform infrared (FTIR) spectroscopy and X-ray photoelectron spectroscopy (XPS) showed the presence of free amines and thiols remaining on the surface of MBs. The reactivities of these functional groups were demonstrated by either electrostatically interacting with the alumina and the silica surfaces or chemically bonding with the gold surface in quartz crystal microbalance with dissipation monitoring (QCM-D) measurements. To demonstrate the potential of being utilized as drug carriers, MBs were used to load a demo drug, doxorubicin (Dox) electrostatically. To optimize the loadings of Dox onto MBs, their loading efficiencies were systematically compared using UV/Vis and fluorescence spectrophotometer, by varying the presence of the pre-coated gold nanoparticles (AuNPs), pH, dosages of MBs, temperature, and time. A temperature-sensitive polymer, poly(N-isopropylacrylamide-block-acrylic acid) (poly(NIPAM-b-AAc), was used to encapsulate the Dox-loaded MBs to prevent any premature

release of the loaded Dox. With a fine-tuned lower critical solution temperature (LCST) of 39 °C, the Dox-loaded MBs with a poly(NIPAM-b-AAc) shell exhibited a temperature-responsive switch that initiated the release of Dox from ~20% to ~90% when the temperature was elevated 37 to 39 °C in in-vitro release testing (IVRT). On the other hand, the shell-free carriers, such as Dox-loaded MBs, Dox-loaded AuNPs-coated MBs, did not show such a temperature response. The further kinetic study of the Dox-loaded MBs with a poly(NIPAM-b-AAc) shell revealed that the release of Dox followed the Korsmeyer-Peppas model, governed by the Fickian diffusion and the conformational change of the polymer shell.

Preface

Chapter 4 of this thesis was published in *Ultrasonics Sonochemistry* as "Ma, X., Bussonniere, A., & Liu, Q. (2017). A facile sonochemical synthesis of shell-stabilized reactive microbubbles using surface-thiolated bovine serum albumin with the Traut's reagent. *Ultrasonics Sonochemistry*, *36*, 454-465". I was responsible for the data collection, the data analysis, and the composition for all the manuscript except for the acoustic characterization section. Bussonniere, A. contributed to the acoustic characterization section and Liu, Q. was the supervisory author providing the essential guidance of the work.

Chapter 5 of this thesis was accepted for publication to the *Colloids and Surfaces B: Biointerfaces* journal as "Ma, X., Liu, Q. Preparation of poly(N-isopropylacrylamide)-block-(acrylic acid)-encapsulated proteinaceous microbubbles for delivery of doxorubicin". I was responsible for the data collection, the data analysis, and the manuscript composition. Liu, Q. was the supervisory author providing the concept formation.

Chapter 4 was presented both at 2016 Faculty of Engineering Graduate Research Symposium and at the Canadian Centre for Clean Coal/Carbon and Mineral Processing Technologies (C^5MPT) at University of Alberta.

Chapter 4 and part of Chapter 5 were presented at 2016 Leeds Microbubble Consortium in Leeds, England, United Kingdom.

Acknowledgements

I would like to extend my sincere gratitude to my research supervisor, Prof. Qingxia (Chad) Liu, for his continued guidance and support throughout my course of research. The impact of his help has well exceeded the scope of my research project and deeply changed my way of thinking for my future career and life. It has been my greatest honor to be his student for the past two years.

I would like to thank Dr. Adrien Bussonniere for his efforts completing the acoustic characterizations of my synthesized MBs during the late stage of my work.

I would like to express my appreciation to all the colleagues from C^5MPT for all their support and assistance.

I would like to thank Nathan Gearin, Ni Yang, Shihong Xu, and Anqiang He for their training and technician work for my project. Without their continued efforts, I could not have gone through my research project smoothly.

I would also like to acknowledge the financial support from both C^5MPT and the Natural Sciences and Engineering Research Council of Canada (NSERC).

Table of Contents

List of Figures

Abbreviations

MBs	Microbubbles
BSA	Bovine serum albumin
BSA-SH	Surface-thiolated bovine serum albumin
BSA-SH MBs	Microbubbles synthesized using surface-thiolated bovine serum albumin

Dox	Doxorubicin
DTT	Dithiolthreitol
Poly(NIPAM-b-AAc)	Poly(N-isopropylacrylamide)-block-(acrylic acid)
AFE	Air-filled emulsion
FTIR	Fourier transform infrared spectroscopy
XPS	X-ray photoelectron spectroscopy
FE-SEM or SEM	Field emission scanning electron microscope
TEM	Transmission electron microscope
QCM-D	Quartz crystal microbalance with dissipation monitoring
EDTA	Ethylenediaminetetraacetic acid
PBS	Phosphate buffered saline
RCF	Relative centrifugal force
ATR	Attenuated total reflectance
DRIFTS	Diffuse reflectance infrared Fourier transmission spectroscopy
ABX	Automated beamsplitter exchange
MMI	Multi-modal imaging
DLS	Dynamic light scattering
CLSM	Confocal laser scanning microscope
IVRT	In-vitro release testing
LCST	Lower critical solution temperature

List of symbols

E_b	Bulk modulus of the shell, mN/m^2
σ	The interfacial tension between the air and solution, mN/m
R	The radius of MBs, μm
d	The shell thickness of MBs, nm
ΔP	The Laplace pressure, atm
ΔV_{Shell}	The volume change of the shell
α_{att}	The attenuation coefficient, dB/cm
D	The sample-containing cell width, cm
$V_{protein}$	The absorption of protein solution, mV
$V_{microbubble}$	The absorption of microbubble solution, mV
M_t/M_f	The percentage of the released payload at time t, %
n	The release exponent
K_{KP}	The release rate constant for the Korsmeyer-Peppas kinetic model
T	Time, mins
K_0	The release rate constant for the zero kinetic model
K_1	The release rate constant for the first kinetic model
K_H	The release rate constant for the Higuchi kinetic model

Chapter 1 Introduction

1.1 Background

Bubbles with a typical size range of 1 to 10 μm have been known as microbubbles (MBs) [1, 2]. With a large surface area and a variety of surface properties, MBs have been extensively studied and prevalently used for many applications in the fields of medical, food, and water treatment. The pressure difference originated from the curved surface of MBs, known as the Laplace pressure, often drives the entrapped gas diffuse into the liquid phase. A stabilizing shell made of proteins, lipids, or polymers, has been therefore adopted to enhance the stability and the lifetime of MBs. For the air-filled proteinaceous MBs, efforts have been made previously by other researchers to either physically or chemically denature proteins before the synthesis of MBs. However, the physical denaturation does not result in any appreciable increase in the lifetime while the chemical denaturation only works for certain types of proteinaceous MBs. As a result, a facile, universal synthesis of stable proteinaceous MBs is required for various applications involving MBs.

1.1.1 Classification of microbubbles (MBs)

To stabilize MBs, a shell is frequently needed to entrap the gas inside the core, and different types of shell materials (Figure 1.1) have been utilized for this purpose such as proteins, surfactants, lipids, polymers, and polyelectrolyte multilayers [3-6]. Different shell materials render various surface properties and functionalities to MBs [4]. Protein-shelled MBs have a

relatively rigid shell composed of native and denature proteins [7]. Different proteins have been utilized to assemble the shells of MBs because of the amphipathic nature of proteins. Surfactants, well known for their role of reducing surface tension, have also been used for synthesizing MBs. Depending on the method of synthesis, surfactants-shelled MBs are more stable through insonication than agitation [4, 8]. Lipids-shelled MBs, commercially known as Difinity and Sonovue [4, 9], endow a well-orientated monolayer as a stabilizing shell. The stability of lipids-shelled MBs comes from the low surface tension and the highly adhesive monolayer resulting from hydrophobic and van der Waals interactions [10]. Polymer-shelled MBs have also been

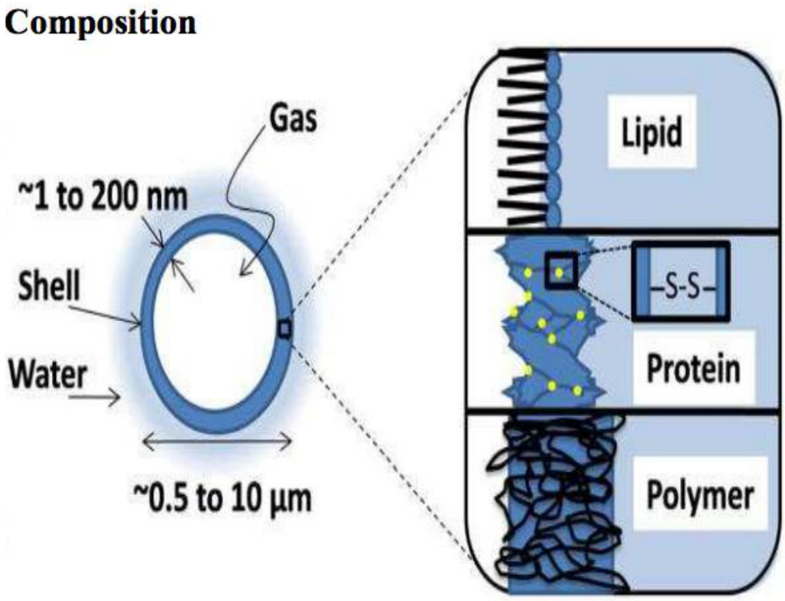

Figure 1.1 Composition of microbubbles with different types of shell materials [3]

extensively studied by many researchers because they are more resistant to compression and expansion than proteins- or lipids-shelled MBs [3, 4]. Polyelectrolytes-coated MBs, on the other hand, have frequently been adopted for layer-by-layer deposition of either drug payloads or

biological molecules [11, 12]. In the meantime, the stability of MBs and the number of deposited molecules could be dramatically increased as the number of layers goes up.

1.1.2 General utilizations of MBs

With large surface areas and tunable surface functionalities, MBs have been widely used in many different fields such as clinical applications [13-21], food industries [22, 23], and water treatment [24, 25]. For clinical applications, the construct of MBs renders an excellent echogenicity and therefore primarily used as an ultrasound contrast-enhancing agent [13-15, 15-21]. With the presence of the gas core, MBs emit and reflect sound waves upon the ultrasound treatment; in the meantime, tissues and bones have a very limited acoustic response. As a result, MBs are capable of exclusively producing an acoustic response and used to enhance the imaging signals for clinical purposes. Also, MBs have been considered to be one of the most promising chemotherapeutic agents when loaded with drug payloads (Figure 1.2) [17, 18, 21, 26]. A non-invasive and theranostic approach using MBs can be advantageous. In detail, non-invasive approaches are particularly meaningful for brain cancers where a traditional surgery is typically difficult to perform [21]. Theranostic approaches, defined as the coupling of therapeutic with diagnostic agents, enables the diagnosis and the drug administration at the same time [18, 21]. In the field of food industries, MBs have been used to substitute traditional preservative and enhanced the shelf life of food [22, 23]. Depending on the shell material, MBs can be rendered antimicrobial and antibacterial resistance, which make them favorable for their uses in

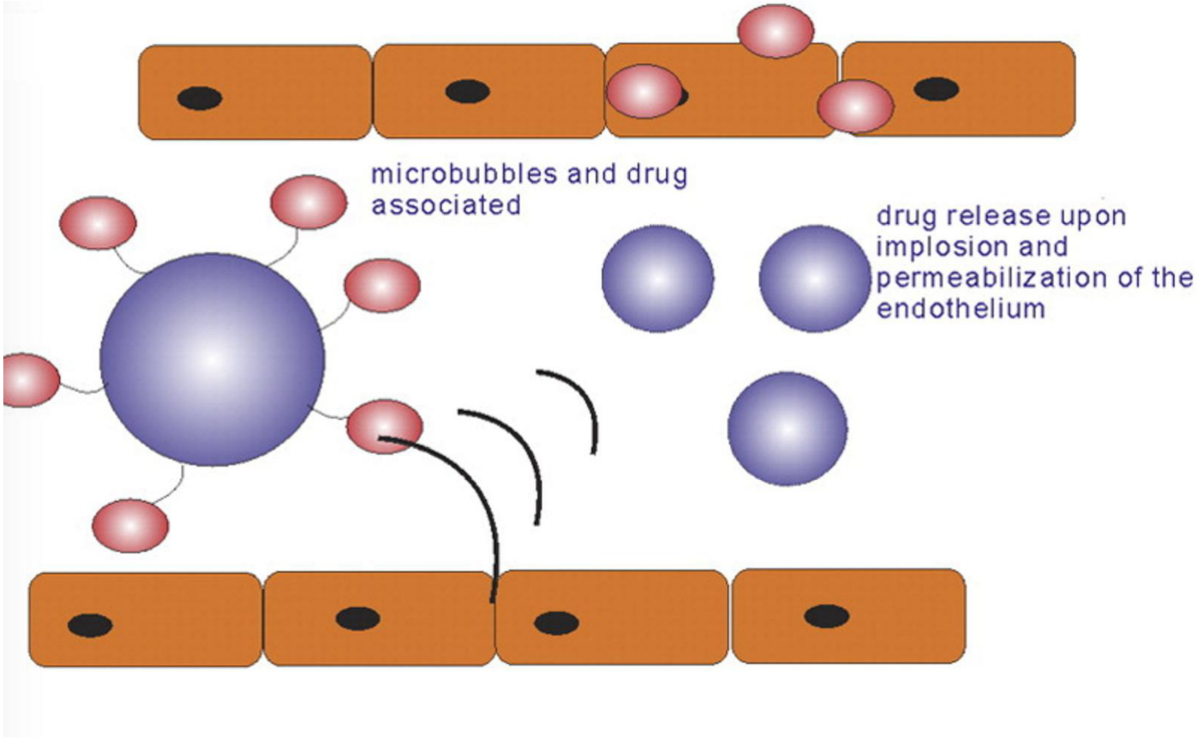

Figure 1.2 A schematic of the drug-loaded MBs releasing the drug upon ultrasonic radiation[26]

the food industry. In water treatment, ultrasonic radiation of microbubbles produces a vast number of free radicals which can efficiently decompose organic compounds [21, 25].

1.1.3 Challenges of MBs

Although MBs are considered as a promising agent in many fields, one of the key challenges of expanding their usages has been their short lifetime and instability [27, 28]. For proteinaceous MBs, physical denaturation by heating was proved to be inadequate to maintain the subsequently synthesized MBs [29, 30]. Chemical reductants such as dithiolthreitol (DTT) was used to partially loosen up the protein structure in order to synthesize stable protein-shelled MBs [29-31]. The role of DTT was to reduce the internal disulfide bond to external thiols, available for

later formation of the cross-linkers in MBs. However, the treatment of proteins with the chemical reductants was only effective to certain types of proteins that intrinsically have abundant disulfide bond. For example, lysozyme with a large number of disulfide bonds buried inside can be used to synthesize stable MBs after treated by DTT. However, the most of other proteins with limited internal disulfide bonds cannot be used to stabilize MBs when treated by DTT in advance [31].

1.2 Objectives

The short lifetime of air-filled proteinaceous MBs has been the major problem hindering their applications. Although many types of proteinaceous MBs have been reported in the literature, they are frequently case-specific and only applicable to certain proteins. As a result, the need for a universal, facile method of synthesis has been emphasized. The main objectives of the current study are listed as following:

1. To demonstrate the synthesis of stable proteinaceous MBs using surface-treated bovine serum albumin (BSA).

2. To characterize the synthesized MBs using various surface characterization techniques.

3. To probe the surface reactivity of the synthesized MBs using the QCM-D test.

4. To demonstrate the usage of the synthesized MBs as a drug carrier using doxorubicin (Dox) as a representative chemotherapeutic agent.

5. To optimize the loading of Dox onto MBs under various conditions.

6. To study the drug retention and release of Dox-loaded MBs with and without an outer encapsulating shell.

1.3 References

[1] Maske, S.K., et al., *INTERNATIONAL JOURNAL OF PHARMACY & LIFE SCIENCES.* Int. J. of Pharm. & Life Sci.(IJPLS), 2012. **3**(12): 2228-2235.

[2] Geers, B., et al., *Crucial factors and emerging concepts in ultrasound-triggered drug delivery.* Journal of controlled release, 2012. **164**(3): 248-255.

[3] Dayton, P., et al., *Acoustic radiation force in vivo: a mechanism to assist targeting of microbubbles.* Ultrasound in medicine & biology, 1999. **25**(8): 1195-1201.

[4] Forsberg, F., W.T. Shi, and B. Goldberg, *Subharmonic imaging of contrast agents.* Ultrasonics, 2000. **38**(1): 93-98.

[5] Sirsi, S. and M. Borden, *Microbubble compositions, properties and biomedical applications.* Bubble Science, Engineering & Technology, 2009. **1**(1-2): 3-17.

[6] Christiansen, J.P., et al., *Targeted tissue transfection with ultrasound destruction of plasmid-bearing cationic microbubbles.* Ultrasound in medicine & biology, 2003. **29**(12): 1759-1767.

[7] Klibanov, A.L., *Ligand-carrying gas-filled microbubbles: ultrasound contrast agents for targeted molecular imaging.* Bioconjugate chemistry, 2005. **16**(1): 9-17.

[8] Christiansen, C., et al., *Physical and biochemical characterization of Albunex, a new ultrasound contrast agent consisting of air-filled albumin microspheres suspended in a solution of human albumin.* Biotechnology and applied biochemistry, 1994. **19**(3): 307-320.

[9] Dressaire, E., et al., *Interfacial polygonal nanopatterning of stable microbubbles.* Science, 2008. **320**(5880): 1198-1201.

[10] Thomsen, H., *Contrast Media in Ultrasonography Basic Principles and Clinical Applications.* 2005.

[11] Duncan, P.B. and D. Needham, *Test of the Epstein-Plesset model for gas microparticle dissolution in aqueous media: Effect of surface tension and gas undersaturation in solution.* Langmuir, 2004. **20**(7): 2567-2578.

[12] Borden, M.A., et al., *DNA and polylysine adsorption and multilayer construction onto cationic lipid-coated microbubbles.* Langmuir, 2007. **23**(18): 9401-9408.

[13] Ferrara, K.W., M.A. Borden, and H. Zhang, *Lipid-shelled vehicles: engineering for ultrasound molecular imaging and drug delivery.* Accounts of chemical research, 2009. **42**(7): 881-892.

[14] Blomley, M. and D. Cosgrove, *Microbubble echo-enhancers: a new direction for ultrasound?* The Lancet, 1997. **349**(9069): 1855-1856.

[15] Cosgrove, D., *Echo enhancers and ultrasound imaging.* European journal of radiology, 1997. **26**(1): 64-76.

[16] Calliada, F., et al., *Ultrasound contrast agents: basic principles*. European journal of radiology, 1998. **27**: S157-S160.

[17] Lentacker, I., et al., *Ultrasound-responsive polymer-coated microbubbles that bind and protect DNA*. Langmuir, 2006. **22**(17): 7273-7278.

[18] Ferrara, K., R. Pollard, and M. Borden, *Ultrasound microbubble contrast agents: fundamentals and application to gene and drug delivery.* Biomedical Engineering, 2007. **9**.

[19] Qin, S., C.F. Caskey, and K.W. Ferrara, *Ultrasound contrast microbubbles in imaging and therapy: physical principles and engineering*. Physics in medicine and biology, 2009. **54**(6): R27.

[20] Yang, F., et al., *Superparamagnetic iron oxide nanoparticle-embedded encapsulated microbubbles as dual contrast agents of magnetic resonance and ultrasound imaging*. Biomaterials, 2009. **30**(23): 3882-3890.

[21] Park, J.I., et al., *Microbubbles loaded with nanoparticles: a route to multiple imaging modalities.* Acs Nano, 2010. **4**(11): p. 6579-6586.

[22] Kiessling, F., et al., *Ultrasound microbubbles for molecular diagnosis, therapy, and theranostics.* Journal of nuclear medicine, 2012. **53**(3): 345-348.

[23] Ishikawa, H., et al., *Inactivation of Bacillus spores by the supercritical carbon dioxide micro-bubble method.* Bioscience, biotechnology, and biochemistry, 1997. **61**(6): 1022-1023.

[24] Kobayashi, F., et al., *Inactivation of Escherichia coli by CO2 microbubbles at a lower pressure and near room temperature.* Transactions of the ASABE, 2009. **52**(5): 1621-1626.

[25] Suslick, K.S., *Sonochemistry.* science, 1990. **247**(4949): 1439-1445.

[26] Xu, Q., et al., *A comparative study of microbubble generation by mechanical agitation and sonication.* Innovative Food Science & Emerging Technologies, 2008. **9**(4): 489-494.

[27] Epstein, c.e.P. and M.S. Plesset, *On the Stability of Gas Bubbles in Liquid-Gas Solutions.* The Journal of Chemical Physics, 1950. **18**(11): 1505-1509.

[28] Kloek, W., T. van Vliet, and M. Meinders, *Effect of bulk and interfacial rheological properties on bubble dissolution.* Journal of Colloid and Interface Science, 2001. **237**(2): 158-166.

[29] Cavalieri, F., et al., *Ultrasonic synthesis of stable, functional lysozyme microbubbles.* Langmuir, 2008. **24**(18): 10078-10083.

[30] Cavalieri, F., et al., *Antimicrobial and biosensing ultrasound-responsive lysozyme-shelled microbubbles.* ACS applied materials & interfaces, 2013. **5**(2): 464-471.

[31] Vong, F., et al., *A comparison of the physical properties of ultrasonically synthesized lysozyme-and BSA-shelled microbubbles.* Ultrasonics sonochemistry, 2014. **21**(1): 23-28.

Chapter 2 Literature Review

2.1 Advantages and disadvantages of MBs

The usage of MBs has been reported to be advantageous for several reasons. For clinical applications, the primary usage of MBs has been concentrated in imaging for their echogenicity, biocompatibility, and cost-effectiveness. Tissues and blood inside human bodies are similar in echogenicity, and as a result, it is very challenging to differentiate the interface between tissue and blood [1-3]. MBs, on the other hand, are capable of reflecting ultrasound waves and producing unique signals that are easy to detect [2-5]. The shell materials of MBs are highly bio-friendly and bio-recognizable, frequently selected from naturally-occurring proteins, lipids and biocompatible polymers [1, 5-7]. In practice, MBs used in ultrasound produce the sonographic images much more cost-effectively than other alternative molecular imaging modalities, such as magnetic resonance imaging (MRI), positron emission tomography (PET), and single-photon emission computed topography (SPECT) [1][6]. Due to their advantages, MBs have also been considered as one of the most promising theranostic agents in drug delivery where imaging and drug-releasing are coupled [7-9]. Drug payloads can be loaded onto or into the surface of MBs frequently through antigen-antibody pairing. Different amplitudes or frequency of ultrasound waves can be used to image the area of interest and to trigger the release of the loaded drug subsequently. Driven by this combined concept of theranostic approaches, much research work has been proposed to design and optimize the construct of drug-loaded MBs [10-13]. However, MBs used in medical fields still face tremendous disadvantages. Low circulation residence times have been the key problem hindering the utilizations of MBs [1, 14, 15]. As a result, efforts have

been made to extend the lifetime of MBs in-vivo, to reduce their interaction with cells and organs, and to govern their destruction in a more controllable way [1, 29, 38]. For instance, a layer of polyethylene glycol (PEG) has frequently been adopted to enhance adhesion when the interaction between cell and MBs is repulsive and suppress adhesion when their interaction is

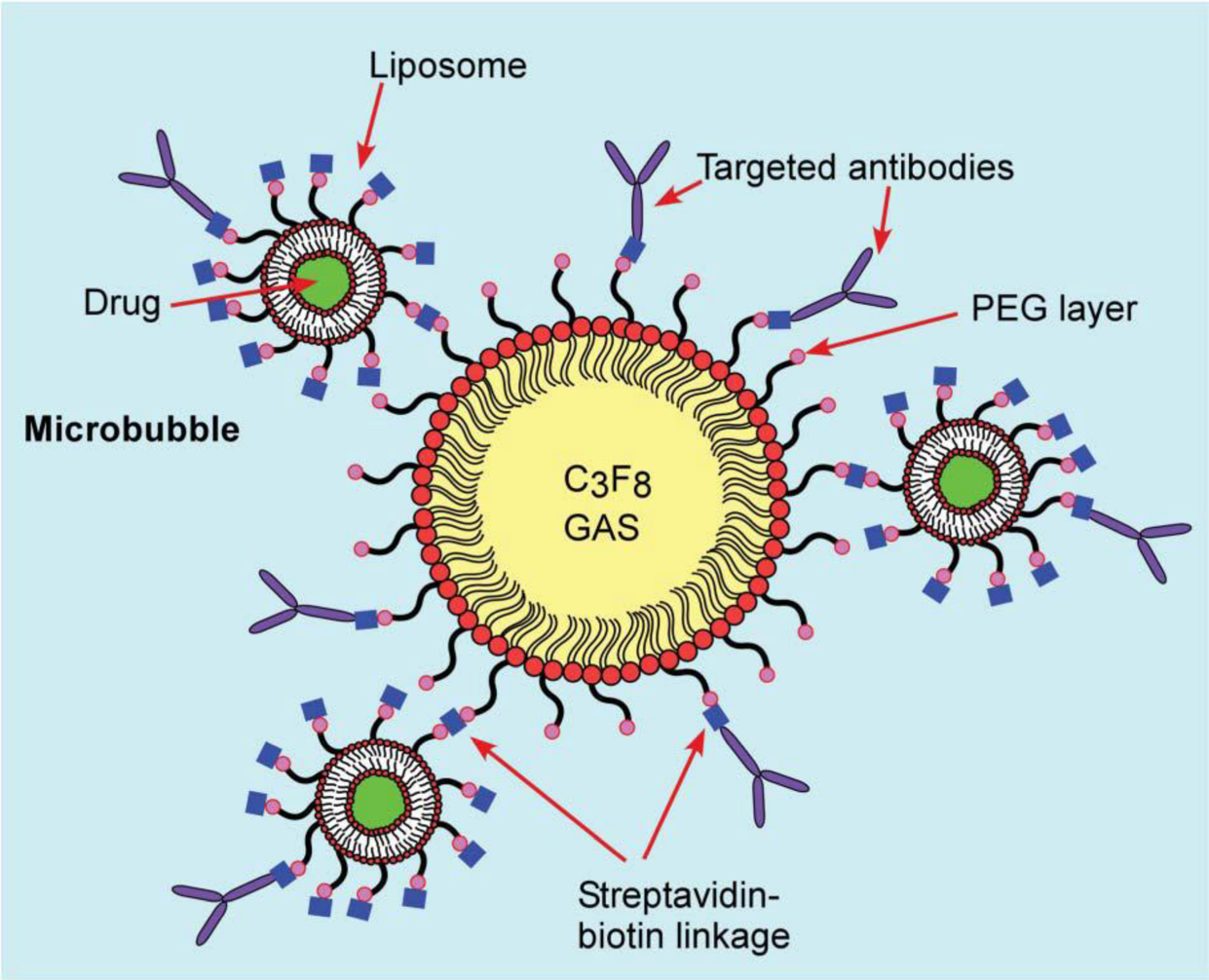

Figure 2.1 A schematic representing perfluorocarbon-entrapped MBs with drug loaded through a streptavidin-biotin linkage [16].

attractive [16]. The coating of PEG act as a buffering zone that enables MBs more resistance to the cellular environment; however, they can be still taken up by the liver or immune system cells [1]. Besides, the burst of MBs upon ultrasound radiation causes cellular and vascular damages, and as a result, many researchers have been conducting studies on the cellular interaction with MBs under different conditions [17, 18]. For water purification, MBs are preferably used to remove metal ions from dilute solutions [19]. Also known as the air-filled emulsion (AFE), MBs generated using sonication technique have a high affinity for different metal ions because of the presence of amino, amide, and carboxylic groups on the surface of MBs [19]. However, a much thorough study needs to carry out for different metal ions under various conditions. Physical and chemical adsorptions are always both contributable to ion adsorption with MBs. The stability and functionality of MBs make them a favorable candidate in collecting ions; however, the costs of MBs and the removal efficiency needs to be balanced when applied on an industrial scale.

2.2 Methods of MBs synthesis

2.2.1 Synthesis of MBs using co-axial electrodynamic atomization

Co-axial electrodynamic microbubbling has been one of the novel methods of synthesizing monodispersed MBs [20, 21]. Two concentrically placed syringe needles were used to simultaneously pump out different materials, normally being the stabilizing coating and the entrapped gas (Figure 2.2). For the MBs formation, any gas of interest is pumped through the inner needle and the coating liquid is injected through the outer needle. Three modes are reported

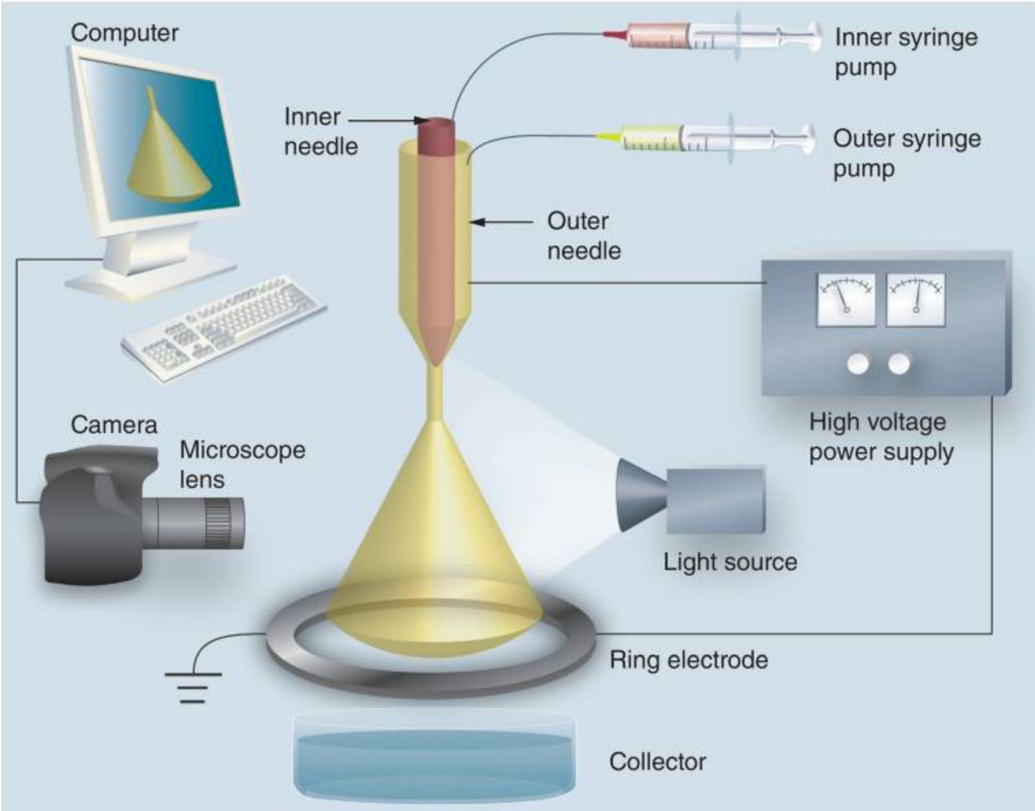

Figure 2.2 Schematic representation of co-axial electrodynamic atomization [21]

to be associated with the synthesis of MBs, and they are dripping, conning, and microbubbling modes. In detail, during the first stage of dripping, the flowing gas is entrapped by the flowing coating liquid at the orifice, generating macroscopic bubbles that are comparable to the size of the outer needle (Figure 2.2). Then, the conning mode can be reached when the high voltage source is applied to the system. The inclusion of a high voltage source attached to the co-axial needles produces a focusing effect that reduces the size of the synthesized bubbles to the range of microns [20, 21]. However, the MBs generated at this stage are not uniform in their size distribution. Further increase in the voltage drives the process into the microbubbling stage, where monodispersed MBs start to be synthesized. Governed by the magnitude of the high

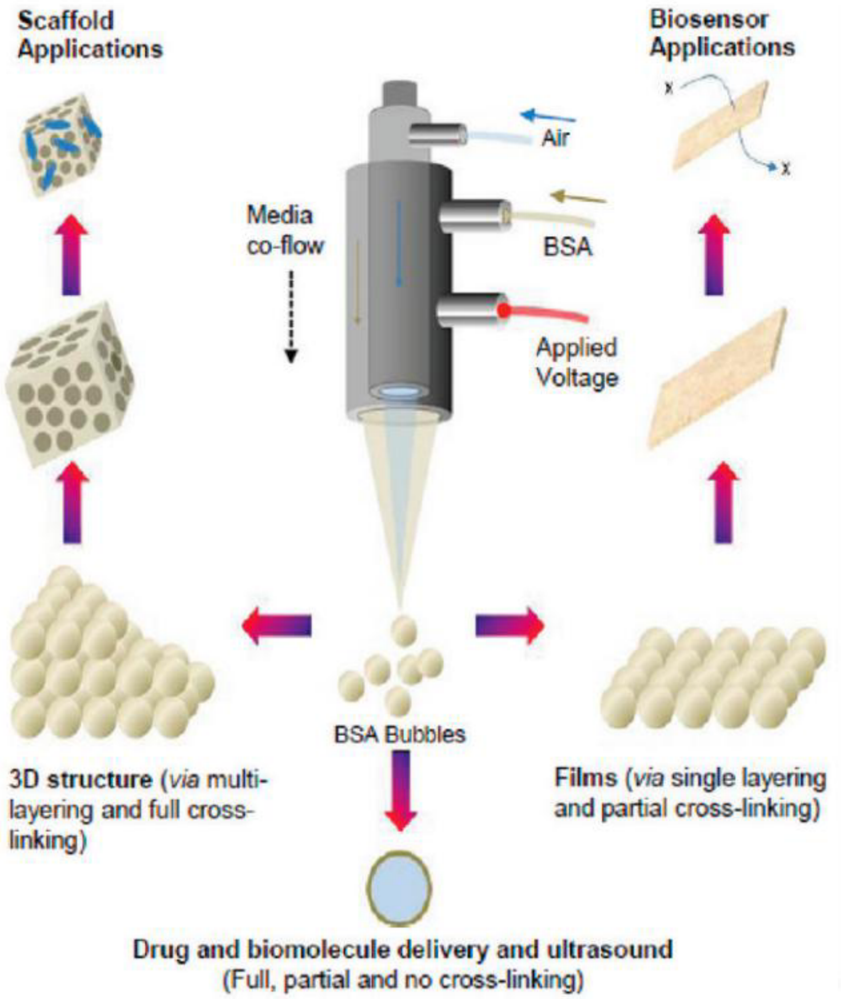

Figure 2.3 Generation of MBs using co-axial electrodynamic microbubbling [22]

voltage source, the size of the synthesized MBs can be manipulated by changing the parameters of the experimental setup such as the flow speed of air and the coating material, the size of the inner and the outer syringes, and the magnitude of the applied voltage [22]. After the MBs formation, cross-linkers have been frequently adopted to assemble the bubbles into a 2D membrane or a 3D scaffold (Figure 2.3). In spite of the capabilities of producing the monodispersed MBs and further incorporating them into 2D or 3D structures, the method of co-

axial electrodynamic microbubbling has major disadvantages. One of the them is the instability associated with the system. Any electrostatic changes in the environment interfere with electric field in the system and therefore hinder the continued production of fine, monodispersed MBs [22]. In addition, the instability of the synthesized MBs is another problem. The implementation of the high voltage source only physically reduces the size of bubbles to the range of micron; however, the produced MBs are easily collapsed after the synthesis without using cross-linkers in the collection media. In other words, the stable, free-form MBs are difficult to obtain while the MBs-incorporated 2D membrane or 3D scaffold becomes more suitable using this approach.

2.2.2 Synthesis of MBs using Mechanical agitation

Mechanical agitation can be effective synthesizing lipids-coated MBs [23, 24]; however, for proteinaceous MBs, other means of stabilizations have to be used along with mechanical mixing or shaking [25, 26]. Air has a much higher solubility than perfluorocarbon, and therefore, the substitution of using air as the gas core with perfluorocarbon can greatly reduce the gas diffusion and enhance the stability of MBs. It's also subtle to choose proteins that have a large area of the hydrophobic portion (Figure 2.4a, red portion) as the stabilizing shell. Mechanical agitation provides a high shear force that anneal proteins together; in other words, proteins with an easily accessible, a large hydrophobic area are particularly needed for this purpose. When air is used as the entrapped gas, an amorphous structure is often produced because of the inefficient treatment of mechanical agitation (Figure 2.4). When perfluorocarbon gas is used instead, MBs of a

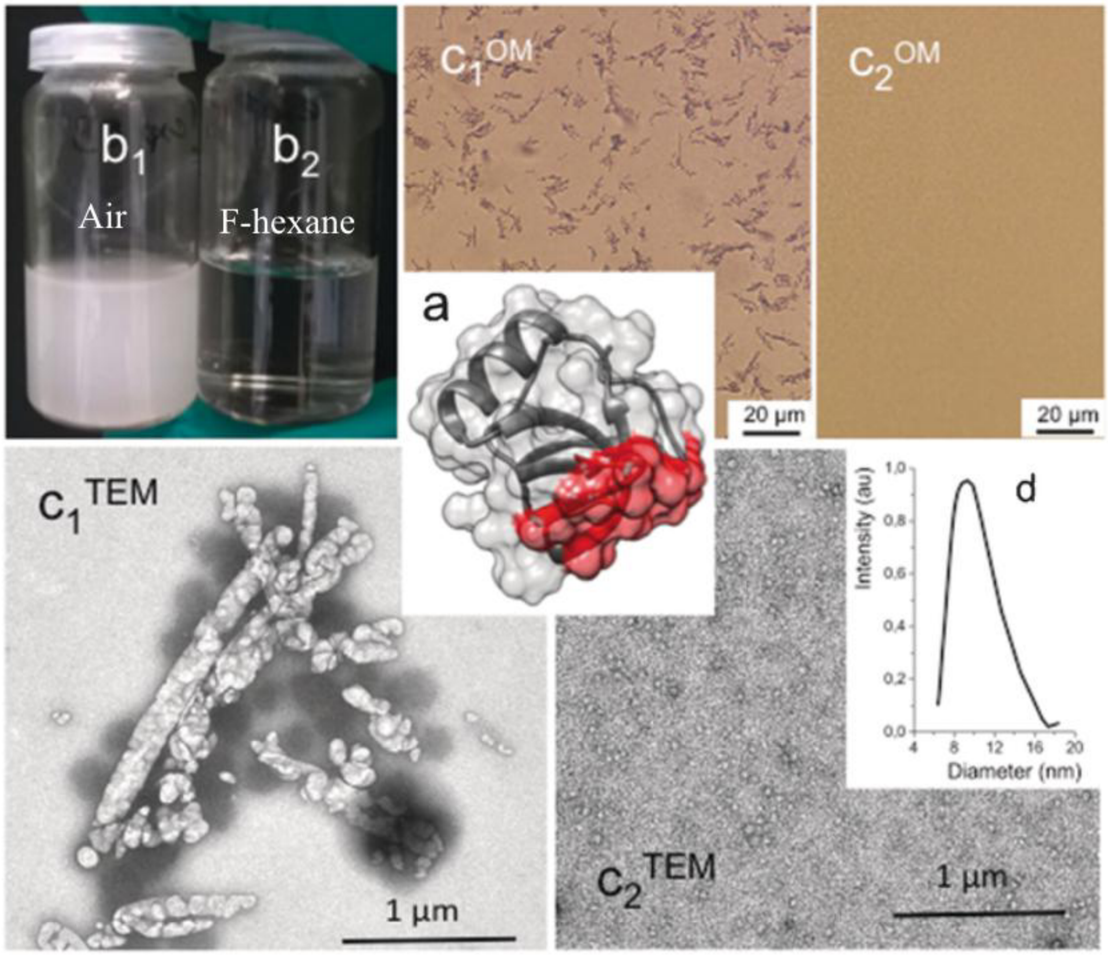

Figure 2.4 With air and F-hexane, MBs (b_2, C_2^{OM}, and C_2^{TEM}) and amorphous structures (b_1, C_1^{OM}, and C_1^{TEM}) were generated through mechanical agitation, where OM and TEM stand for optical and transmission electron micrographs [25].

relatively monodispersed size distribution is observed after the mechanical mixing (Figure 2.4). Another way of stabilizing the mechanically-synthesized proteinaceous MBs is to use solid nanoparticles to reduce the gas diffusion. Over time, the solid nanoparticles on the stabilizing shell can adopt a more compact form and strengthen the rigidity of MBs. In addition to the improved stability, the inclusion of solid nanoparticles can also render the optical tunablity to MBs, which is favorable for multimodal imaging and biosensing [26]. However, the necessary

utilization of other means of stabilizations reveals the limited selection of proteins and the inadequate treatment of mechanical agitation to synthesize proteinaceous MBs.

2.2.3 Synthesis of MBs using ultrasonic radiation

Ultrasonic radiation of proteinaceous solution produces both emulsification and cavitation [27, 28]. Emulsification produced by ultrasonic radiation was similar to that by vortex, but emulsification alone is not sufficient producing stable, long-lived MBs (Figure 2.5a). The presence of oxygen is another important factor determining the synthesis of MBs; in detail, with the presence of air, MBs can be successfully produced while oxygen-free environment cannot produce MBs in any appreciable amount (Figure 2.5a). To further investigate the mechanism of the cavitation process, superoxide dismutase, N-ethylmaleimide, and glutathione have been used to remove superoxide, cysteine, and free radicals, respectively in proteinaceous solution. When

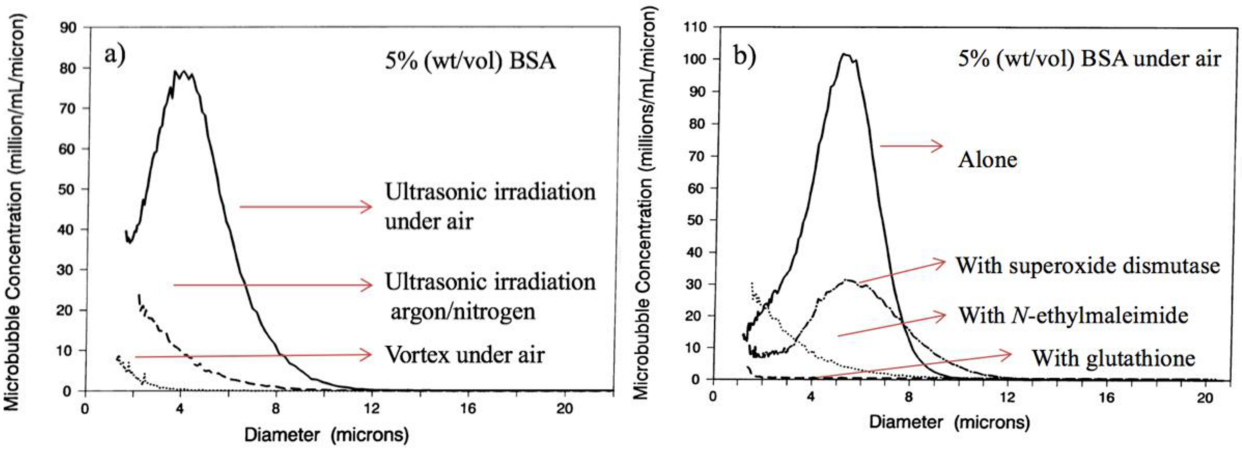

Figure 2.5 Comparison of synthesizing MBs under different situation (a) and with different chemicals suppressing the oxidants produced in ultrasonic radiation (b) [29].

superoxide, free radicals, and cysteine residues are depleted, no MBs can be formed, and their important roles are demonstrated (Figure 2.5b). The ultrasonic radiation generates a large number of free radicals, and these free radicals subsequently form superoxide, further oxidizing cysteine residues on proteins to disulfide bonds [29].

As mentioned above, the presence of cysteine is critical and therefore has been extensively studied in an effort to stabilize proteinaceous MBs. To increase the surface presence of cysteine groups, also known as the thiol groups, efforts have been made to either physically or chemically denature proteins in order to expose the internal disulfide bonds to external free thiols. Heat denaturation is a well-known process to loosen up the protein structure; however, the internal buried disulfide bond is relatively insensitive to heat shock [30]. Albeit being mostly denatured after the heat treatment, proteins adsorbed onto the air-water interface are held together primarily by hydrophobic and Van deer Waals forces. Without the presence of cross-linkers, the formed MBs can be easily collapsed at any time. Chemical denaturation using reductants, on the other hand, can be very effective reducing the internal disulfide bonds to external free thiols [15, 31, 32]. It has been reported that the degree of cross-linking is controlled by two factors, the extent of chemical reduction and of the sonication [15, 33]. A higher concentration of reductants or a longer reaction of denaturation results in a higher degree of the protein denaturation and therefore a higher degree of cross-linked network [15]. However, a lower cross-linking degree can also contribute to the stability of MBs; in other words, a relatively loose cross-linked network can also be stabilized by forming multilayers of proteins during the sonication process [15]. In addition to the degree of chemical denaturation, the magnitude and length of sonication also contribute to the stability of MBs. Higher power (> 120 W) and longer time (> 50 s) result

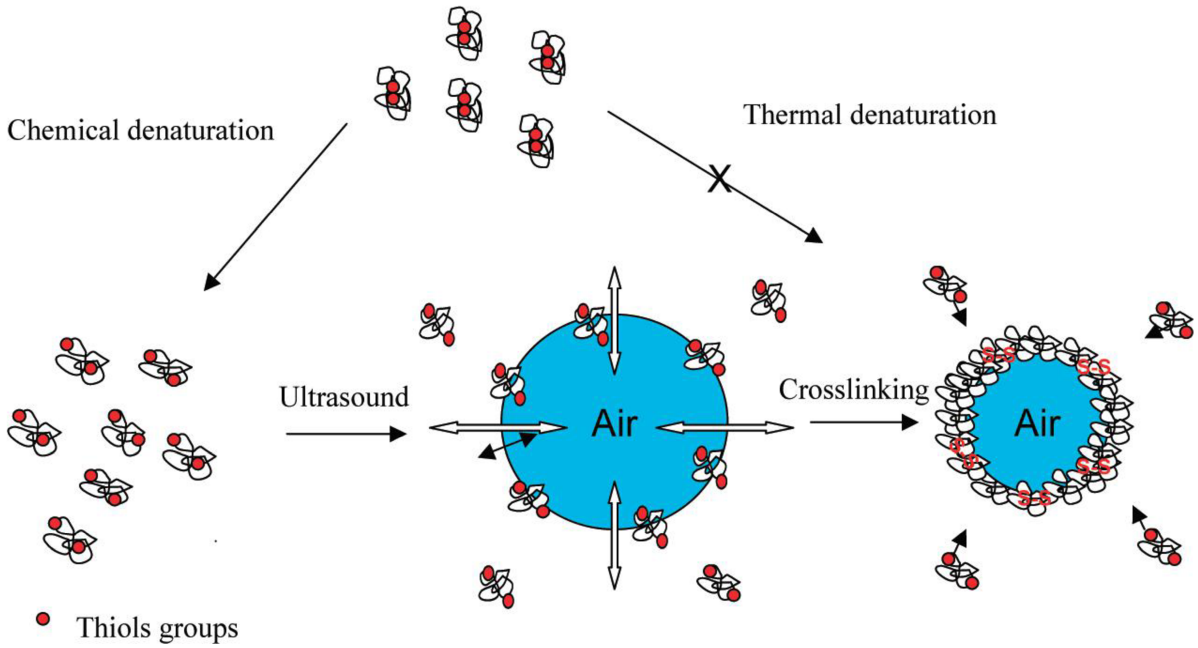

Figure 2.6 Schematic representation of partially denatured proteins cross-linked onto the shell of air-entrapped MBs [15].

in MBs with fragments because of the excessively strong shear force [33]. On the other hand, a lower amplitude of sonication radiation generates a lower yield of MBs. As a result, optimization of synthesizing proteinaceous MBs using disulfide-rich proteins has been systematically conducted by others [15, 31, 33]. However, a key drawback of this chemical denaturation prior to the MBs synthesis is the heavy dependence of the disulfide-rich proteins [32]. If a protein does not have sufficient number of internal disulfide bond, then this approach would not work. In addition, the utilization of reducing agents excessively loosens up the protein quaternary and tertiary structure, inevitably resulting in some changes in functionality of proteins. More problematically, the reduced form of proteins tends to have an overall lowered hydrophobicity which reduces the rigidity of the subsequently cross-linked shell and disfavors the stability of the synthesized MBs [34]. So, as reported in the literature, lysozyme-shelled MBs were successfully

stabilized when lysozyme was treated with DTT while the synthesized BSA-shelled MBs were still short-lived using the same approach.

2.3 Applications of MBs

2.3.1 Clinical imaging

The gas bubbles of a micron size act as an ideal reflector for the ultrasound, allowing the detection and characterization of cardiovascular abnormalities [10, 35]. The utilization of MBs enables non-invasive imaging which heavily relies on the reception of the reflection or backscattering of the sound wave at a particular range of frequency [10]. The stabilizer-shelled

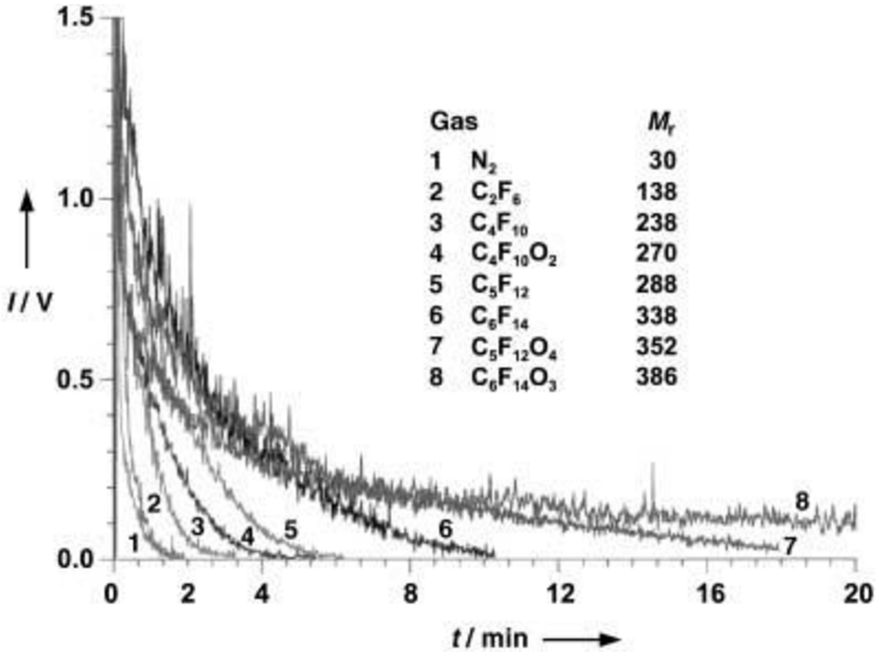

Figure 2.7 Comparison of the ultrasound signal decay with the filling gas in the MBs of the different molecular weight [36].

MBs always show a great compressibility resulted from the entrapped gas [37]. At a moderate acoustic power, MBs undergo oscillation in the acoustic field where they are compressed and expanded. The oscillation of MBs results in the generation of strong acoustic response much greater than the backscattered ultrasound response in acoustic impedance [10]. The compressibility of MBs is dependent on many factors such as the gas, the viscosity, and density of the surrounding media [38]. It was observed that perfluorocarbon gases of higher molecular weights showed an increased bubble persistence; in other words, as the molecular weights of the filling gas increases, a longer time of bubble persistence in the acoustic field is observed (Figure 2.7). At a high amplitude of acoustic power, MBs can be destroyed by outward diffusion of the gas, large shell defects, or the fragmentation of MBs [39]. In other words, different amplitudes of acoustic power result in different types of ultrasound cavitation. Non-inertial cavitation refers to the stable bubble oscillation with the gas entrapped inside throughout the compression and expansion [40]. As the ultrasound intensity increases, MBs move into the inertial or transient cavitation where they instantly collapse and locally generate high pressures and temperatures [40]. At the sufficient high ultrasound intensity, the backscattered sound waves produced by MBs give the initial source of the image; in addition, the super-harmonics and sub-harmonics of the incident sound waves greatly improve the resolution and contrast [41]. Echoes from cells and tissues are only a reflection of the transmitted frequency (Figure 2.8a) while those from MBs are at the second harmonic frequency (Figure 2.8b). As a result, the harmonic imaging is very useful for differentiating the MBs-containing regions and the MBs-free regions [35]. To further improve the sensitivity, the pulse-inversion technique has frequently been adopted, and it refers to the delivery of two pulses in proximity with one pulse 180° out of phase from the other

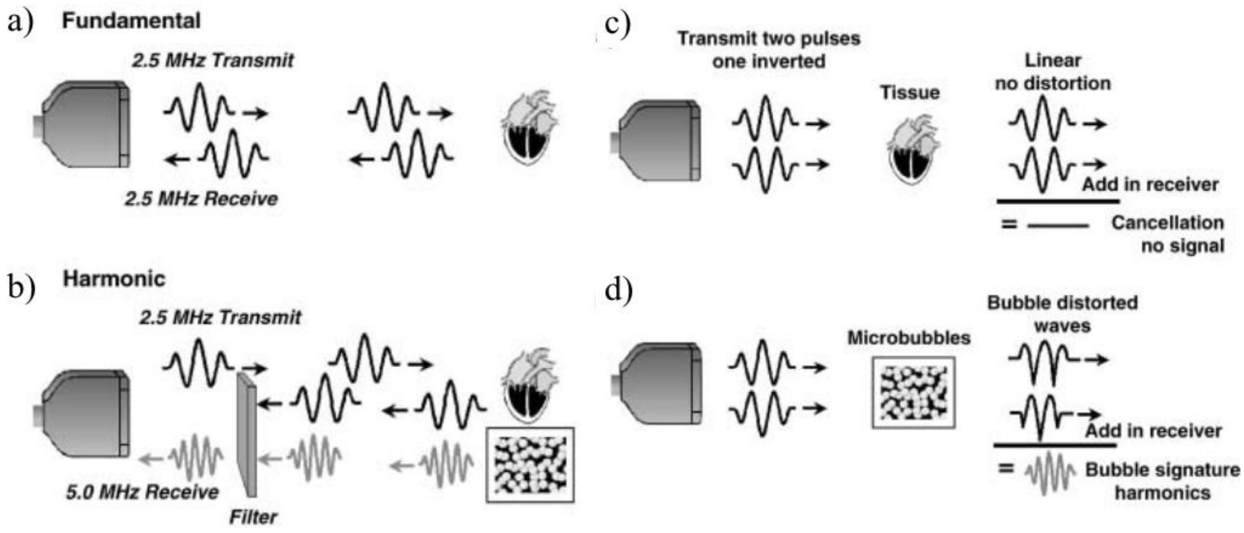

Figure 2.8 As an ultrasound contrast agent, MBs can produce fundamental (a) and harmonic (b) modes of imaging (d) that can be differentiated with the acoustic response of tissue (c) [35].

one (Figure 2.8c, d). As a linear reflector, tissues cancel out the two equal, opposed pulses, generating the minimal signal (Figure 2.8c). On the other hand, MBs behave as a non-linear reflector and the combined signals from the two pulses cannot be eliminated (Figure 2.8d), collectively producing a high contrast image [35, 42]. The pulse-inversion technique is particularly beneficial in imaging blood vessels even when the flow is slow, or the vessels are small [42]. The extensive utilization of MBs in clinical imaging, therefore, improve the accuracy and confidence of disease diagnosis to a great extent.

2.2.2 Water treatment

In the field of water treatment, MBs have also been used as a promising water-purifying agent

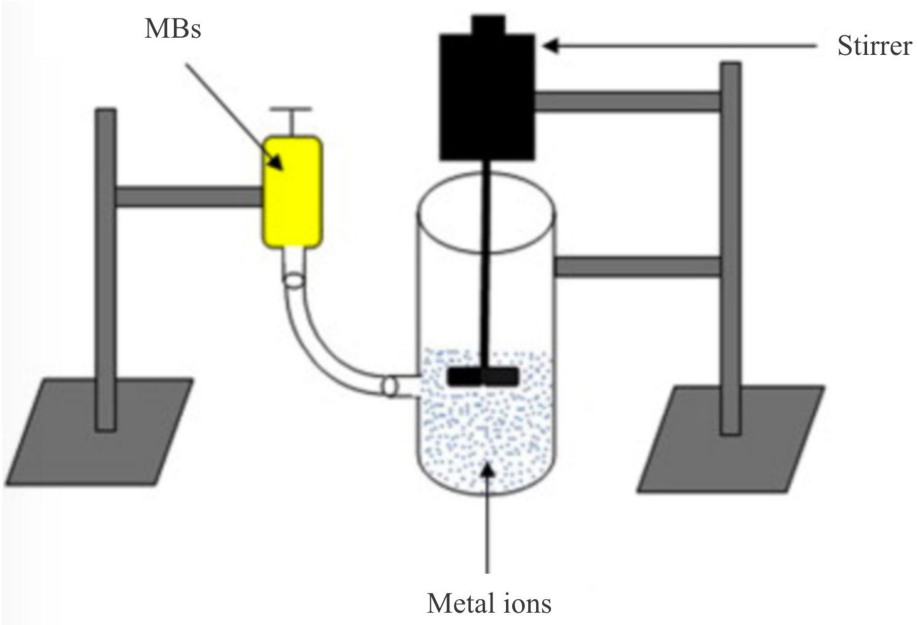

Figure 2.9 Schematic representation of using MBs to collect metal ions in a column flotation test [19].

for their capability of collecting waste ions and decomposing organic compounds [19, 28, 43]. Conventional water treatment methods have disadvantages such as high energy requirement, high capital cost, and low sensitivity to trace metal waste. The introduction of biocompatible materials such as the stabilizer-shelled MBs becomes favorable for their sensitive response and convenience for collection. For a conventional setup, a stirrer is frequently needed to mix the injected MBs with the metal ions because MBs tend to float to the top of the solution (Figure 2.9). Although the metal-collecting mechanism differs from ions to ions, a general mechanism has been reported to be two-step interactions [19]. Initially, metal ions diffuse into the surrounding regions of MBs through electrostatic interactions where the ions are physically bound to the surface of MBs. When the ions and the surface functional groups are brought in proximity, chemical bonds are subsequently formed and anchored onto the MBs [19].

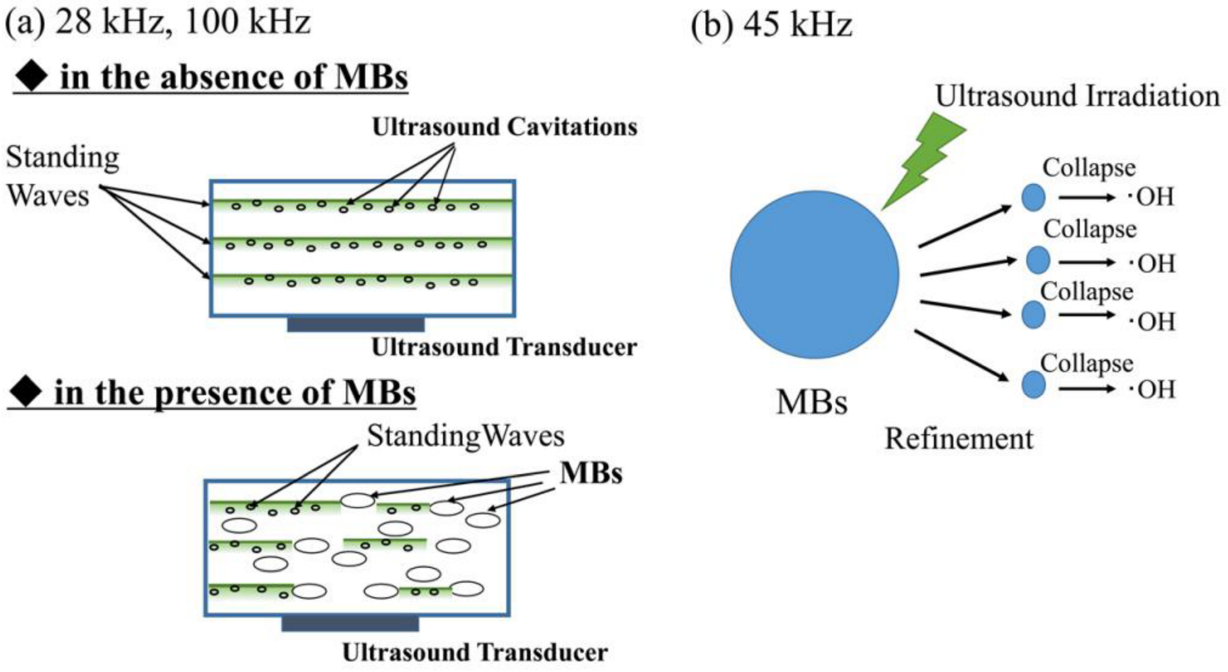

Figure 2.10 Dependence of ultrasound frequency on the suppression at 28 kHz and 100 kHz (a) and the enhancement at 45 kHz (b) with the presence of MBs [44].

In addition to the capabilities of collecting metal on their surface, MBs can also produce a tremendous number of free radicals that can efficiently decompose the organic waste in water treatment [28, 43]. It has been reported that the generation of free radicals in aqueous solution is dually dependent on the magnitude of frequency and the presence of MBs [44]. Stable cavitation is reached in a standing wave field in the absence of MBs at overly low or high ultrasound intensities; however, upon introducing MBs, the standing wave field is interrupted, thereby hindering the radical formation of OH (Figure 2.10a). In comparison, at a moderate level of ultrasound intensity, MBs enhance the generation of the free radicals, possibly because of the re-formation of the new MBs followed by the initial burst of the original MBs (Figure 2.10b). As the extent of chemical decomposition is dependent on the number of available free radicals,

detailed studies on the sonochemical process with the presence of MBs are needed for a wider application of using MBs as a water-purifying agent.

2.3.3 Drug delivery

Inspired by the concept of theranostic approach, the utilization of using MBs as an ultrasound contrast enhancer has been combined with their capability of delivering drug molecules [8-11]. The payload drugs are designed to be released at the targeted area following the imaging step either simultaneously or subsequently [10, 11]. Using acoustic radiation force, the drug-loaded MBs can be moved and concentrated at the targeted region; furthermore, they can be locally permeated into the microvasculature and cell membranes [10]. The vascular permeability can be

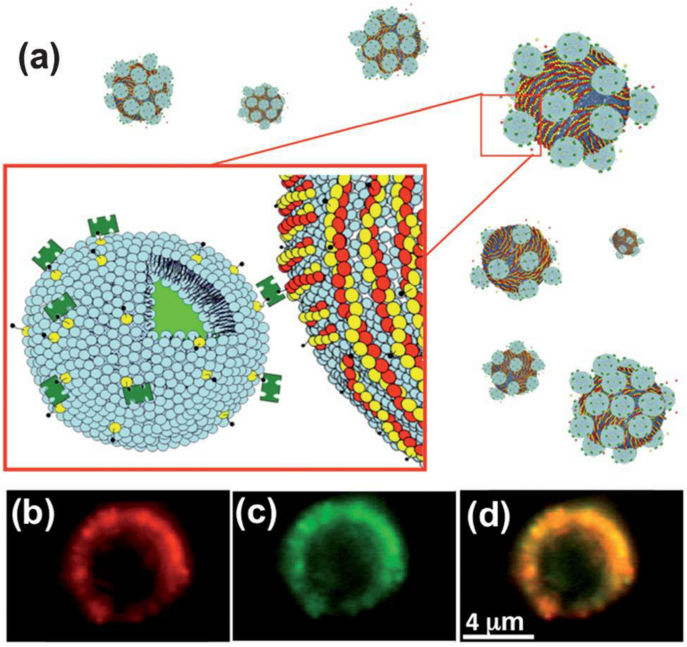

Figure 2.11 Through the biotin-neutravidin cross-linker (a), red (b), green (c), and orange (d) dye-loaded liposomes are bound to MBs [45].

subtly controlled by changing the acoustic parameters. As a result, the drug-loaded MBs are frequently adopted to disrupt blood-brain barrier that creates extravascular drug delivery challenges [9, 46]. The payload drugs can be either electrostatically deposited onto the surface of MBs or chemically bound to MBs through cross-linkers. The packing density of the loaded drugs can also be fine-tuned by controlling the number of cross-liners. For instance, different dyes-loaded liposomes were chemically bound to the surface of MBs through the biotin-neutravidin cross-linker (Figure 2.11).

In addition to the capability of carrying drugs, MBs can greatly alleviate the issues of hypoxia by using oxygen as the filling gas [47]. Hypoxia, referring to the local oxygen deficiency, is a key problem hindering the effectiveness of radiation and chemotherapy-based treatments because the

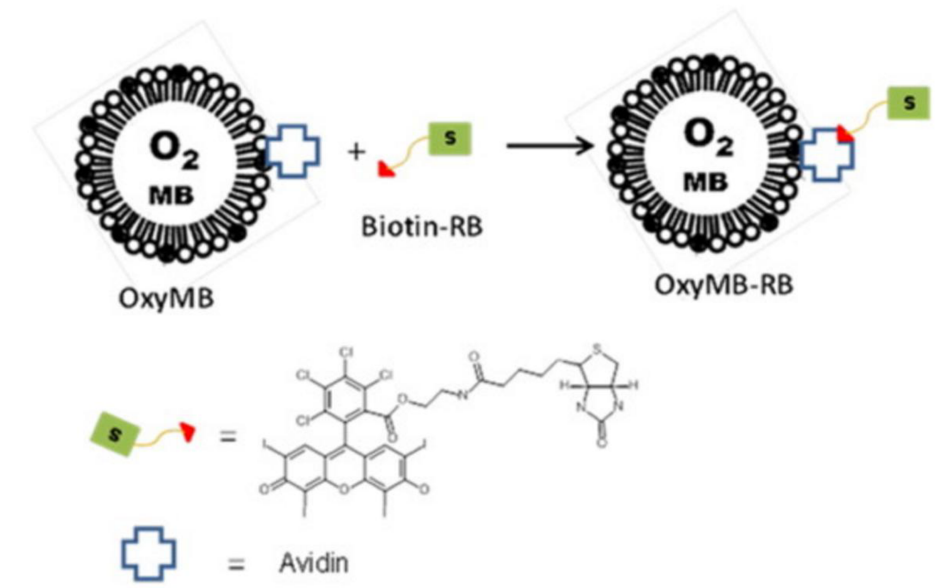

Figure 2.12 Schematic representation of a sensitizer-loaded, oxygen-rich MBs that can be excited by light of an appropriate wavelength [47].

cellular function is dramatically reduced around the oxygen-depleted tumor site [48]. The delivery of oxygen gas directly into the tumor site can be realized by using oxygen-enriched MBs [46]. It's reported that a sensitizing drug can be cross-linked onto MBs and also used as a switch controlling the rupture of MBs (Figure 2.12). In detail, upon emitting light of an appropriate wavelength, inertial cavitation of MBs can be induced, resulting in the destruction of MBs and the release of the entrapped oxygen gas (Figure 2.12). The simultaneous release of the drug and gas improve the concentration of oxygen at the tumor site as well as the efficiency of the treatment [46]. The unparalleled treatment using the drug-loaded MBs opens a new route for non-invasive cancer therapy.

2.4 References

[1] Maske, S.K., et al., INTERNATIONAL JOURNAL OF PHARMACY & LIFE SCIENCES. Int. J. of Pharm. & Life Sci.(IJPLS), 2012. 3(12): 2228-2235.

[2] Blomley, M. and D. Cosgrove, Microbubble echo-enhancers: a new direction for ultrasound? The Lancet, 1997. 349(9069): 1855-1856.

[3] Cosgrove, D., Echo enhancers and ultrasound imaging. European journal of radiology, 1997. 26(1): 64-76.

[4] Camarozano, A.C., et al., Effects of microbubbles and ultrasound on the microcirculation: observation on the hamster cheek pouch. Journal of the American Society of Echocardiography, 2010. 23(12): 1323-1330.

[5] Calliada, F., et al., Ultrasound contrast agents: basic principles. European journal of radiology, 1998. 27: S157-S160.

[6] Spencer, S.S., The relative contributions of MRI, SPECT, and PET imaging in epilepsy. Epilepsia, 1994. 35(s6): S72-S89.

[7] Janib, S.M., A.S. Moses, and J.A. MacKay, Imaging and drug delivery using theranostic nanoparticles. Advanced drug delivery reviews, 2010. 62(11): 1052-1063.

[8] Kiessling, F., et al., Ultrasound microbubbles for molecular diagnosis, therapy, and theranostics. Journal of nuclear medicine, 2012. 53(3): 345-348.

[9] Martin, K.H. and P.A. Dayton, Current status and prospects for microbubbles in ultrasound theranostics. Wiley Interdisciplinary Reviews: Nanomedicine and Nanobiotechnology, 2013. 5(4): 329-345.

[10] Lindner, J.R., Microbubbles in medical imaging: current applications and future directions. Nature Reviews Drug Discovery, 2004. 3(6): 527-533.

[11] Ferrara, K., R. Pollard, and M. Borden, Ultrasound microbubble contrast agents: fundamentals and application to gene and drug delivery. Biomedical Engineering, 2007. 9.

[12] Sirsi, S. and M. Borden, Microbubble compositions, properties and biomedical applications. Bubble Science, Engineering & Technology, 2009. 1(1-2): 3-17.

[13] Sirsi, S.R. and M.A. Borden, Advances in ultrasound mediated gene therapy using microbubble contrast agents. Theranostics, 2012. 2(12): 1208-1222.

[14] Sirsi, S., et al., Lung surfactant microbubbles. Soft Matter, 2009. 5(23): 4835-4842.

[15] Cavalieri, F., et al., Ultrasonic synthesis of stable, functional lysozyme microbubbles. Langmuir, 2008. 24(18): 10078-10083.

[16] Peyman, S.A., et al., Expanding 3D geometry for enhanced on-chip microbubble production and single step formation of liposome modified microbubbles. Lab on a Chip, 2012. 12(21): 4544-4552.

[17] Lajoinie, G., et al., In vitro methods to study bubble-cell interactions: Fundamentals and therapeutic applications. Biomicrofluidics, 2016. 10(1): 011501.

[18] De Cock, I., et al., Sonoprinting and the importance of microbubble loading for the ultrasound mediated cellular delivery of nanoparticles. Biomaterials, 2016. 83: 294-307.

[19] Nazari, A.M., P.W. Cox, and K.E. Waters, Copper ion removal from dilute solutions using ultrasonically synthesised BSA-and EWP-coated air bubbles. Separation and Purification Technology, 2014. 132: 218-225.

[20] Farook, U., et al., Preparation of microbubble suspensions by co-axial electrohydrodynamic atomization. Medical engineering & physics, 2007. 29(7): 749-754.

[21] Ekemen, Z., et al., Electrohydrodynamic bubbling: an alternative route to fabricate porous structures of silk fibroin based materials. Biomacromolecules, 2013. 14(5): 1412-1422.

[22] Mahalingam, S., M. Meinders, and M. Edirisinghe, Formation, stability, and mechanical properties of bovine serum albumin stabilized air bubbles produced using coaxial electrohydrodynamic atomization. Langmuir, 2014. 30(23): 6694-6703.

[23] Talu, E., Lipid-stabilized monodisperse microbubbles produced by flow focusing for use as ultrasound contrast agents and targeted drug delivery. 2007: ProQuest.

[24] Thomson, L.M., et al., Manufacture of concentrated, lipid-based oxygen microbubble emulsions by high shear homogenization and serial concentration. Journal of visualized experiments: JoVE, 2014(87).

[25] Gazzera, L., et al., Design of Highly Stable Echogenic Microbubbles through Controlled Assembly of Their Hydrophobin Shell. Angewandte Chemie, 2016. 128(35): 10419-10423.

[26] Mahalingam, S., et al., Formation of protein and protein–gold nanoparticle stabilized microbubbles by pressurized gyration. Langmuir, 2014. 31(2): 659-666.

[27] Suslick, K.S., Ultrasound: its chemical, physical, and biological effects. 1988: VCH Publishers.

[28] Suslick, K.S., Sonochemistry. science, 1990. 247(4949): 1439-1445.

[29] Grinstaff, M.W. and K.S. Suslick, Air-filled proteinaceous microbubbles: synthesis of an echo-contrast agent. Proceedings of the National Academy of Sciences, 1991. 88(17): 7708-7710.

[30] Touch, V., S. Hayakawa, and K. Saitoh, Relationships between conformational changes and antimicrobial activity of lysozyme upon reduction of its disulfide bonds. Food chemistry, 2004. 84(3): 421-428.

[31] Cavalieri, F., et al., Antimicrobial and biosensing ultrasound-responsive lysozyme-shelled microbubbles. ACS applied materials & interfaces, 2013. 5(2): 464-471.

[32] Vong, F., et al., A comparison of the physical properties of ultrasonically synthesized lysozyme-and BSA-shelled microbubbles. Ultrasonics sonochemistry, 2014. 21(1): 23-28.

[33] Zhou, M., F. Cavalieri, and M. Ashokkumar, Tailoring the properties of ultrasonically synthesised microbubbles. Soft Matter, 2011. 7(2): 623-630.

[34] Cavalieri, F., et al., One-pot ultrasonic synthesis of multifunctional microbubbles and microcapsules using synthetic thiolated macromolecules. Chemical Communications, 2011. 47(14): 4096-4098.

[35] Schutt, E.G., et al., Injectable microbubbles as contrast agents for diagnostic ultrasound imaging: the key role of perfluorochemicals. Angewandte Chemie International Edition, 2003. 42(28): 3218-3235.

[36] Kabalnov, A., et al., Dissolution of multicomponent microbubbles in the bloodstream: 1. Theory. Ultrasound in medicine & biology, 1998. 24(5): 739-749.

[37] Qin, S., C.F. Caskey, and K.W. Ferrara, Ultrasound contrast microbubbles in imaging and therapy: physical principles and engineering. Physics in medicine and biology, 2009. 54(6): R27.

[38] de Jong, N., et al., Absorption and scatter of encapsulated gas filled microspheres: theoretical considerations and some measurements. Ultrasonics, 1992. 30(2): 95-103.

[39] Chomas, J.E., et al., Mechanisms of contrast agent destruction. IEEE transactions on ultrasonics, ferroelectrics, and frequency control, 2001. 48(1): 232-248.

[40] Villarraga, H.R., et al., Destruction of contrast microbubbles during ultrasound imaging at conventional power output. Journal of the American Society of Echocardiography, 1997. 10(8): 783-791.

[41] Krishna, P.D. and V.L. Newhouse, Second harmonic characteristics of the ultrasound contrast agents Albunex and FSO69. Ultrasound in medicine & biology, 1997. 23(3): 453-459.

[42] Mulvagh, S.L., et al., Contrast echocardiography: current and future applications. Journal of the American Society of Echocardiography, 2000. 13(4): 331-342.

[43] Xu, Q., et al., A comparative study of microbubble generation by mechanical agitation and sonication. Innovative Food Science & Emerging Technologies, 2008. 9(4): 489-494.

[44] Masuda, N., et al., Influence of microbubbles on free radical generation by ultrasound in aqueous solution: dependence of ultrasound frequency. The Journal of Physical Chemistry B, 2015. 119(40): 12887-12893.

[45] Heath, G.R., et al., Self-assembly of actin scaffolds on lipid microbubbles. Soft matter, 2014. 10(5): 694-700.

[46] Ting, C.-Y., et al., Concurrent blood–brain barrier opening and local drug delivery using drug-carrying microbubbles and focused ultrasound for brain glioma treatment. Biomaterials, 2012. 33(2): 704-712.

[47] McEwan, C., et al., Oxygen carrying microbubbles for enhanced sonodynamic therapy of hypoxic tumours. Journal of Controlled Release, 2015. 203: 51-56.

[48] Vaupel, P., F. Kallinowski, and P. Okunieff, Blood flow, oxygen and nutrient supply, and metabolic microenvironment of human tumors: a review. Cancer research, 1989. 49(23): 6449-6465.

Chapter 3 Experimental Techniques

3.1 In-vitro release testing (IVRT)

In-vitro release testing heavily relies on the utilization of dialysis tubes [1, 2], which was adopted in the experiments carried out in this study. The porous membrane gives rise to the nature of selective permeability that based on the size of molecules. In other words, the semi-permeable membrane allows small molecules to pass through the pores while trapping the large molecules inside the membrane [3]. At the beginning of dialysis, the molecules smaller than the pore size of the membrane are driven to move to the releasing medium because of the concentration gradient (Figure 3.1a). After a period of time, the equilibrium is reached when the concentration of the small molecules inside and outside the dialysis bag is balanced (Figure 3.1b).

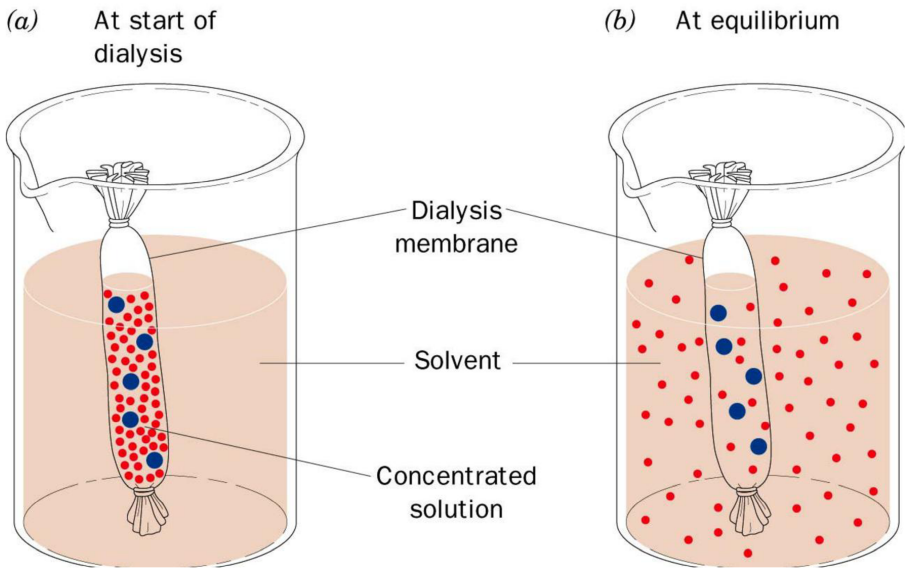

Figure 3.1 Schematic representation of the set-up for the in-vitro release test at the start (a) and the equilibrium (b) of dialysis [4].

In a typical in-vitro drug release test, the drug-loaded carrier is immersed into a dialysis bag of an appropriated molecular weight cut-off normally at 37 °C to mimic a cellular environment [1, 2]. At a pre-determined interval, a small aliquot of solution from the releasing medium is withdrawn and replaced with an equal volume of fresh medium. The withdrawn solution can be then analyzed for the released drug molecules that diffuse through the pores of the dialysis bag. The cumulative releasing profile of the loaded drug is then calculated by dividing the cumulated released amount by the overall loaded amount [1, 2]. The releasing medium might be different from the trapped medium inside the dialysis bag to simulate a particular extracellular environment. Different buffers or different pH conditions might also be adopted to fit the needs of the releasing condition better. Although the in-vivo releasing profiles are likely to be much different from the in-vitro behavior, the information collected from the in-vitro release testing gives reliable preliminary data and directs further in-vivo and clinical studies.

3.2 Quartz crystal microbalance with dissipation monitoring (QCM-D)

Quartz crystal microbalance with dissipation monitoring (QCM-D) measures the mass and dissipation variations by measuring the changing in the frequency of a quartz piezoelectric crystal sensor [5-8]. The variations in the electromechanical response can be sensitive enough to detect molecule binding or structural transformation of the attached layers of molecules on the piezoelectric crystal sensor [8]. The mathematical relationship between the change of the resonance frequency and the mass of the adsorbed material is described below,

$$-\Delta f = \frac{n f_o \Delta m}{\rho_q t_q} = \frac{n \Delta m}{c}$$

where n, fo, Δm, ρq, tq, and c represent the overtone number, the fundamental resonance frequency, the change of the added mass, the density of quartz crystal, the thickness of the crystal, and the sensitivity constant [9]. A specified voltage is applied to cause the crystal to oscillate, and the change of the adsorbed mass can be calculated based on the change of the oscillation frequency [9]. However, this relationship can be only applied to the mass rigidly adsorbed with no slip or deformation imposed by the oscillation crystal surface [9]. When the change of dissipation above 5% of the change of frequency, the relationship can be fitted using the viscoelastic model (not shown) instead [10]. With great sensitivity, the use of QCM-D measurements in our experiment demonstrates the surface interactions between our synthesized MBs with metal surfaces with different charges and simulates the loading of each layer in the drug loading test.

3.3 Scanning electron microscope (SEM)

Scanning electron microscope (SEM) imaging was extensively used in our studies to track the morphological change of MBs for its capabilities to provide information on surface topography, crystalline structure, chemical composition, and electrical behavior [11-13]. Compared to the 1,000x magnification of the conventional optical microscope, SEM can achieve resolution of 1 nm, which is equivalent to 1,000,000x. In addition to the higher resolution, other types of information such as chemical analysis and electrical properties can be obtained using SEM. In comparison with transmittance electron microscope (TEM), SEM is also advantageous for the following reasons [11, 12]. SEM enables non-destructive evaluation of the specimen while TEM easily damages the specimen during the specimen preparation [11, 13]. A much larger specimen

can be examined using SEM than TEM. A 200 mm diameter wafer is normally used for SEM while a 3 mm diameter wafer can be used for TEM. In addition, sample preparation is also very different between SEM and TEM; in other words, TEM specimen preparation is much more complex and time-consuming than SEM [11].

In SEM, two or three electromagnetic lenses concentrate the electron beam into a fine probe which is used to scan across the area of interest [13]. The electrons penetrate through and interact with the sample at various depths, producing signals like secondary electrons, backscatterd electrons, and characteristic X-rays [11, 13]. A high-resolution micrograph can be obtained at high accelerating voltages with the risk of heavy sample damage. So, for a fragile sample, a lower accelerating voltage can be used for imaging albeit having a lower resolution.

3.4 Spectrophotometric measurements

Ultraviolet-visible (UV/Vis) and fluorescent confocal laser scanning microscopy (CLSM) spectrophotometric measurements were adopted at different stages in our studies for their capabilities to quantify the concentration based on either the UV/Vis absorption or fluorescent emission. As indicated by the name, UV/Vis spectroscopy refers to the adsorption of analytes in the visible and near-UV regions [14, 15]. A beam of light from a visible or UV light source is separated into its components through a prism and split in a two equal density beam by a half mirror [15]. One beam passes through the sample-containing cuvette, and the other one goes through the solvent-only cuvette. The intensities of the sample and reference beam are denoted as I_0 and I, respectively, and the relationship between the intensities and concentration can be depicted by the Beer-Lambert law, $A = log_{10}(I_0/I) = \varepsilon cL$, where A, ε, and c are measured

absorbance, extinction coefficient, and the concentration of the absorbing material, respectively [16]. However, adsorption flattening is likely to occur when the solution of interest is either too high in concentration or not homogeneous; in such conditions, the measurement would deviate from the Beer-Lambert law.

Fluorescent CLSM, often used as a complementary to UV/Vis spectrophotometric measurement, deals with the electron transition from the excited state to the ground state [17]. By eliminating the out-of-focus background signal, fluorescent CLSM provides significant enhancement of both axial and lateral imaging resolution. A three-dimensional image is easily obtained with fluorescent CLSM by collecting a stack of optical sections, enabling an in-depth analysis of the sample of interest [17]. However, two major problems limit the utilization of fluorescent CLSM listed as following. Fluorescence photo-bleaching limits the available fluorescent photons. Also, the excited state of the fluorophore easily saturates the fluorescence emission and hinders the collection of images.

3.5 Dynamic light scattering

Dynamic light scattering (DLS) has been widely used in many fields such as physics, biology, and medicine [18]. With a monochromatic laser source, DLS provides a facile and accurate method for measuring the particle sizes. In brief, the collected mutual translational diffusion coefficient of macromolecules is inversely related to the particle size, and small particles diffuse much quicker than the large ones [19]. In a typical analysis, the autocorrelation function decays with time, and particles of a smaller size give rise to a faster decorrelation of scattered intensity

[19]. As a result, the fitting of the autocorrelation function becomes critically important because the extent of fitting reflects the accuracy of the measurement.

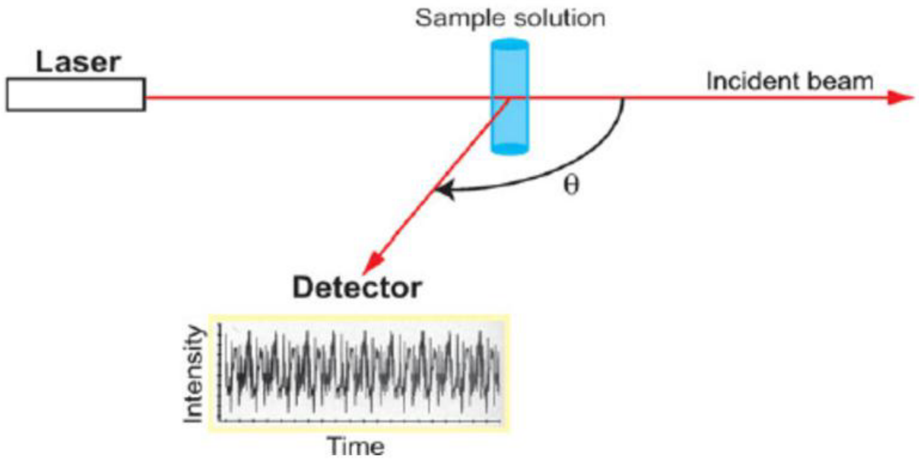

Figure 3.2 Schematic representation of the dynamic light scattering measurement [19].

We used the DLS to measure the hydrodynamic size of the synthesized polymer at various temperatures. By a conventional definition, the hydrodynamic size is defined to be a hypothetical sphere that diffuses with the same speed as the particles of interest. The size measured by the DLS is the hydrodynamic size which was automatically calculated using the Stokes-Einstein equation (not shown).

3.5 References

[1] Nigam, S., K. Barick, and D. Bahadur, Development of citrate-stabilized Fe_3O_4 nanoparticles: conjugation and release of doxorubicin for therapeutic applications. Journal of Magnetism and Magnetic Materials, 2011. 323(2): 237-243.

[2] Qiu, F., et al., Real-time monitoring of anticancer drug release with highly fluorescent star-conjugated copolymer as a drug carrier. Biomacromolecules, 2014. 15(4): 1355-1364.

[3] Koros, W., Y. Ma, and T. Shimidzu, Terminology for membranes and membrane processes. J. Membr. Sci, 1996. 120(2): 149-159.

[4] Instituion, S.R.E. Selective Permeability of Dialysis Tubing Lab Explained. [cited 2016 Dec. 31].

[5] Rodahl, M., et al., Quartz crystal microbalance setup for frequency and Q-factor measurements in gaseous and liquid environments. Review of Scientific Instruments, 1995. 66(7): 3924-3930.

[6] Rodahl, M., F. Höök, and B. Kasemo, QCM operation in liquids: an explanation of measured variations in frequency and Q factor with liquid conductivity. Analytical Chemistry, 1996. 68(13): 2219-2227.

[7] Janshoff, A., H.J. Galla, and C. Steinem, Piezoelectric Mass-Sensing Devices as Biosensors—An Alternative to Optical Biosensors? Angewandte Chemie International Edition, 2000. 39(22): 4004-4032.

[8] Reimhult, E., et al., Simultaneous surface plasmon resonance and quartz crystal microbalance with dissipation monitoring measurements of biomolecular adsorption events involving structural transformations and variations in coupled water. Analytical chemistry, 2004. 76(24): 7211-7220.

[9] Sauerbrey, G., Verwendung von Schwingquarzen zur Wägung dünner Schichten und zur Mikrowägung. Zeitschrift für physik, 1959. 155(2): 206-222.

[10] Voinova, M.V., et al., Viscoelastic acoustic response of layered polymer films at fluid-solid interfaces: continuum mechanics approach. Physica Scripta, 1999. 59(5): 391.

[11] Vernon-Parry, K., Scanning electron microscopy: an introduction. III-Vs Review, 2000. 13(4): 40-44.

[12] Goldstein, J., et al., Scanning electron microscopy and X-ray microanalysis: a text for biologists, materials scientists, and geologists. 2012: Springer Science & Business Media.

[13] Hayat, M.A., Principles and techniques of scanning electron microscopy. Biological applications. Volume 1. 1974: Van Nostrand Reinhold Company.

[14] Ingle Jr, J.D. and S.R. Crouch, Spectrochemical analysis. 1988.

[15] Perkampus, H.-H., H.-C. Grinter, and T. Threlfall, UV-VIS Spectroscopy and its Applications. 1992: Springer.

[16] Swinehart, D., The beer-lambert law. J. Chem. Educ, 1962. 39(7): 333.

[17] Sandison, D.R., et al., Quantitative fluorescence confocal laser scanning microscopy (CLSM), in Handbook of biological confocal microscopy. 1995, Springer. 39-53.

Chapter 4 A facile sonochemical synthesis of shell-stabilized reactive microbubbles using surface-thiolated bovine serum albumin with the Traut's reagent[1]

4.1 Introduction

In the last decade, microbubbles have been utilized in clinical applications [1-11], food industries [12, 13], and water treatment [14, 15]. In clinical practice, as ultrasound contrast agents, microbubbles can improve the quality of the medical imaging [1-3. 5-11]. Microbubbles have been employed as drug carriers [1-3, 5, 6] and the loading of therapeutic molecules onto or into the microbubbles can aid the coupling of imaging with therapeutics (theranostics) [7, 8, 11]. Microbubbles have also been used for surface attachments with other functional molecules such as magnetic, semiconductor nanoparticles, and stimulus-responsive polymers [4, 9, 10]. For example, Lentacker *et al.* developed polycation-coated microbubbles as potential gene delivery carriers [4]; *Park et al.* demonstrated ultrasound and magnetic resonance imaging applications of microbubbles loaded with metal, metal oxide or semiconductor nanoparticles [10]. Owing to their intrinsic antimicrobial properties, microbubbles have been intensively studied in the food industry as a sterilizing agent to depress the growth of *Bacillus* spores and *Escherichia coli* [12, 13]. In wastewater treatment, ultrasonic radiation of microbubbles produces a vast number of free radicals which can efficiently decompose organic compounds [14, 15].

[1] A version of this chapter was published on *Ultrasonics Sonochemistry* as Ma, X., Bussonniere, A., & Liu, Q. (2017). A facile sonochemical synthesis of shell-stabilized reactive microbubbles using surface-thiolated bovine serum albumin with the Traut's reagent. *Ultrasonics Sonochemistry*, *36*, 454-465

Without stabilizers, a short lifetime (~ several hours) limits the use of conventional gas-filled microbubbles [16, 17]. The pressure difference originating from the curved surface of the bubble, known as the Laplace pressure, spontaneously drives the entrapped gas to diffuse into the liquid phase [17, 18]. Besides, Ostwald ripening adversely affects the lifetime of microbubbles; specifically, coalescence continues to reduce the surface energy of microbubbles until a complete phase separation is reached [19-21]. Surfactants can reduce the surface energy to lengthen the lifetime of microbubbles [22, 23]; alternatively, biocompatible polymers such as proteins and lipids can be employed to construct a rigid shell, which reduces outward gas diffusion [3, 24, 25]. Cavalieri *et al.* and Talu *et al.* respectively synthesized lysozyme-shelled and lipid-coated microbubbles with a lifetime of several months [24, 25].

The formation of disulfide bond has shown to increase the stability of microbubbles [25-28]. During the process of acoustic cavitation, superoxide is generated, cross-linking free thiols of cysteine residues [25]. A higher disulfide content contributes to a thicker shell and thus to a greater stability of microbubbles [27]. Free thiols can be released internally from proteins with reducing agents such as DL-dithiothreitol (DTT) to enhance inter- and intramolecular disulfide bridging during microbubble formation [25, 26, 28]. However, such treatment might excessively loosen up the protein structure and gives rise to a lowered hydrophobicity, which reduces the stability of microbubbles [27].

In this paper, we reported, for the first time, a facile synthesis of long-lived microbubbles with surface-treated proteins. Traut's reagent, which reacts with primary amines (Figure 4.1a), was applied to our model protein BSA to render thiol groups externally [29]. Upon the ultrasonic

radiation, the thiolated BSA (BSA-SH) forms the shell of microbubbles with air entrapped inside (BSA-SH MBs). Within a week, BSA-SH MBs gradually shrank to a critical size of ~850 nm while forming a thicker shell. As a result of bubble shrinkage, the increased Laplace pressure was balanced by the thickened shell, reaching an equilibrium and stabilizing for several months. The characterizations of microbubbles by Fourier transform infrared (FTIR) spectroscopy and X-ray photoelectron spectroscopy (XPS) indicated the presence of primary amines and thiols after the microbubble synthesis. Quartz crystal microbalance with dissipation monitoring (QCM-D) illustrated their reactivities on silica, alumina, and gold surfaces, shedding light on the possibilities of utilizing BSA-SH MBs in other applications such as drug delivery and metal removal from wastewater.

4.2 Materials and Methods

Lyophilized BSA (≥ 96%), Traut's reagent (≥ 98%), ethylenediaminetetraacetic acid (EDTA) (≥ 98.5%, ED-100G), silica nanoparticles (10-20 nm) and alumina nanoparticles (< 50 nm) were purchased from Sigma-Aldrich. Phosphate buffered saline (PBS) and spin desalting columns were acquired from ThermoFisher Scientific. All reagents were used as received without further treatment. Milli-Q water with a resistivity of 18.2 MΩ•cm was used for preparing solutions. Stock solutions of hydrochloric acid (HCl, 0.1 M) and sodium hydroxide (NaOH, 0.1M) were used to adjust the pH of solutions.

4.2.1. Synthesis of microbubbles using surface-treated BSA

EDTA (5 mM) was added to PBS to prevent oxidation of free sulfhydryls [30], and the EDTA-PBS mixture was adjusted to pH 8 with 0.1 M NaOH to assist effective thiolation of BSA with Traut's reagent [29, 31]. BSA (50 mg in 0.75 ml EDTA-PBS) and Traut's reagent solutions (0, 0.5, 2, and 5 mg in 0.25 ml EDTA-PBS) were prepared, and BSA and Traut's reagent were allowed to react by mixing to form 1 ml solutions of 0, 5, 20, and 50 times molar excess of Traut's reagent. The mixtures were incubated for 1 hour at 23°C with a gentle swirling of 60 rpm (New Brunswick Innova 42/42R) before decanting into spin desalting columns to stop the reaction and remove the excess Traut's reagent. The mixtures were placed in a water bath (Fischer Scientific Isotemp Bath 4100 R20) at 45 °C for 10 minutes (Figure 4.1c) to moderately loose up the structure of the thiolated BSA (BSA-SH). A conformational change of BSA does not occur below 40 °C, and undesired aggregations start to take place at approximately 50°C [32-34]. Ultrasonic radiation of 20 kHz was applied to the mixtures with a sonic dismembrator (Fisher Scientific^{TM} Model 705). A temperature probe was used to monitor the solution temperature throughout the ultrasonic radiation (Figure 4.1b). An ultrasound impulse of 23% amplitude, equivalent to 173 W, was applied for 45 sec. The combination of amplitude and duration was selected based on empirical evidence. After the microbubble synthesis, two separate phases were formed. In brief, the foam phase containing the large, visible bubbles was at the top, and the aqueous phase containing the desired microbubbles was at the bottom. The synthesized microbubbles were separated from the large, visible bubbles using a pipette. The separated aqueous phase was then centrifuged at 300 relative centrifugal force (RCF) for 10 min

to collect the microbubbles [35], and then the top layer of the supernatant was resuspended in PBS. Milli-Q water was used to resuspend the supernatant for the QCM-D measurements. The

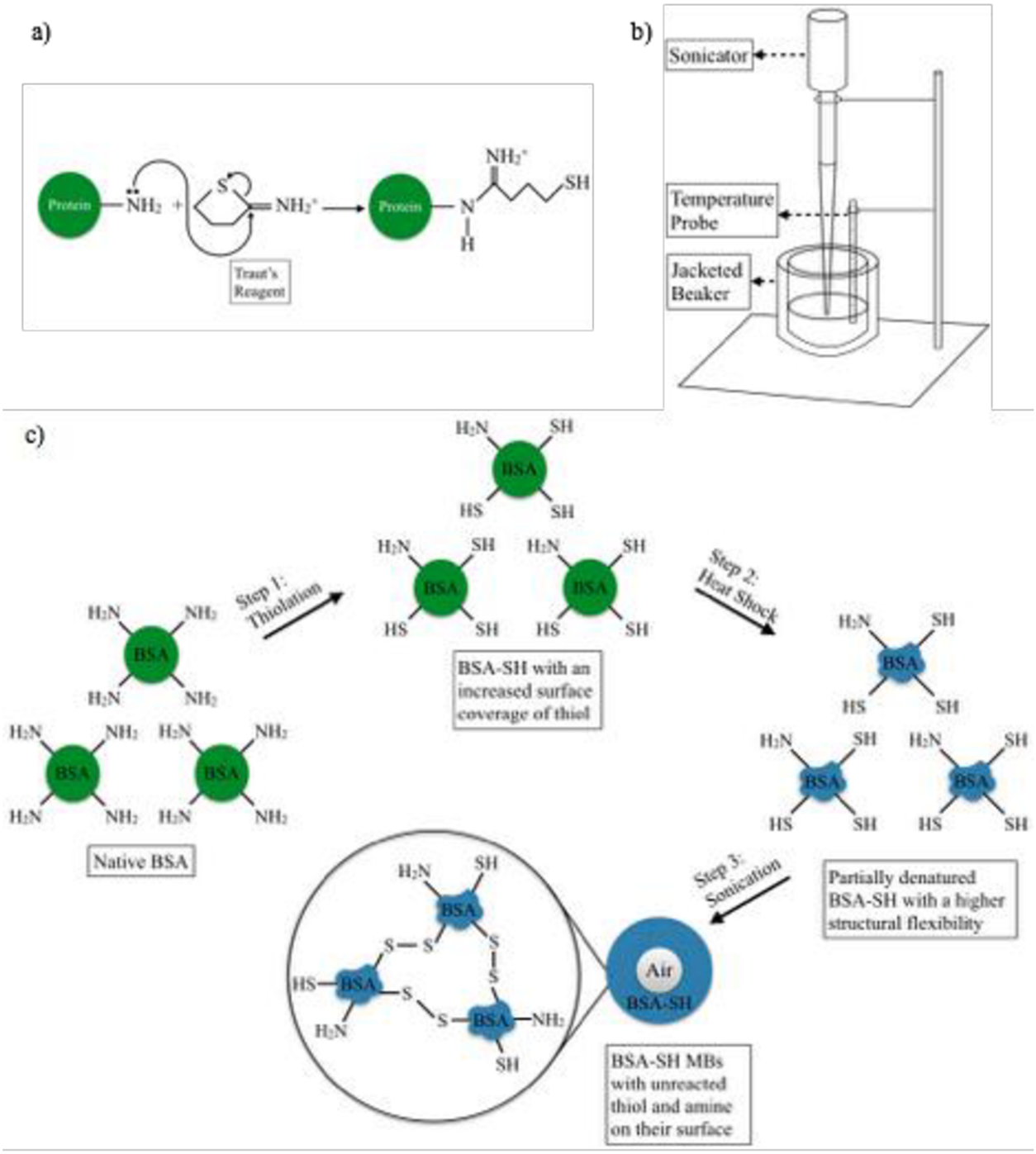

Figure 4.1 Schematics for the mechanism of thiolation of a protein with the Traut's reagent (a), experimental setup of sonication (b), and flow charts of synthesis of BSA-SH MBs (c).

centrifugal collection was repeated for three times, and the collected microbubbles were later stored at 4 °C.

4.2.2 Scanning electron microscope (SEM) imaging

To study morphology and the shell thickness of BSA-SH MBs, SEM images were collected using a field emission scanning electron microscope (FESEM: Carl-Zeiss Sigma) operated at an acceleration voltage of 5 kV. A small aliquot of the as-synthesized solution of BSA-SH MBs was dropped on a silicon wafer and left to evaporate overnight. To measure the shell thickness of the synthesized MBs under different conditions, a cross section of the shell was needed, and it was obtained by gently scraping the air-dried BSA-SH MBs with a piece of fine sandpaper [36]. Following the breakage of microbubbles and the exposure of their cross sections, SEM images of them were obtained and the thickness of their shells was measured using ImageJ [37]. In brief, a number of lines were drawn using ImageJ to label the thickness of the shell, from the outside to the inside boundary of the shell. The length of these lines was automatically calculated by ImageJ and averaged out to the thickness of the shell. For a better conductivity, a carbon thin film was sputter-coated on the sample surface before the imaging collection.

4.2.3 Size distribution, zeta potential, surface tension measurements

ImageJ software [37] and a ZetaPALS particle size analyzer (Brookhaven Instrument, USA) were both adopted for size distribution measurements. Images of microbubbles at different stages

were collected with a digital microscope (KEYENCE, VHX-700F) and histograms were accordingly generated via ImageJ. The size distributions were additionally measured using a ZetaPALS dynamic light scattering detector (Brookhaven Instruments, USA); 300 measured values were used to generate a size distribution histogram. The zeta potentials of silica nanoparticles, alumina nanoparticles, and BSA-SH MBs at different pH values were also measured by the ZetaPALS module. Before measurements, the suspensions containing these agents were respectively diluted using PBS and adjusted to various pH values with HCl and NaOH. The zeta potential at each pH value was averaged over ten measurements. The surface tension of the surface-treated BSA aqueous solution was measured using a Theta Optical Tensiometer T200 (Biolin Scientific, Stockholm, Swden). A quartz cell was used to contain the BSA-SH solution, and an air bubble was generated from a gastight syringe with a needle. The air bubble was recorded and analyzed using the Theta software for the measurement of the surface tension.

4.2.4 FTIR and XPS measurements

BSA was used as purchased. Lyophilized BSA-SH, BSA-SH MBs, and BSA-SH MBs reacted with alumina nanoparticles were collected using a freeze dryer (Labconco FreeZone 4.5) and subjected to FTIR spectroscopy and XPS. FTIR spectra were recorded with 32 scans at a resolution of 1 cm^{-1} using a Nicolet iS50 FT-IR spectrometer equipped with an iS50 automated beamsplitter exchanger (ABX) at wavenumber 700 to 4000 cm^{-1}. For a non-destructive analysis, the attenuated total reflectance (ATR) module was adopted instead of the diffuse reflectance infrared Fourier transmission spectroscopy (DRIFTS) or potassium bromide (KBr) method

which involves sample grinding and destruction. High-resolution X-ray photoelectron spectra of N1s and S2p were obtained using an XPS (Kratos AXIS 165) with monochromatic Al Kα X-rays (1486.6 eV). The X-ray source was applied at 210 W, and the pressure was kept at 2.5E-8 torr. A pass energy of 20 eV at an increment of 0.1 eV was used to collect the high-resolution XPS output. The Gaussian Lorentzian functions were used for fitting because of the instrumental broadening of the peaks and the minimized residues after the fitting.

4.2.5 QCM-D measurements

QCM-D measurements were performed using a D300 QCM-D (Q-Sense Västra Frölunda, Sweden) with a QAFC 302 axial flow measurement chamber. The silica, alumina, and gold sensors (QSX303), supplied by Q-Sense AB, were quartz crystals coated with SiO2, Al2O3, and Au, respectively. Before the injection of solutions, all sensors were placed in the chamber and excited to their fundamental resonant frequency at ~ 4.9 MHz using an AC voltage. The chamber was thermally controlled at 23 °C, and the flow rate was adjusted to 25 μL/min using a flow dispenser (ISM935C, ISMATEC). Background solutions consisting of Milli-Q water pre-adjusted to the same pH as the solution of BSA-SH MBs were injected into the chamber for 10 min. Following the background solution, the solution of BSA-SH MBs flowed into the chamber for 30 min, and then the chamber was rinsed with the original background solution for 10 min.

4.3 Results and Discussions

4.3.1 Spatial and temporal size distributions of BSA-SH MBs

As the size of microbubbles plays a critical role in governing their applications, the spatial and temporal size distributions were respectively studied. Because the Traut's reagent dosage is directly linked to the conversion efficiency of primary amines to thiols, its effect on the size distribution of the microbubbles formed was determined. In the absence of the Traut's reagent, microbubbles were observed to be present in a size range of 0.4 - 4.0 µm (Figure 2a) by image analysis and in a size range of 0.4 - 1.8 µm (Figure S1a) by dynamic light scattering. Upon

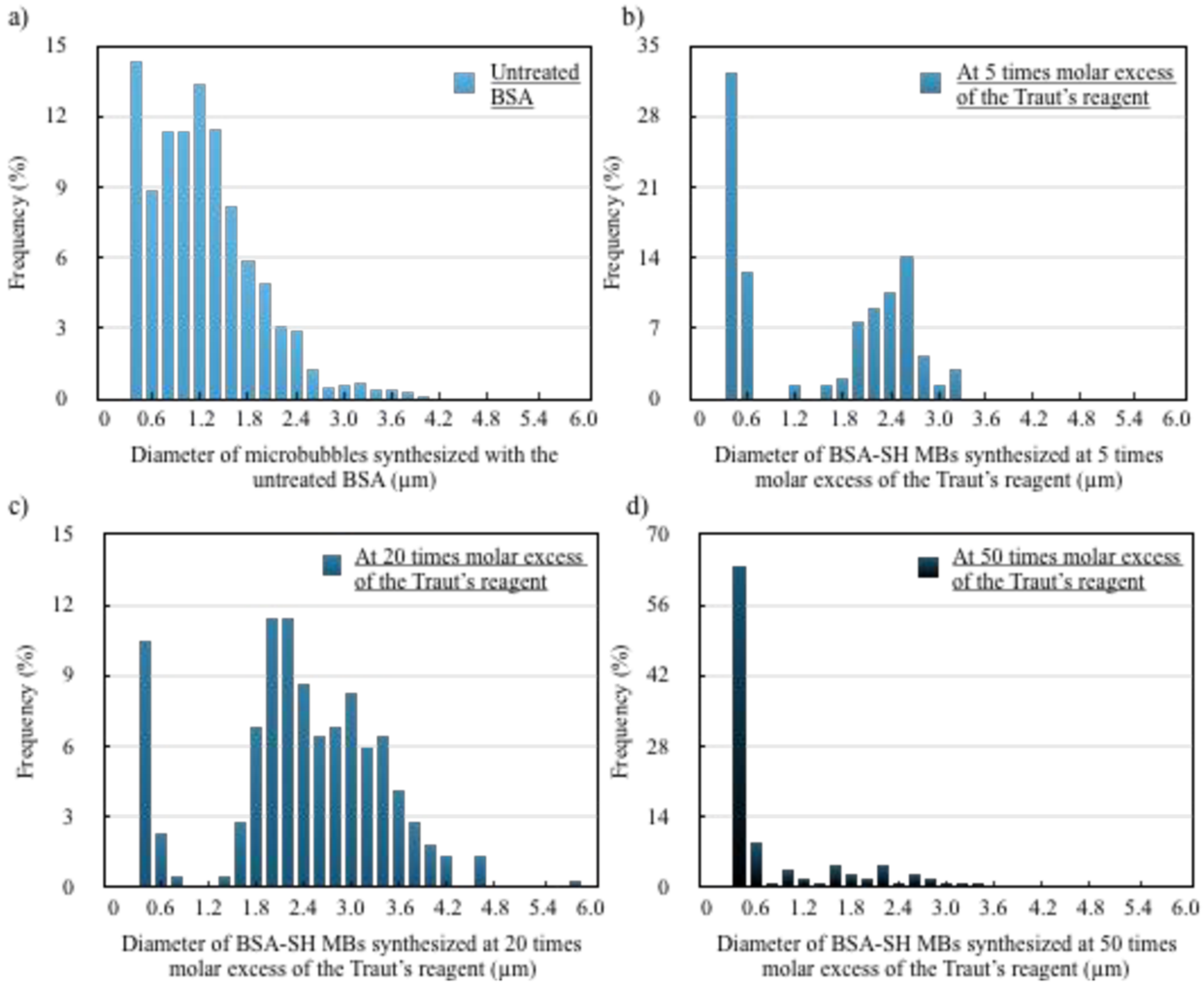

Figure 4.2 Spatial size distributions of microbubbles synthesized with BSA (a), BSA treated with 5 (b), 20 (c), and 50 (d) times molar excess of Traut's reagent were obtained by image processing immediately after the centrifugal collection.

introducing the Traut's reagent, a bimodal distribution of microbubbles separately centered at 0.5 and 2.5 μm, respectively, were observed (Figure 2b, c, S1b, c). On the contrary, such a trend was not present when the molar excess of Traut's reagent was increased to 50 times (Figure 2d, S1d). To determine an optimal ratio of the Traut's reagent to BSA, the stability of microbubbles was tested. In detail, microbubbles originally sized at ~ 0.5 μm were merely capable of maintaining the bubble structure for a few hours, consistent with the reported short lifetime of conventional BSA microbubbles [26, 38, 39]. On the other hand, microbubbles initially with an average size of 2.5 μm were longer-lived, and the bubbles gradually shrank to ~850 nm in the days following the synthesis. At 20 times BSA molar excess of the Traut's reagent, such a long-lived fraction of the synthesized microbubbles was observed to be the greatest (Figure 2c, S1c), and this condition was therefore considered to be optimal for the synthesis of BSA-SH MBs and the subsequent characterizations (Figure 3, 7, 8, 9, 10, 11). The higher dosage of the Traut's reagent, the more surface coverage of thiols after the reaction, which results in more disulfide bonds for strengthening the shell. In other words, the formation of the long-lived microbubbles was a result of the optimal surface coverage of thiols. It was therefore hypothesized that a molar excess of the Traut's reagent of 5 times BSA or lower did not provide sufficient surface coverage of thiol groups available for synthesizing stable microbubbles. On the other hand, an overly high surface coverage of thiol groups rendered by high dosages such as 50 times molar excess of Traut's reagent to BSA created excessive steric hindrance to stable microbubble formation. This argument was experimentally supported through the measurement of the shell thickness of the microbubbles synthesized with surface-treated BSA with different molar excesses of the Traut's reagent (Figure 6a, S4a-d). In detail, the untreated BSA generated a shell of 45±10 nm upon ultrasonic radiation while the treated BSA formed microbubbles with a thicker shell. The 20

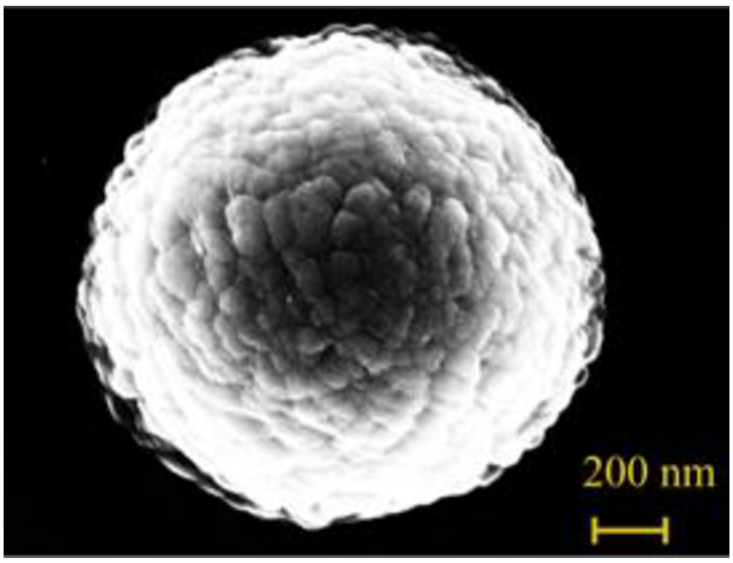

Figure 4.3. At a 20 times BSA molar excess of Traut's reagent, an SEM image of the BSA-SH MBs were taken immediately following the centrifugal collection.

times molar excess of the Traut's reagent gave rise to the greatest thickness of the subsequently generated microbubbles, 155 ± 20 nm, further explaining their long-term stability. However, an excessively low or high molar excess of the Traut's reagent such as 5 or 50 times failed to enhance the lifetime of the synthesized microbubbles as much as the optimal 20 times molar excess, shown as moderately thickened shell thicknesses of 75 ± 20 nm and 85 ± 10 nm, respectively.

At the aforementioned optimal condition, temporal size distributions of BSA-SH MBs were accordingly measured using image analysis and dynamic light scattering. A roughly bimodal size distribution with two peaks at 2.5 and 0.5 μm appeared following the synthesis (Figure 2c, 4a). As mentioned above, the unstable portion sized at 0.5 μm, pointed by the red arrows (Figure 4a), were mostly vanished within a few hours and completely disappeared in 1 day after the synthesis

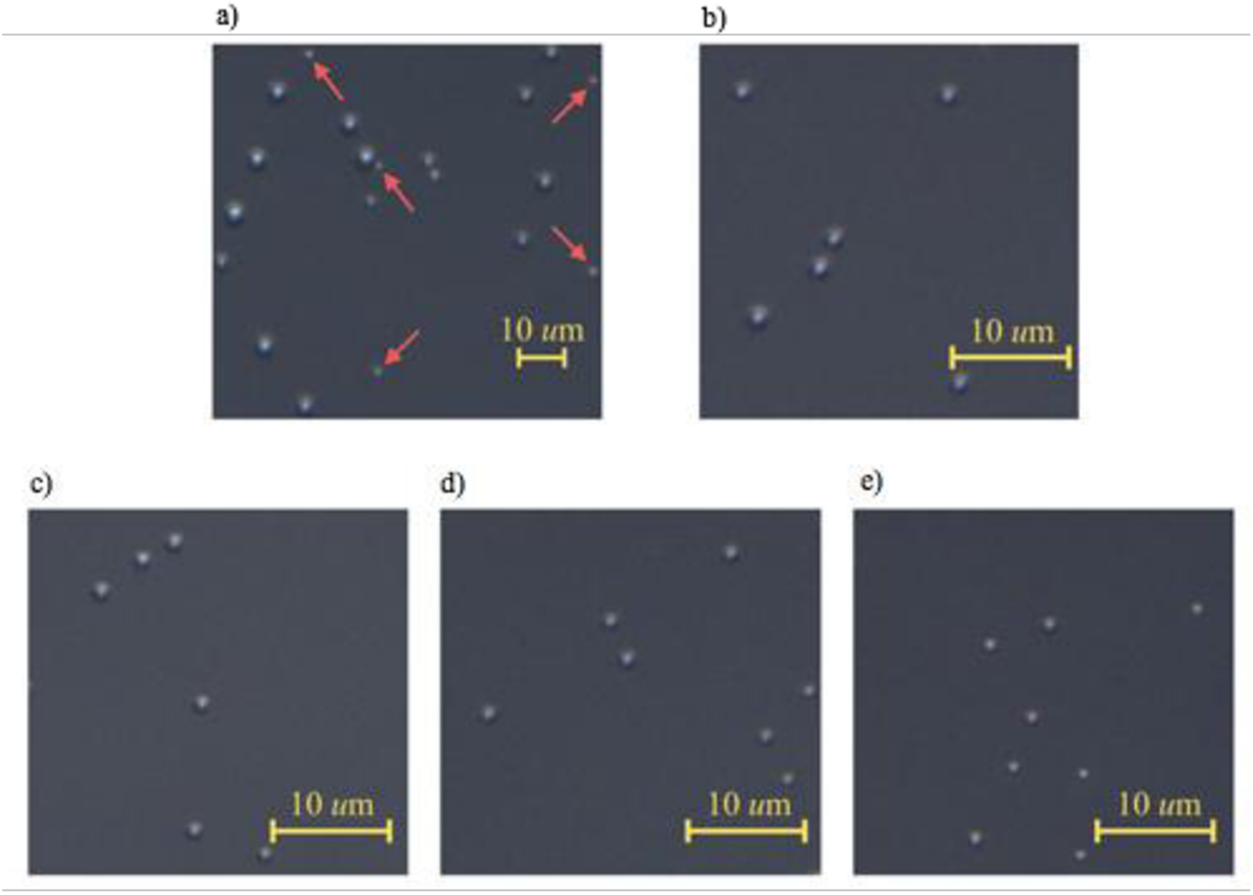

Figure 4.4 At a 20 times BSA molar excess of Traut's reagent, light microscope images of the BSA-SH MBs were taken after the centrifugal collection (a), 1 day (b), 2 days (c), 3 days (d), and 6 months (e). The sub-micron, short-lived portion of the synthesized microbubble was pointed out by red arrows (a).

(Figure 4b). The long-lived portion initially centered at 2.5 μm, on the other hand, gradually shrank in the days after the synthesis and eventually stabilized at the critical size of 850 nm (Figure 4b-d, 5b-d, S2b-d). Immediately after the synthesis, the concentration of BSA-SH MBs was measured to be $8.5 \pm 1.4 \times 10^7$ bubbles/ml, and it was dropped to $3.8 \pm 1.0 \times 10^7$ bubbles/ml within 3 days (Figure S3). The collapse of the sub-micron portion was the major driving force

lowering the overall concentration, but the stabilized long-lived portion was well maintained afterwards (Figure S3). The short lifetime of the 0.5 μm portion was attributed to its incomplete thiolation during the surface treatment. As a result, fewer thiols of the starting material gave rise to fewer cross-linkers of disulfide bonds in the synthesized microbubbles that easily collapsed under the Laplace pressure. In contrast, the long-lived portion of 2.5 μm with enough cross-linkers was able to sustain its spherical structure over time. The shrinkage of BSA-SH MBs was experimentally observed to be associated with the thickening of their shells; more specifically, the initial shell thickness of 155±20 nm gradually increased to 280±30 nm within a week, and then eventually stabilized at 290±25 nm (Figure 6b, S4e). The volume change of the shell materials (ΔV_{Shell}) could be roughly estimated by assuming BSA-SH MBs were perfectly spherical without losing shell materials during their shrinkage. Immediately after the synthesis, BSA-SH MBs, with an average radius of 1.25 μm and an average shell thickness of 155 nm, the shell volume (V_0) could be estimated using $V_0 \approx (1.25\ \mu m^3 - (1.25\text{-}0.155)\ \mu m^3)\ 4\pi/3 \approx 2.68\ \mu m^3$. Analogously, the shell volume of BSA-SH MBs after one week (V_1) was $V_1 \approx (0.425\ \mu m^3 - (0.425\text{-}0.29)\ \mu m^3)\ 4\pi/3 \approx 0.311\ \mu m^3$. It could be readily seen that their shell volume was greatly compressed along with the shrinkage of BSA-SH MBs, indicating the adoption of a more close-packed shell over time. As the dominant driving force of the bubble shrinkage, the Laplace pressure can be calculated using the Young-Laplace equation given as $\Delta P = 2\gamma/R$ where γ and R are the surface tension and spherical radius, respectively [40]. The measured surface tension of the thiolated BSA, BSA-SH, was determined to be 50.0 mN/m (Figure S5) and it was slightly lower than that of the untreated BSA, 51-53 mN/m [41, 42]. With a starting diameter of 2.5 μm, the Laplace pressure inside the newly synthesized microbubbles was 0.79 atm, which was considered to be the most probable driving force of the microbubble shrinkage. The condition of

the microbubble stabilization was reported to be $E_b > 2\sigma R/3d^2$, where E_b, σ, R, and d represent the bulk modulus of the shell, the interfacial tension between the air and solution, the radius of microbubbles, and the thickness of the shell [36, 43]. After the microbubble shrinkage, the bulk modulus of the shell was calculated to be at least 3.79E5 N/m^2 to stabilize microbubbles with a

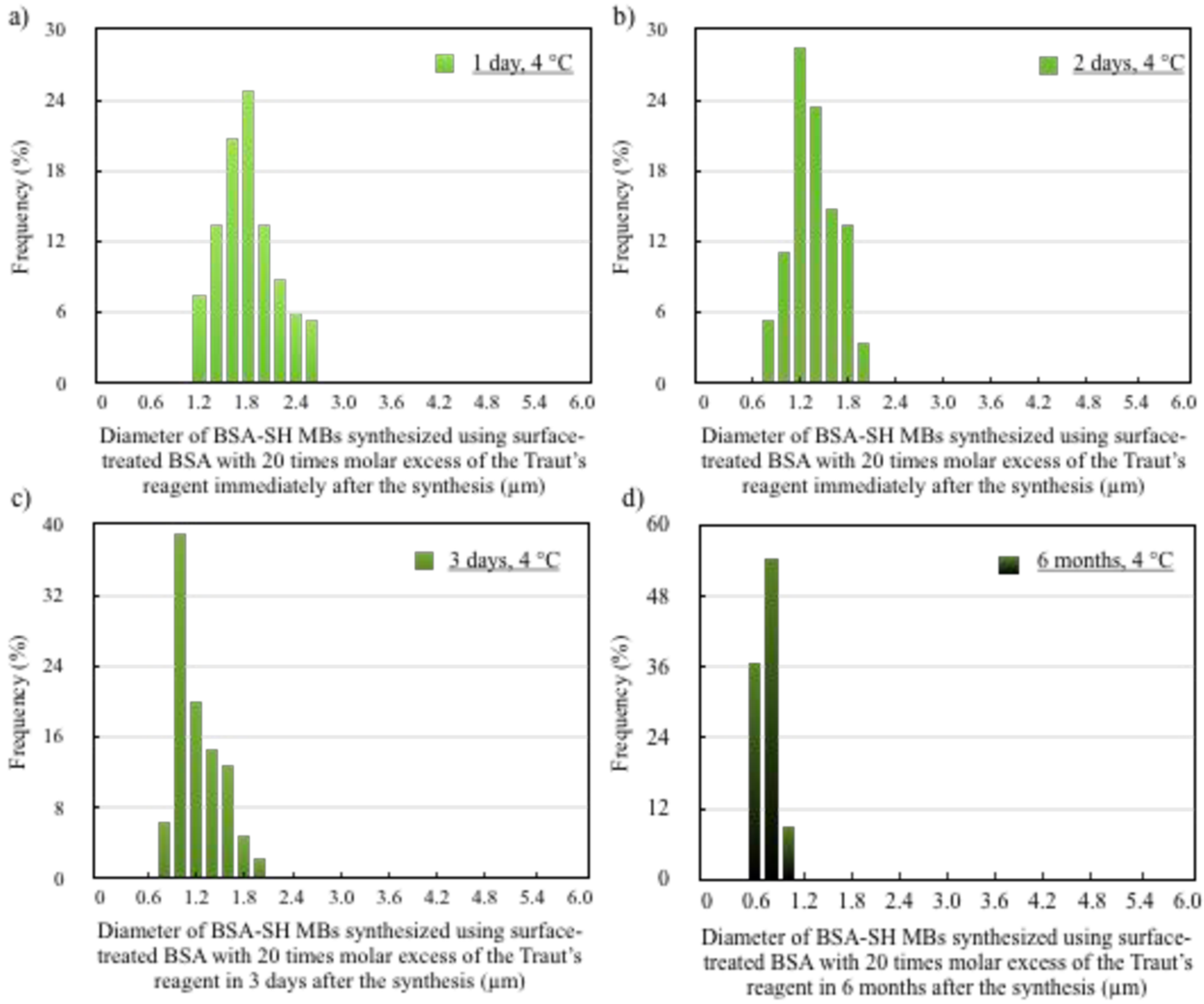

Figure 4.5 Temporal size distributions of BSA-SH MBs synthesized using the experimentally optimal ratio of Traut's reagent to BSA, 20 times were also recorded by image processing in 1 day (a), 2 days (b), 3 days (c), and 6 months (d) after the synthesis.

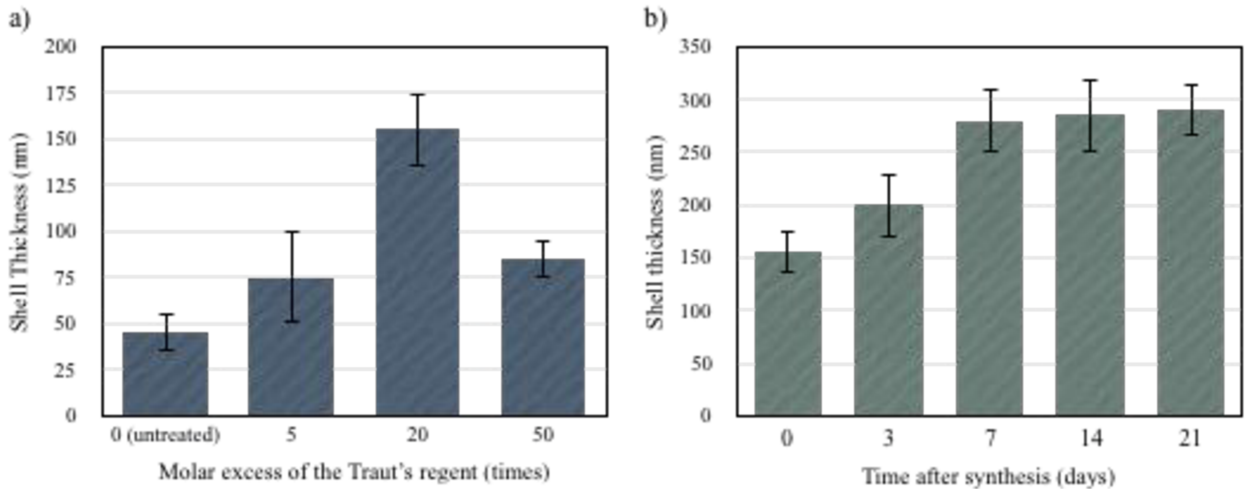

Figure 4.6 The measurements of shell thicknesses of microbubbles as a function of the molar excess of the Traut's Reagent (a) and time after the synthesis (b).

final diameter of 850 nm and a thickened shell of ~290 nm. Driven by the Laplace pressure, microbubbles continued to shrink until reaching their critical size where the Laplace pressure was eventually overcome by the thickened, more close-packed shell [44-46].

4.3.2 FTIR and XPS measurements of BSA-SH MBs

FTIR spectra of BSA, BSA-SH, and BSA-SH MBs were respectively recorded to track the changes in bonding throughout the synthesis of BSA-SH MBs (Figure 7). For a non-destructive quantitative analysis, the peak heights of amide I (C=O stretching) and amide II (C-N stretching and N-H bending) respectively at 1650 and 1532 cm^{-1} were manually fixed, and then the relative magnitude of other bonds was compared accordingly. Compared to the undetectable presence of free thiols in untreated BSA (Figure 7a), an appreciable increase in thiol content in BSA-SH (Figure 7b) was shown in the peak intensity at 2510 cm^{-1}, confirming the successful thiolation of

BSA. The slight shift of the experimental value from the literature value, typically in the region of 2550–2600 cm^{-1} [47], may arise from the abundant intra- and intermolecular hydrogen bondings [48]. Although the formation of BSA-SH MBs greatly consumed free thiols [24-28], there were still free thiols remaining on the surface shown with a reduced peak intensity at 2510 cm^{-1} (Figure 7c). The peaks of the C-N stretching and the CH_2 rocking vibrations of the primary amine at 1235 and 1390 cm^{-1}, respectively throughout the synthesis (Figure 7a-c) suggested the presence of the primary amine [49, 50]. Other major peaks at 1075, 3040, and 3381 were attributed to the C-O stretch of primary alcohol, the O-H stretch of carboxylic acid, and the O-H stretch of alcohols, respectively [49-51]. Based on the FTIR data, free thiols were successfully rendered onto BSA after the surface treatment, and partially consumed during the microbubble formation; on the other hand, the primary amines were present throughout the synthesis. High resolution XPS of S2p (Figure 8) and N1s (Figure 9) was conducted to track the changes in chemical bonding throughout the synthesis of BSA-SH MBs. For S2p spectra, the peaks were fitted using S2p doublets consisting of $S2p_{3/2}$ and $S2p_{1/2}$ with a 2:1 area ratio and a splitting of 1.2 eV according to the spin-orbit coupling [52, 53]. Before the thiolation, only disulfide bond was observed with the $S2p_{3/2}$ and $S2p_{1/2}$ peaks at 163.5 and 164.7, respectively (Figure 8a) [52, 54, 55].

After the surface treatment of BSA to BSA-SH, along with the pre-existing disulfide bond, free thiols appeared with the $S2p_{3/2}$ and $S2p_{1/2}$ peaks at 162.7 and 163.9, respectively (Figure 8b). In disulfide bond, sulfur was equipped with a negative charge of 1; however, in thiols, sulfur was reduced to a negative charge of 2, endowing a better ability to release the electron upon the X-ray excitation. The downward shifts of the $S2p_{3/2}$ and $S2p_{1/2}$ peaks were attributed to the higher

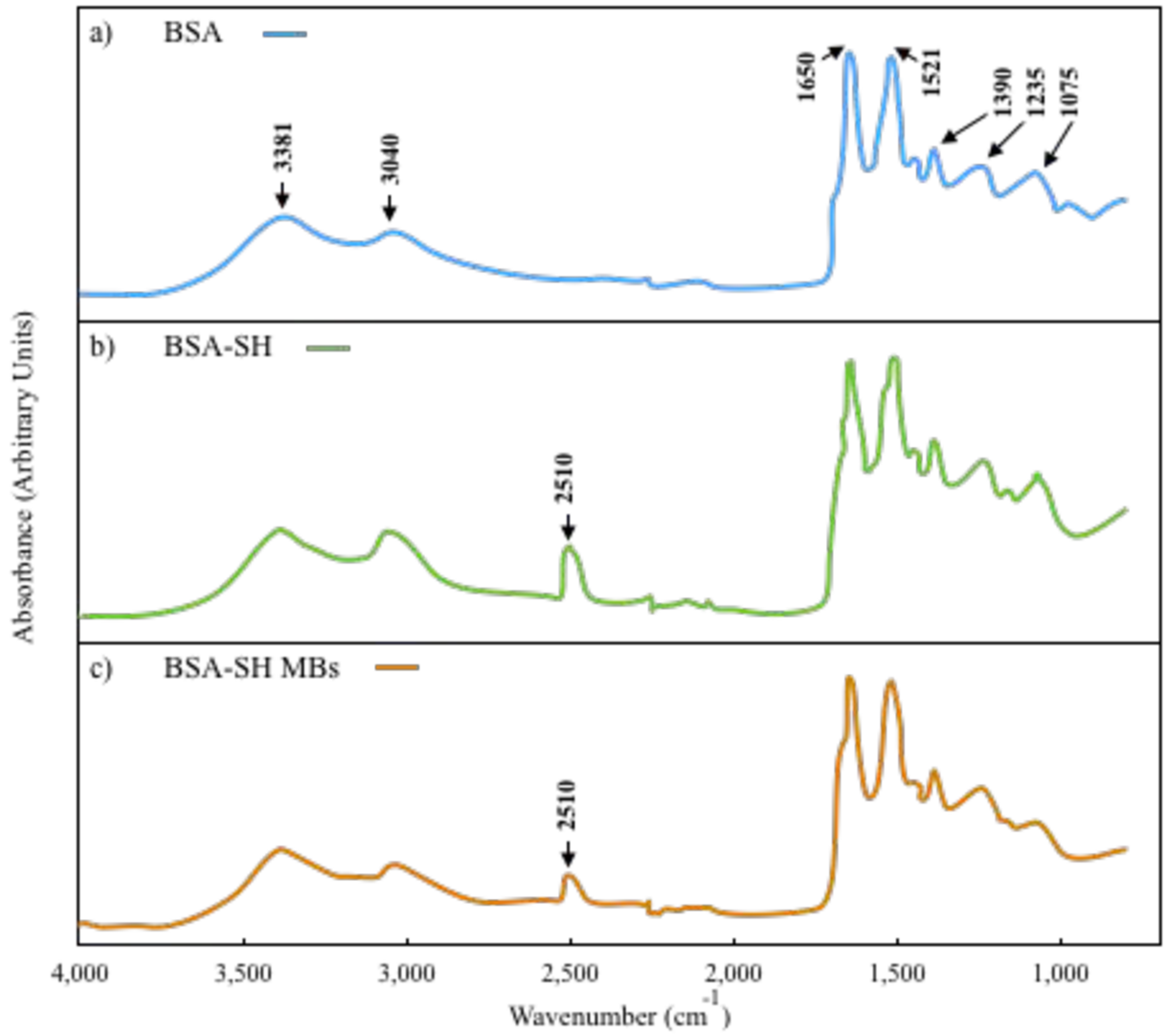

Figure 4.7 FTIR absorbance spectra of BSA (a), BSA-SH (b), and BSA-SH MBs (c).

electron-releasing tendency of the sulfur in thiols in comparison with that in the disulfide bond. After the synthesis of BSA-SH MBs, the mutual existence of disulfide bond and thiol were indicated by their $S2p_{3/2}$ and $S2p_{1/2}$ peaks at 163.5 and 164.7, and 162.7 and 163.9, respectively (Figure 8c). In addition to their co-existence, their relative amounts could be estimated by comparing the relative peak area of either their $S2p_{3/2}$ or $S2p_{1/2}$ peak. In specific, the content of free thiols was increased from indiscernible to 48.2 % (Figure 8a, b) after the surface thiolation,

and it was dropped to 26.3 % after the bubble synthesis (Figure 8b, c). In agreement with the FTIR analysis (Figure 7), the S2p spectra illustrated the successful thiolation that renders free thiols onto BSA and the remaining presence of free thiols albeit being partially consumed by the synthesis of BSA-SH MBs.

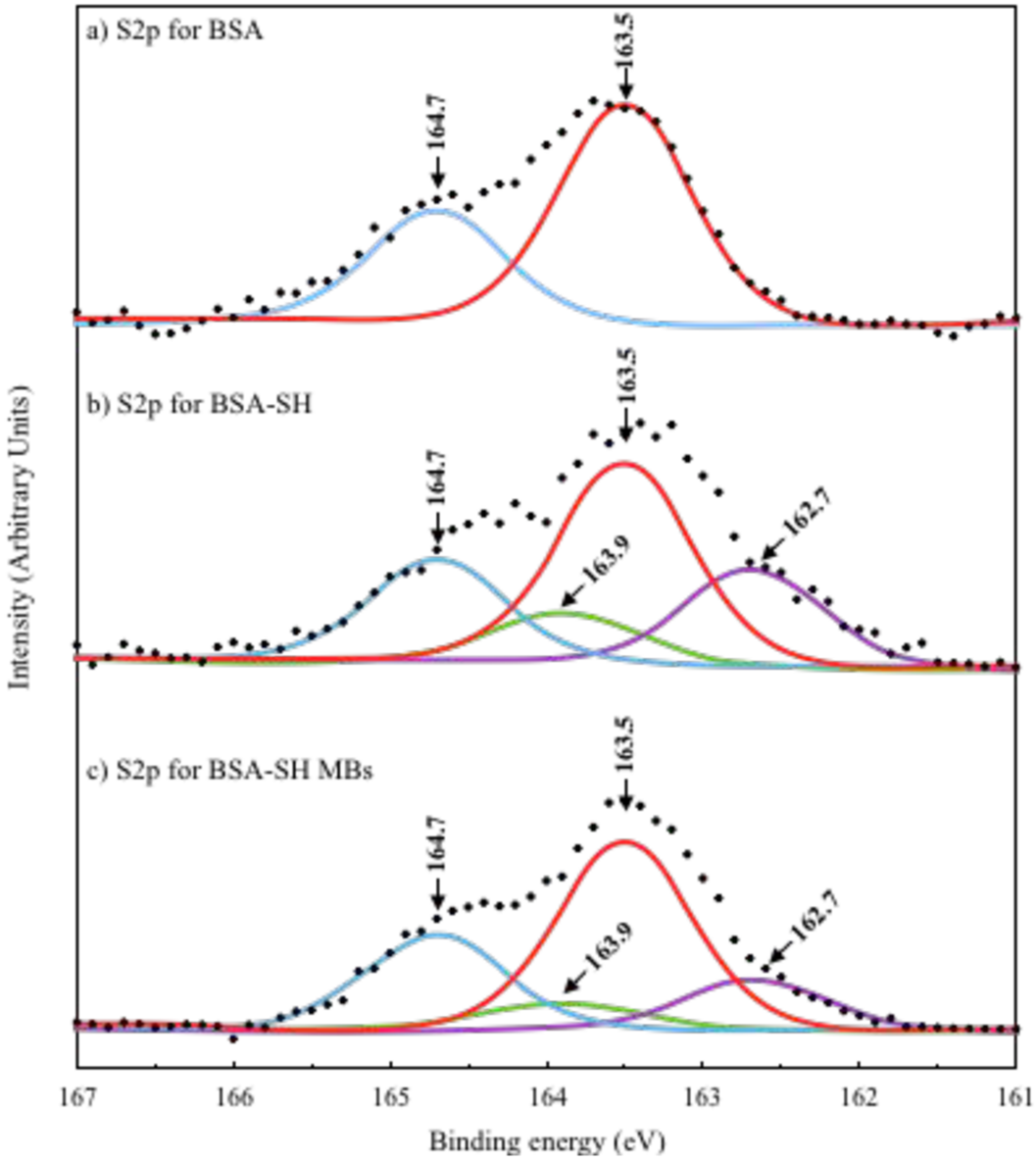

Figure 4.8 High resolution XPS spectra of S2p for BSA (a), BSA-SH (b), and BSA-SH MBs (c).

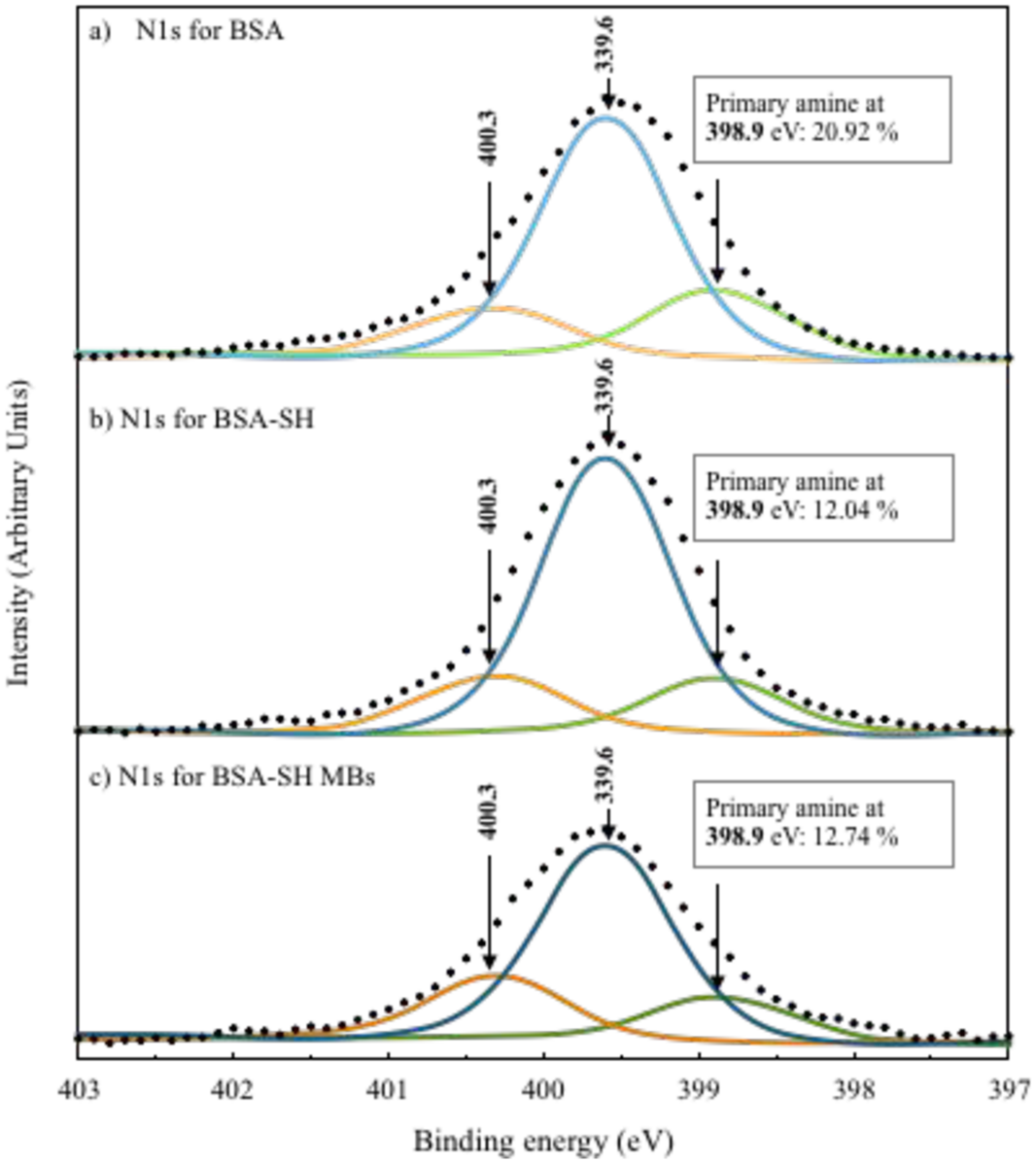

Figure 4.9 High resolution XPS spectra of N1s for BSA (a), BSA-SH (b), and BSA-SH MBs (c).

The binding energy peaks of the N1s spectra at 400.3, 399.6, and 398.9 eV correspond to H-bonded nitrogen, secondary amines, and primary amines, respectively (Figure 9) [52-58]. The partial consumption of primary amines was confirmed through a decrease in peak area at 398.9 eV from 20.92 to 12.04 % after the thiolation with Traut's reagent (Figure 9a, b). The subsequent

sonochemical formation of the microbubbles had a negligible effect on the content of primary amine from 12.04 to 12.74% (Figure 9b, c). At the optimal dosage of the Traut's reagent, 20 times molar excess, a partial conversion of primary amine to thiol occurred during the surface treatment of native BSA, and their co-existence after the synthesis of BSA-SH MBs was consistently indicated from the FTIR spectra (Figure 7) and XPS binding energies of S2p (Figure 8) and N1s (Figure 9).

4.3.3 Zeta potential and QCM-D adsorption measurements

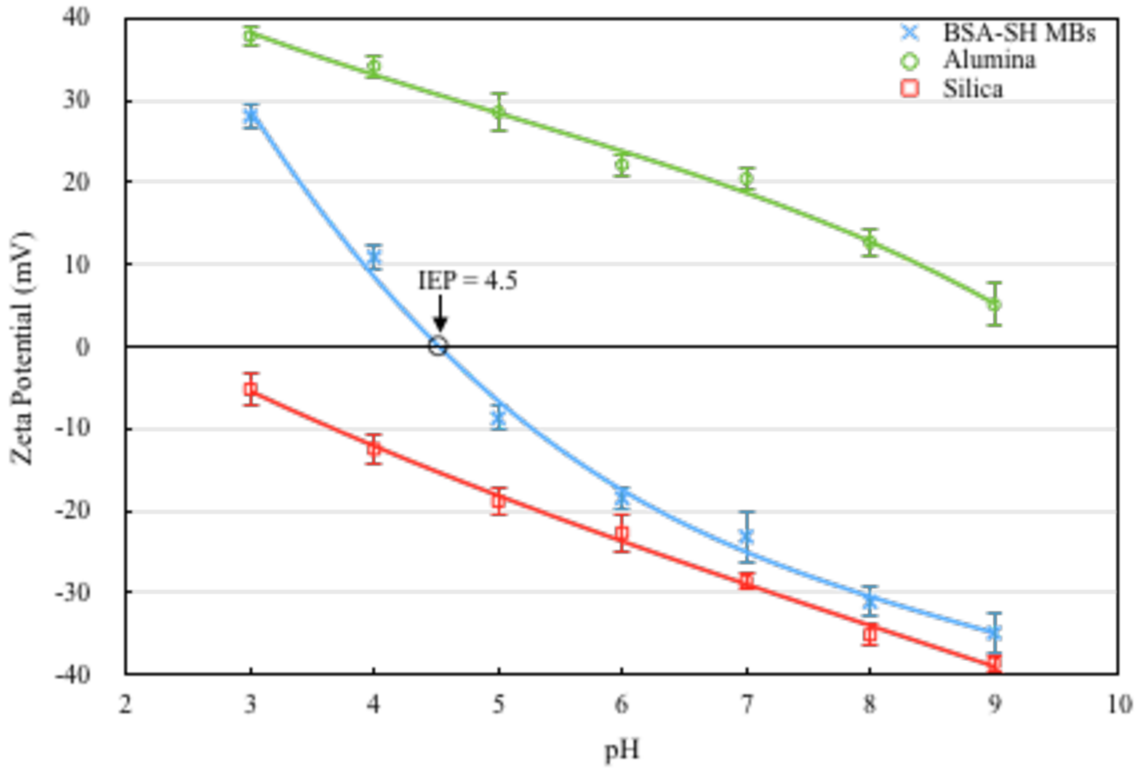

Figure 4.10 Zeta potential measurements of BSA-SH MBs, alumina and silica in a range from pH 3 to 9.

The zeta potentials of BSA-SH MBs were measured in a broad range of pH 3 to 9 (Figure 10). As the pH increases, the zeta potentials of BSA-SH MBs decreases, exhibiting the same trend of the native BSA [59]. The isoelectric point (IEP), referred to the pH where a molecule carries a zero net charge, was determined to be 4.5 for the synthesized BSA-SH MBs from the zeta potential measurement (Figure 10). The IEP of native BSA is theoretically reduced from 5.6 to 4.1 if a complete conversion occurs from primary amine-containing lysine with a pKa of 9.7 to thiol-containing cysteine with a pKa of 5.1 [60, 61]. The difference between the measured and theoretical values might be attributed to an incomplete conversion of the primary amines to thiols as shown by FTIR (Figure 7) and XPS (Figure 8, 9) analyses. Also, zeta potential measurements of two common metal oxide nanoparticles (alumina and silica) were also performed to demonstrate the opposite signs of zeta potentials to BSA-SH MBs and thus the possible electrostatic interactions over certain pH regions. Consistent with the literature values [62-66], alumina and silica nanoparticles were measured to be positively and negatively charged, respectively from pH 3 to 9 (Figure 10). It could be readily seen that, below its IEP of 4.5, BSA-SH MBs favor an electrostatic interaction with the negatively charged silica while, above its IEP, BSA-SH MBs are expected to interact with the positively charged alumina.

To probe the reactivity of BSA-SH MBs, QCM-D adsorption tests were performed; specifically, BSA-SH MBs were introduced onto alumina (Figure 11a) and silica (Figure 11c) surfaces at certain pH regions by electrostatic interactions and onto gold surfaces (Figure 11e) by the gold-thiol bonding effect. The Sauerbrey equation states that the mass adsorbed on a piezoelectric crystal and its resonant frequency are inversely related; in other words, a decline of the resonance frequency indicates the occurrence of adsorption [67]. Extensive adsorptions of BSA-SH MBs

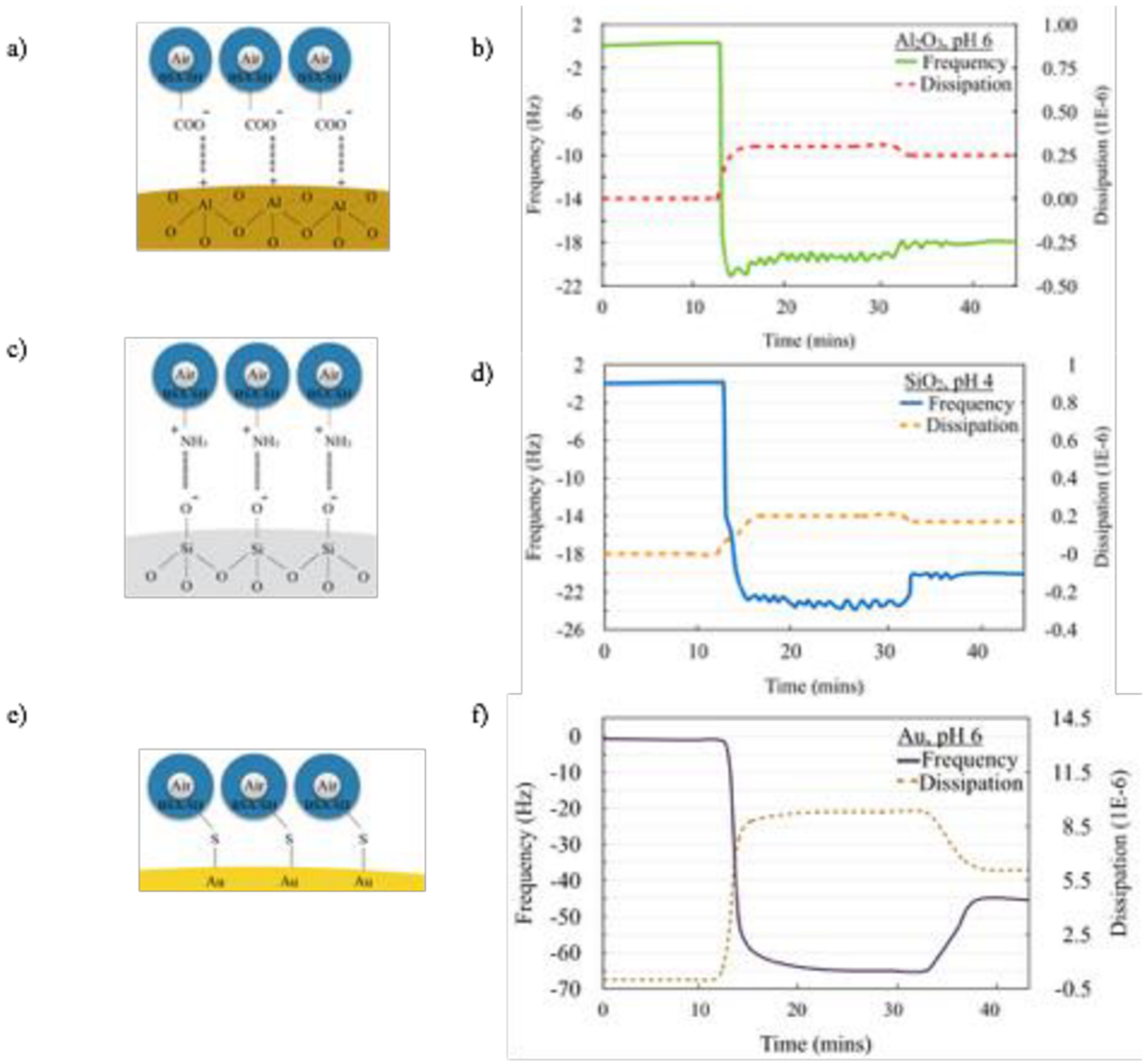

Figure 4.11 Schematics for the interaction mechanism and QCM-D adsorption tests of BSA-SH MBs on alumina sensor at pH 6 (a, b), silica sensor at pH 4 (c, d), on gold sensor at pH 6 (e, f).

on an alumina sensor at pH 6 (Figure 11b) and on a silica sensor at pH 4 (Figure 11d) were confirmed through significant drops in frequency after the injection at 10 min. Immediately following the drop, both sensors underwent a zig-zag fluctuation of frequencies before they were rinsed off with the background solution at 30 min, revealing a dynamic interaction between microbubbles and sensor. Free microbubbles constantly compete with and replace a small

portion of the loosely-bound microbubbles on the sensor, reaching a dynamic equilibrium. The slight increment in frequency at 30 min on both sensors depicts the injection of background solution which removed loosely-bound microbubbles. The pH values were selected to create opposite charges between BSA-SH MBs and the sensors. At pH 6, BSA-SH MBs with an IEP of 4.5 carry a negative charge while the alumina sensor is positively charged; the oppositely charged surfaces favor adsorption. Analogously, the strong interaction at pH 4 between positively charged BSA-SH MBs and a negatively charged silica sensor is shown as a sharp decrease in frequency (Figure 11d). At pH 10, both the BSA-SH MBs and the alumina sensor are negatively charged, leading to a minor, unspecific adsorption (Figure S6a). Similarly, no appreciable adsorption was observed between BSA-SH MBs and the silica sensor at pH 4, a value at which both surfaces are positively charged (Figure S6b). Regarding the viscoelastic properties of the adsorbed BSA-SH MBs, a large-scale adsorption (Figure 11b, d), in comparison with a minor adsorption (Figure S6a, b), gave rise to a larger increment of dissipation which was positively related to their viscoelasticity. To test the reactivity of the surface thiols, BSA-SH MBs were also introduced to react with the gold sensor at pH 6 where both the microbubbles and the gold sensor (IEP = 5.2) [68] are negatively charged excluding the possibility of electrostatic interactions. A significant degree of adsorption of BSA-SH MBs, as well as a dramatically increased viscoelasticity were observed on a gold sensor (Figure 11f). Compared to the charge neutralization in the previous scenarios (Figure 11a-d), the strong bonding effect between gold and thiol might explain the greater magnitude (Figure 11e, f) of the interaction between BSA-SH MBs and gold surface [52, 69-71]. Also, no zig-zag fluctuation of frequencies was observed for the adsorption of BSA-SH MBs on the gold sensor, further indicating the strong gold-thiol bond without any appreciable competing effect from the free microbubbles. Based on the QCM-D

tests, the reactivities of carboxylic and amine groups of BSA-SH MBs were indirectly testified through electrostatic attachments onto the alumina and silica sensors; in addition, the reactivity of the surface thiol groups was directly proved by reacting with the gold sensor. With these reactive functional groups on their surfaces, BSA-SH MBs could be used to load drug molecules through either bond formation or electrostatic interactions. Alternatively, BSA-SH MBs could be directly used to remove metal nanoparticles from wastewater through column flotation. As shown from the QCM-D tests, these synthesized microbubbles have great affinity to metal surfaces; therefore, they can collect metal or metal ions as they float from the bottom to the top of a wastewater column. The novel, facile synthesis of stable proteinaceous microbubbles provides opportunities of expanding their utilizations in either drug delivery or wastewater treatment. Moreover, these microbubbles exhibit an acoustic attenuation coefficient in the order of magnitude of conventional microbubbles [72, 73] (0.53 dB/cm at 3.3 MHz, measurements detailed in the SI) suggesting possible applications in acoustic imaging.

4.4 Conclusions

A facile synthesis of proteinaceous microbubbles with an increased stability was demonstrated using the surface-thiolated BSA with the Traut's reagent. At the optimal molar excess of the Traut's reagent, 20 times, BSA-SH MBs showed an initial size distribution that peaked at 2.5 and 0.5 μm, respectively. The 0.5 μm portion vanished within three days, and the 2.5 μm portion gradually shrank to and eventually stabilized at 850 nm for several months. FTIR spectra and XPS analyses showed the thiol, primary amine, and carboxylic groups on the surface of BSA-SH MBs, and these functional groups were proved to be reactive via the QCM-D adsorptions tests.

Based on these reactive functional groups, applications of BSA-SH MB in drug delivery and water purification could be further exploited through either electrostatic interactions or bond formations.

4.5 References

[1] Blomley, M. and D. Cosgrove, Microbubble echo-enhancers: a new direction for ultrasound? The Lancet, 1997. 349(9069): 1855-1856.

[2] Cosgrove, D., Echo enhancers and ultrasound imaging. European journal of radiology, 1997. 26(1): 64-76.

[3] Calliada, F., et al., Ultrasound contrast agents: basic principles. European journal of radiology, 1998. 27: S157-S160.

[4] Lentacker, I., et al., Ultrasound-responsive polymer-coated microbubbles that bind and protect DNA. Langmuir, 2006. 22(17): 7273-7278.

[5] Ferrara, K., R. Pollard, and M. Borden, Ultrasound microbubble contrast agents: fundamentals and application to gene and drug delivery. Biomedical Engineering, 2007. 9.

[6] Cosgrove, D. and C. Harvey, Clinical uses of microbubbles in diagnosis and treatment. Medical & biological engineering & computing, 2009. 47(8): 813-826.

[7] Ferrara, K.W., M.A. Borden, and H. Zhang, Lipid-shelled vehicles: engineering for ultrasound molecular imaging and drug delivery. Accounts of chemical research, 2009. 42(7): 881-892.

[8] Qin, S., C.F. Caskey, and K.W. Ferrara, Ultrasound contrast microbubbles in imaging and therapy: physical principles and engineering. Physics in medicine and biology, 2009. 54(6): R27.

[9] Yang, F., et al., Superparamagnetic iron oxide nanoparticle-embedded encapsulated microbubbles as dual contrast agents of magnetic resonance and ultrasound imaging. Biomaterials, 2009. 30(23): 3882-3890.

[10] Park, J.I., et al., Microbubbles loaded with nanoparticles: a route to multiple imaging modalities. Acs Nano, 2010. 4(11): 6579-6586.

[11] Kiessling, F., et al., Ultrasound microbubbles for molecular diagnosis, therapy, and theranostics. Journal of nuclear medicine, 2012. 53(3): 345-348.

[12] Ishikawa, H., et al., Inactivation of Bacillus spores by the supercritical carbon dioxide micro-bubble method. Bioscience, biotechnology, and biochemistry, 1997. 61(6): 1022-1023.

[13] Kobayashi, F., et al., Inactivation of Escherichia coli by CO2 microbubbles at a lower pressure and near room temperature. Transactions of the ASABE, 2009. 52(5): p. 1621-1626.

[14] Suslick, K.S., Sonochemistry. science, 1990. 247(4949): 1439-1445.

[15] Xu, Q., et al., A comparative study of microbubble generation by mechanical agitation and sonication. Innovative Food Science & Emerging Technologies, 2008. 9(4): 489-494.

[16] Epstein, c.e.P. and M.S. Plesset, On the Stability of Gas Bubbles in Liquid-Gas Solutions. The Journal of Chemical Physics, 1950. 18(11): 1505-1509.

[17] Kloek, W., T. van Vliet, and M. Meinders, Effect of bulk and interfacial rheological properties on bubble dissolution. Journal of Colloid and Interface Science, 2001. 237(2): 158-166.

[18] Kabalnov, A., et al., Dissolution of multicomponent microbubbles in the bloodstream: 1. Theory. Ultrasound in medicine & biology, 1998. 24(5): 739-749.

[19] Lemlich, R., Prediction of changes in bubble size distribution due to interbubble gas diffusion in foam. Industrial & Engineering Chemistry Fundamentals, 1978. 17(2): 89-93.

[20] Binks, B.P., Modern aspects of emulsion science. 1998: Royal Society of Chemistry.

[21] Taylor, P., Ostwald ripening in emulsions. Advances in colloid and interface science, 1998. 75(2): 107-163.

[22] Chatterjee, D. and K. Sarkar, A Newtonian rheological model for the interface of microbubble contrast agents. Ultrasound in Medicine and Biology, 2003. 29(12): 1749-1757.

[23] Barak, M. and Y. Katz, Microbubbles - Pathophysiology and clinical implications. Chest, 2005. 128(4): 2918-2932.

[24] Talu, E., et al., Long-term stability by lipid coating monodisperse microbubbles formed by a flow-focusing device. Langmuir, 2006. 22(23): 9487-9490.

[25] Cavalieri, F., et al., Ultrasonic synthesis of stable, functional lysozyme microbubbles. Langmuir, 2008. 24(18): 10078-10083.

[26] Grinstaff, M.W. and K.S. Suslick, Air-filled proteinaceous microbubbles: synthesis of an echo-contrast agent. Proceedings of the National Academy of Sciences, 1991. 88(17): 7708-7710.

[27] Cavalieri, F., et al., One-pot ultrasonic synthesis of multifunctional microbubbles and microcapsules using synthetic thiolated macromolecules. Chemical Communications, 2011. 47(14): 4096-4098.

[28] Vong, F., et al., A comparison of the physical properties of ultrasonically synthesized lysozyme-and BSA-shelled microbubbles. Ultrasonics sonochemistry, 2014. 21(1): 23-28.

[29] Traut, R.R., et al., Methyl 4-mercaptobutyrimidate as a cleavable crosslinking reagent and its application to the Escherichia coli 30S ribosome. Biochemistry, 1973. 12(17): 3266-3273.

[30] Tarbell, D., The mechanism of oxidation of thiols to disulfides. Organic sulfur compounds, 1961. 1: 97-102.

[31] Jue, R., et al., Addition of sulfhydryl groups of Escherichia coli ribosomes by protein modification with 2-iminothiolane (methyl 4-mercaptobutyrimidate). Biochemistry, 1978. 17(25): 5399-5406.

[32] Clark, A., et al., ELECTRON MICROSCOPY OF NETWORK STRUCTURES IN THERMALLY-INDUCED GLOBULAR PROTEIN GELS. International Journal of Peptide and Protein Research, 1981. 17(3): 380-392.

[33] Takeda, K., et al., Conformational change of bovine serum albumin by heat treatment. Journal of protein chemistry, 1989. 8(5): p. 653-659.

[34] Yamasaki, M., H. Yano, and K. Aoki, Differential scanning calorimetric studies on bovine serum albumin: II. Effects of neutral salts and urea. International journal of biological macromolecules, 1991. 13(6): p. 322-328.

[35] Feshitan, J.A., et al., Microbubble size isolation by differential centrifugation. Journal of colloid and interface science, 2009. 329(2): 316-324.

[36] Rovers, T.A., et al., Temperature is key to yield and stability of BSA stabilized microbubbles. Food Hydrocolloids, 2016. 52: 106-115.

[37] Abràmoff, M.D., P.J. Magalhães, and S.J. Ram, Image processing with ImageJ. Biophotonics international, 2004. 11(7): 36-42.

[38] Gedanken, A., Preparation and properties of proteinaceous microspheres made sonochemically. Chemistry–A European Journal, 2008. 14(13): 3840-3853.

[39] Sirsi, S., et al., Lung surfactant microbubbles. Soft Matter, 2009. 5(23): 4835-4842.

[40] Graf, K. and M. Kappl, Physics and chemistry of interfaces. 2006: John Wiley & Sons.

[41] Tripp, B.C., J.J. Magda, and J.D. Andrade, Adsorption of globular proteins at the air/water interface as measured via dynamic surface tension: concentration dependence, mass-transfer considerations, and adsorption kinetics. Journal of colloid and interface science, 1995. 173(1): 16-27.

[42] McClellan, S.J. and E.I. Franses, Effect of concentration and denaturation on adsorption and surface tension of bovine serum albumin. Colloids and Surfaces B: Biointerfaces, 2003. 28(1): 63-75.

[43] Meinders, M.B. and T. van Vliet, The role of interfacial rheological properties on Ostwald ripening in emulsions. Advances in colloid and interface science, 2004. 108: 119-126.

[44] Du, Z., et al., Outstanding stability of particle-stabilized bubbles. Langmuir, 2003. 19(8): 3106-3108.

[45] Subramaniam, A.B., et al., Colloid science: Non-spherical bubbles. Nature, 2005. 438(7070): 930-930.

[46] Azmin, M., et al., Dissolution of coated microbubbles: the effect of nanoparticles and surfactant concentration. Materials Science and Engineering: C, 2012. 32(8): 2654-2658.

[47] Tingaut, P., R. Hauert, and T. Zimmermann, Highly efficient and straightforward functionalization of cellulose films with thiol-ene click chemistry. Journal of Materials Chemistry, 2011. 21(40): 16066-16076.

[48] Desiraju, G.R. and T. Steiner, The weak hydrogen bond: in structural chemistry and biology. Vol. 9. 2001: Oxford University Press on Demand.

[49] Stewart, J.E., Vibrational spectra of primary and secondary aliphatic amines. The Journal of Chemical Physics, 1959. 30(5): 1259-1265.

[50] Barth, A., The infrared absorption of amino acid side chains. Progress in biophysics and molecular biology, 2000. 74(3): 141-173.

[51] Socrates, G., Infrared and Raman characteristic group frequencies: tables and charts. 2004: John Wiley & Sons.

[52] Castner, D.G., K. Hinds, and D.W. Grainger, X-ray photoelectron spectroscopy sulfur 2p study of organic thiol and disulfide binding interactions with gold surfaces. Langmuir, 1996. 12(21): 5083-5086.

[53] Ishida, T., et al., High resolution X-ray photoelectron spectroscopy measurements of octadecanethiol self-assembled monolayers on Au (111). Langmuir, 1998. 14(8): 2092-2096.

[54] Bain, C.D., H.A. Biebuyck, and G.M. Whitesides, Comparison of self-assembled monolayers on gold: coadsorption of thiols and disulfides. Langmuir, 1989. 5(3): 723-727.

[55] Nazari, A.M., P.W. Cox, and K.E. Waters, Copper ion removal from dilute solutions using ultrasonically synthesised BSA-and EWP-coated air bubbles. Separation and Purification Technology, 2014. 132: 218-225.

[56] Zhang, F. and M. Srinivasan, Self-assembled molecular films of aminosilanes and their immobilization capacities. Langmuir, 2004. 20(6): 2309-2314.

[57] Eby, D.M., et al., Probing the molecular structure of antimicrobial peptide-mediated silica condensation using X-ray photoelectron spectroscopy. Journal of Materials Chemistry, 2012. 22(19): 9875-9883.

[58] Yu, B., et al., Functionalized graphene oxide/phosphoramide oligomer hybrids flame retardant prepared via in situ polymerization for improving the fire safety of polypropylene. RSC Advances, 2014. 4(60): 31782-31794.

[59] Rezwan, K., et al., Bovine serum albumin adsorption onto colloidal Al2O3 particles: A new model based on Zeta potential and UV-Vis measurements. Langmuir, 2004. 20(23): 10055-10061.

[60] Vogi, R. and D. Oreopoulos, Amino acid sequence in bovine serum albumin. Clin. Chim. Acta, 1973. 48: 353.

[61] Huang, B.X., H.-Y. Kim, and C. Dass, Probing three-dimensional structure of bovine serum albumin by chemical cross-linking and mass spectrometry. Journal of the American Society for Mass Spectrometry, 2004. 15(8): 1237-1247.

[62] Parks, G.A., The isoelectric points of solid oxides, solid hydroxides, and aqueous hydroxo complex systems. Chemical Reviews, 1965. 65(2): 177-198.

[63] Sprycha, R., Electrical double layer at alumina/electrolyte interface: I. Surface charge and zeta potential. Journal of colloid and interface science, 1989. 127(1): 1-11.

[64] Kosmulski, M., Chemical properties of material surfaces. Vol. 102. 2001: CRC press.

[65] Júnior, J.A.A. and J.B. Baldo, The behavior of zeta potential of silica suspensions. New Journal of Glass and Ceramics, 2014. 4(02): 29.

[66] Rajan, Y.C., B.S. Inbaraj, and B.H. Chen, Synthesis and characterization of poly (γ-glutamic acid)-based alumina nanoparticles with their protein adsorption efficiency and cytotoxicity towards human prostate cancer cells. RSC Advances, 2015. 5(20): 15126-15139.

[67] Sauerbrey, G., Verwendung von Schwingquarzen zur Wägung dünner Schichten und zur Mikrowägung. Zeitschrift für physik, 1959. 155(2): 206-222.

[68] Phan, H.T., et al., Investigation of bovine serum albumin (BSA) attachment onto self-assembled monolayers (SAMs) using combinatorial quartz crystal microbalance with dissipation (QCM-D) and spectroscopic ellipsometry (SE). PloS one, 2015. 10(10): e0141282.

[69] Grönbeck, H., A. Curioni, and W. Andreoni, Thiols and disulfides on the Au (111) surface: The headgroup-gold interaction. Journal of the American Chemical Society, 2000. 122(16): 3839-3842.

[70] Li, T., et al., Characterization of floc size, strength and structure under various coagulation mechanisms. Powder technology, 2006. 168(2): 104-110.

[71] Jadzinsky, P.D., et al., Structure of a thiol monolayer-protected gold nanoparticle at 1.1 Å resolution. Science, 2007. 318(5849): 430-433.

[72] De Jong, N., et al., Ultrasonic characterization of ultrasound contrast agents. Medical & biological engineering & computing, 2009. 47(8): 861-873.

[73] Raymond, J.L., et al., Broadband attenuation measurements of phospholipid-shelled ultrasound contrast agents. Ultrasound in medicine & biology, 2014. 40(2): 410-421.

4.6 Supplemental Information

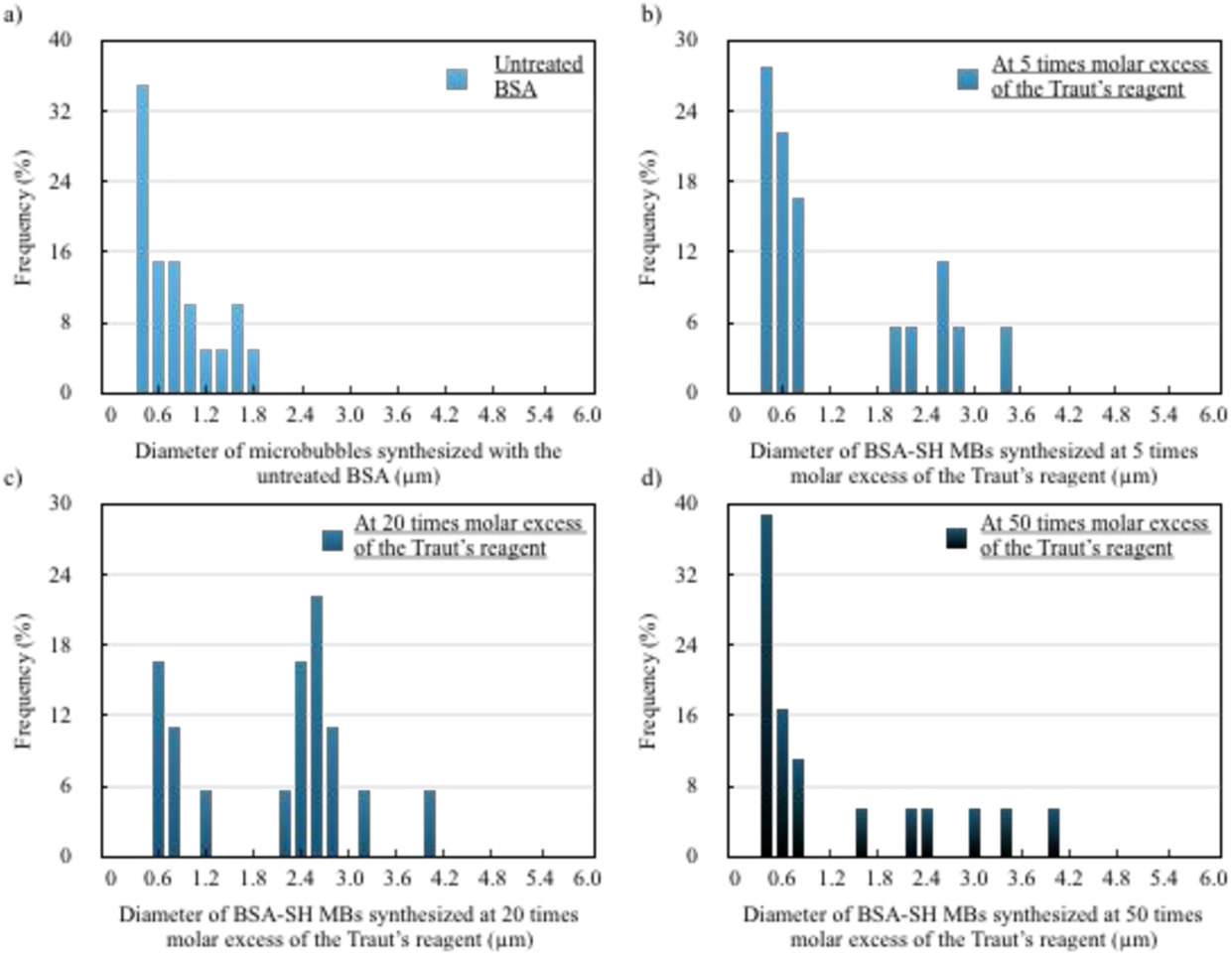

Figure 4.S1 Spatial size distributions of microbubbles synthesized with BSA (a), BSA treated with 5 (b), 20 (c), and 50 (d) times molar excess of Traut's reagent were obtained by dynamic light scattering immediately after the centrifugal collection.

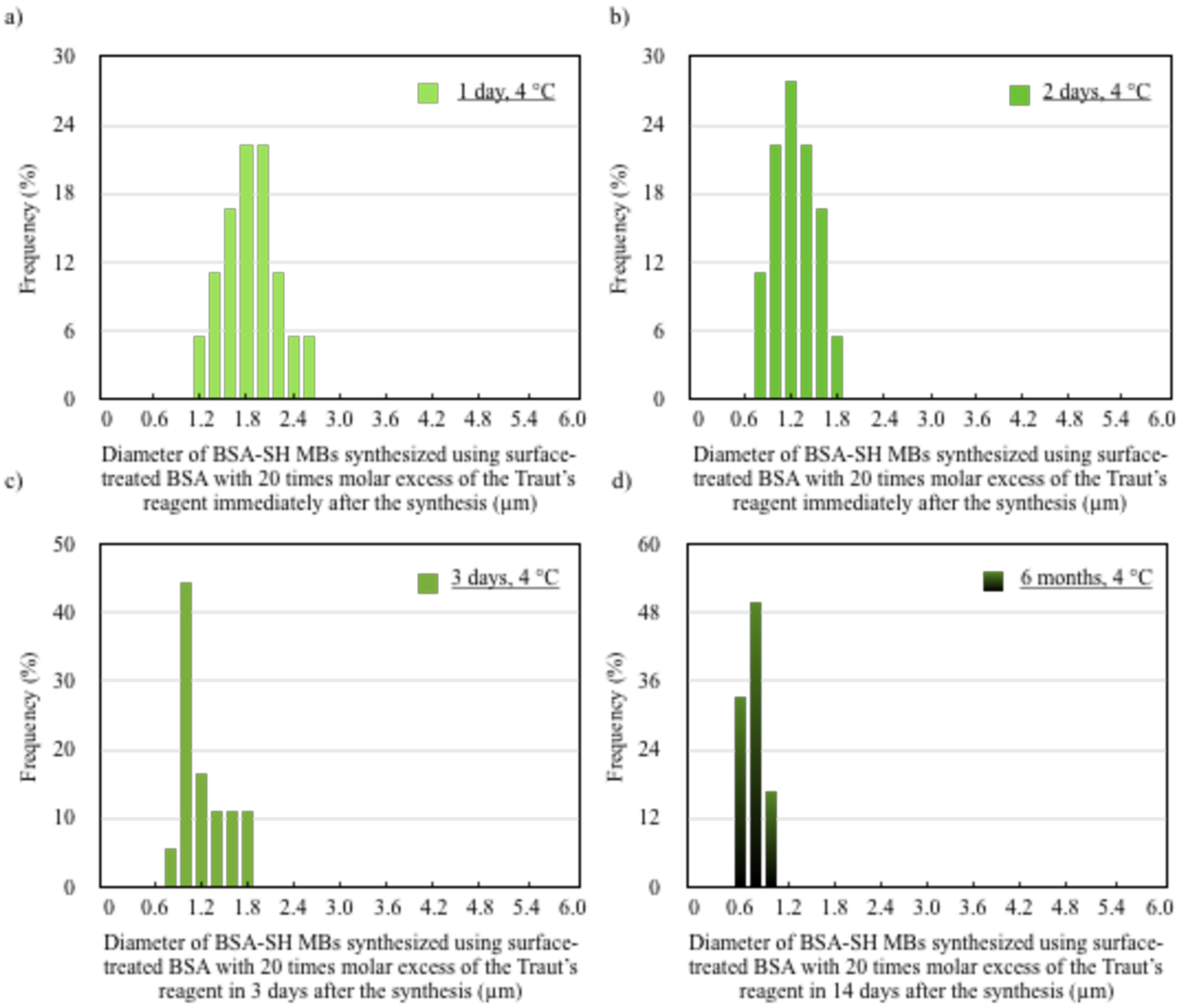

Figure 4.S2 Temporal size distributions of BSA-SH MBs synthesized using the optimal ratio of Traut's reagent to BSA, 20 times molar excess were recorded using dynamic light scattering in 1 day (a), 2 days (b), 3 days (c), and 6 months (d) after the synthesis.

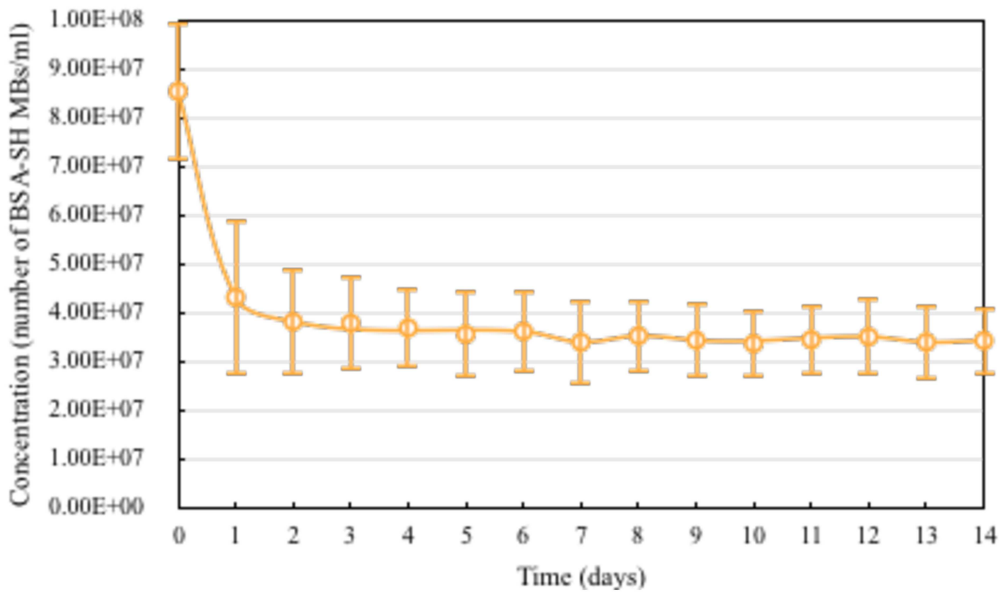

Figure 4.S3 Measurements of the concentration of BSA-SH MBs with respect to time

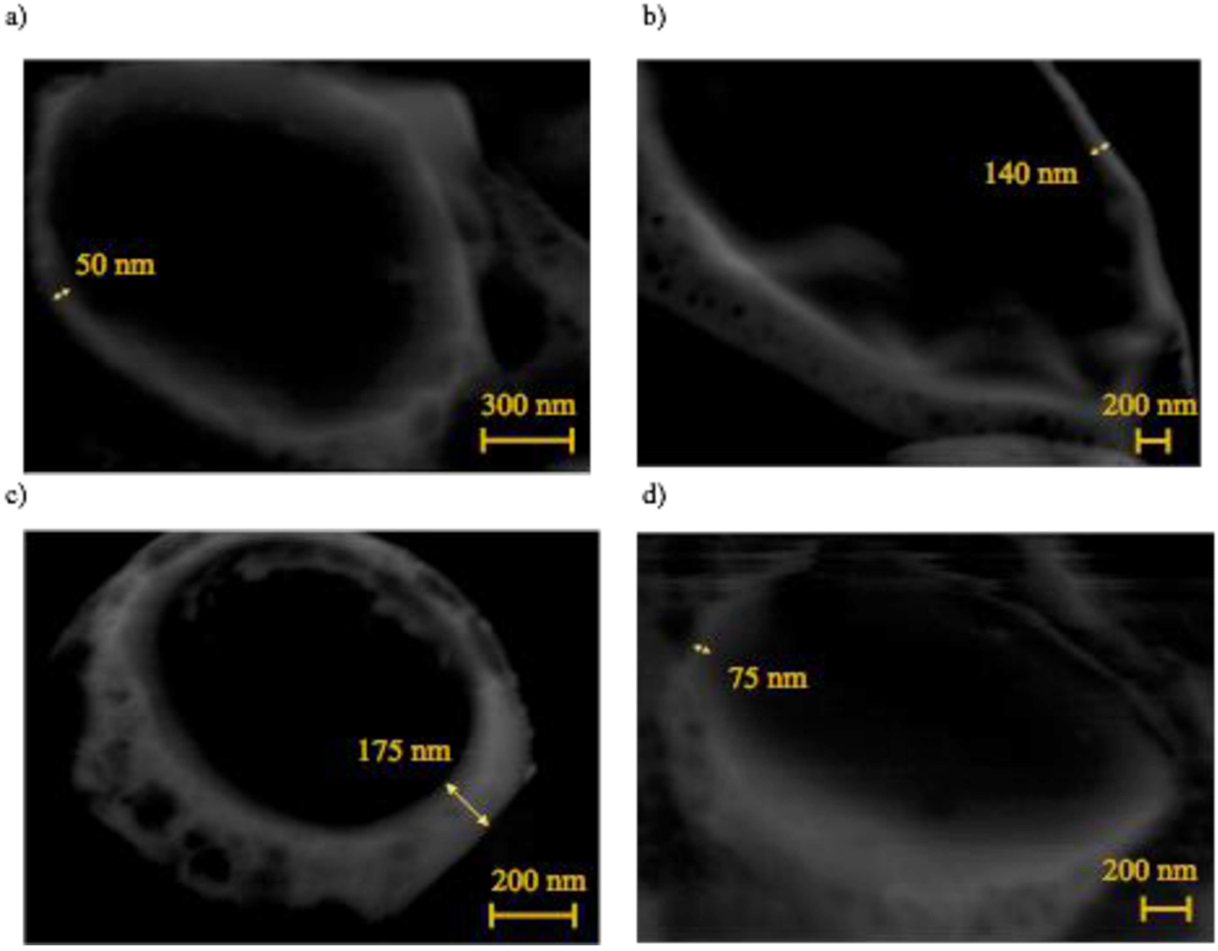

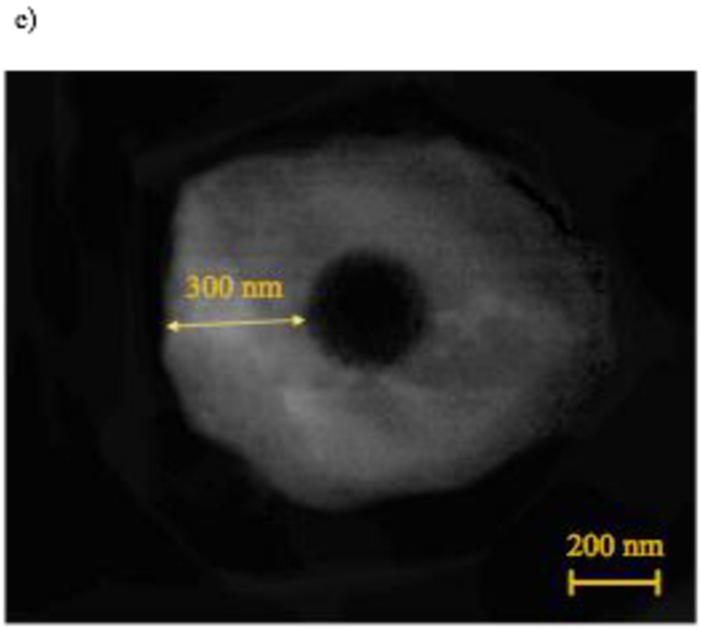

Figure 4.S4. Measurements of shell thickness of microbubbles at untreated (a), 5 (b), 20 (c), 50 (d) times molar excess of the Traut's reagent were shown respectively. At 20 times molar excess of the Traut's reagent, the shell thickness was also recorded after 14 days (e).

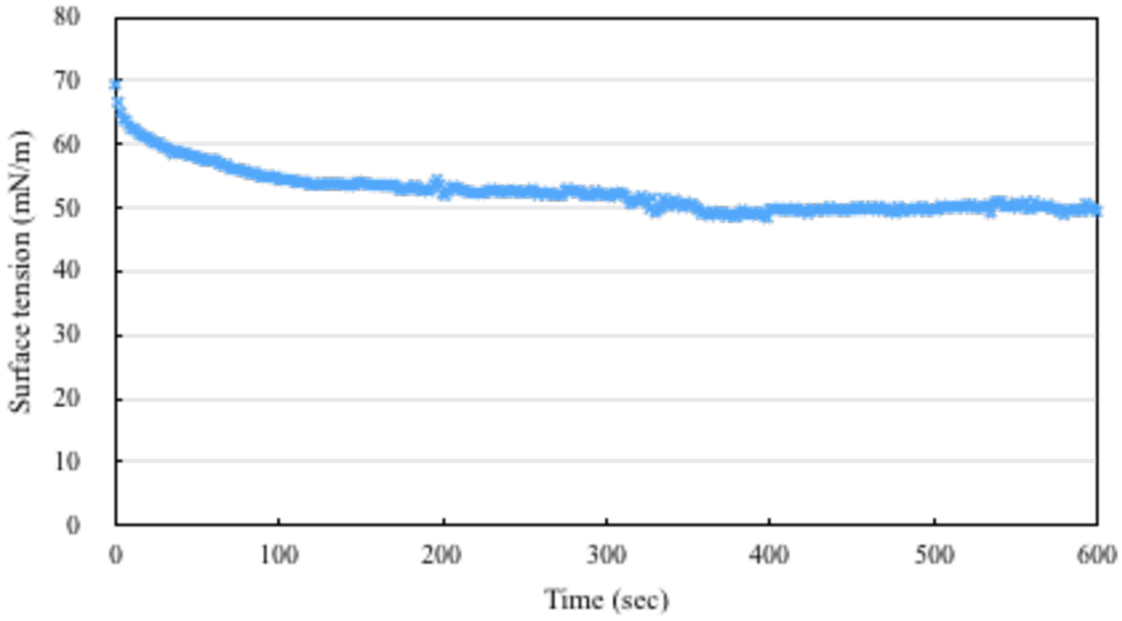

Figure 4.S5. The measurement of surface tension of the surface-thiolated BSA (BSA-SH)

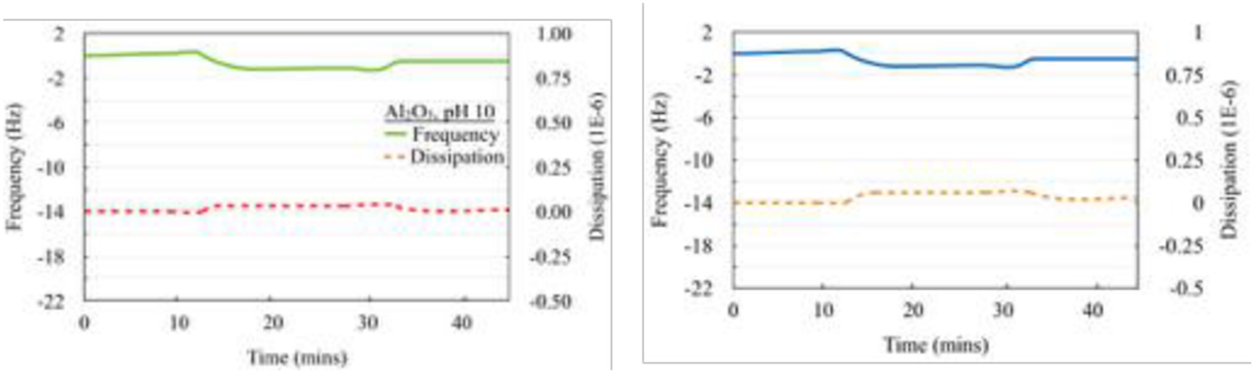

Figure 4.S6. Adsorption tests of BSA-SH MBs on alumina sensor at pH 10 (a) and silica sensor at pH 6 (b).

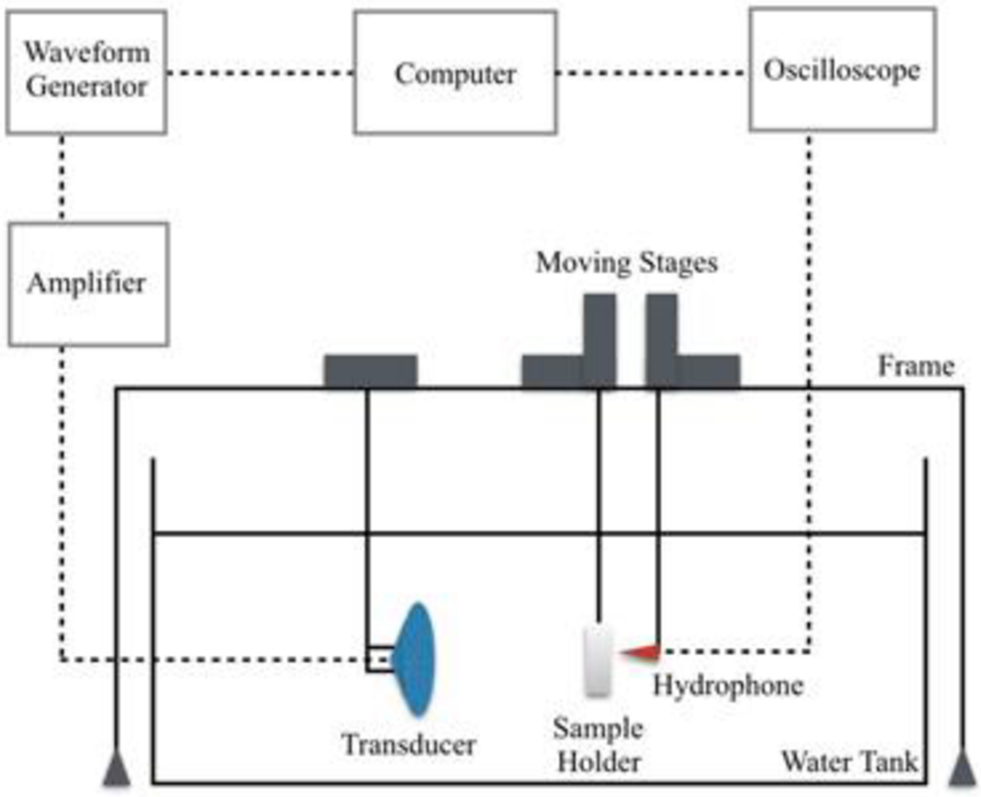

Figure 4.S7 Schematic of the experimental setup used to characterize the microbubble acoustic attenuation

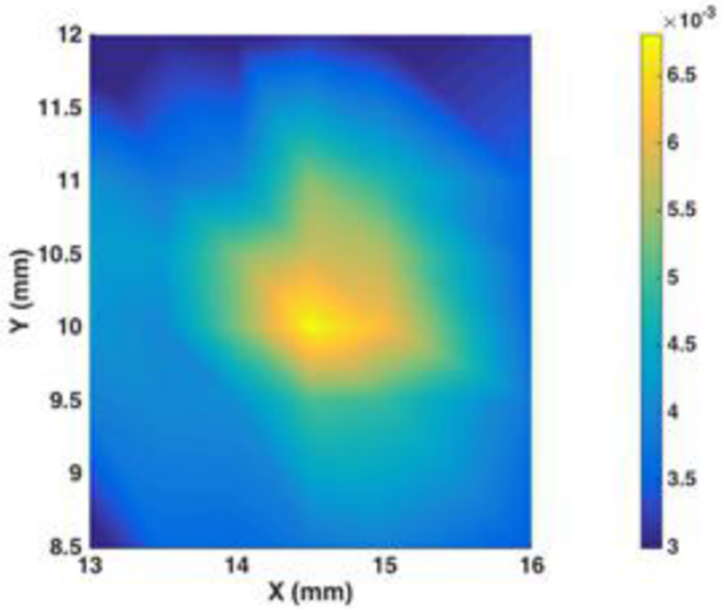

Figure 4.S8 Map of the maximum signal received (colour bar in V) in the plan transverse to the acoustic propagation

Figure S7 shows a schematic of the experimental setup used for the acoustic attenuation measurement. A 3.3 MHz center frequency High Intensity Focused Ultrasound transducer (Sonic Concepts H-101) was used as an emitter and a broadband hydrophone (ONDA HNR 0500) was used as a receiver. The HIFU was excited by an arbitrary waveform generator (SIGLENT 1010) and amplified by an RF amplifier (E&I 1020L). The pulse emitted was 20 cycles long and the pulse repetition period was 10 ms. The hydrophone was connected to an oscilloscope (RIGOL 1104Z-S) and mounted on three-axis micro-positioner for the purpose of alignment. To ensure efficient noise reduction, the acoustic measurements were averaged over 64 waveforms. The tested solution was introduced into a plastic container (1 cm x 1 cm x 4 cm) with 2 rectangular holes on both sides covered with a stretched latex membrane creating two acoustic windows. The cell was precisely placed at the HIFU focal point using a three-axis micro-positioner and the

hydrophone was inserted right behind the cell (Figure S7). All experiments have been performed in a fish tank filled with water.

In order to isolate the effect of microbubbles on the attenuation, we compared the acoustic measurements of the protein solution (in which microbubble are generated) before and after the sonication. Previous to the experiment the acoustic field was scanned in the transverse plan (parallel to the cell) to align the hydrophone with the center of the acoustic beam. As shown by the Figure S8, the acoustic energy is concentrated into a small area due to the transducer geometry. The attenuation coefficient was then calculated based on the amplitude of the signal from the protein and microbubble solution at the maximum of amplitude (X=14.5 mm and Y=10 mm in Figure S8) using:

$$\alpha_{att} = \frac{20 \log_{10}\left(\frac{V_{protein}}{V_{microbubble}}\right)}{D}$$

where D is the cell width and is equal to 1 cm.

The attenuation coefficient was found to be 0.53 dB/cm with a standard deviation of 0.1 dB/cm. This value is in the order of magnitude of classical contrast agent studies [71, 72] suggesting that these new microbubbles could be used as a contrast agent.

Chapter 5 Preparation of poly(N-isopropylacrylamide)-block-(acrylic acid)-encapsulated proteinaceous microbubbles for delivery of doxorubicin[2]

5.1 Introduction

For biomedical or biopharmaceutical applications, gas-filled microbubbles (MBs), with a typical size range of 1 to 10 μm [1, 2], are frequently stabilized by a structured shell to overcome the Laplace pressure, originated from the curved surface [3,4]. Depending on the requirements of shell stiffness and functionality, the shell can be synthesized from a range of biocompatible molecules, such as proteins, lipids, or polymers.[5] Comparatively, a proteinaceous shell tends to have a higher degree of stiffness after the treatment of protein denaturation prior to the synthesis of MBs, and a lipid or polymer shell is often utilized as a functional template for ligand binding [6, 7]. Different gasses including air, perfluorocarbons, and sulfur hexafluoride have been used as a gas core inside the shell, the last two of which are considered to comparably improve the microbubble stability due to their lower partial pressure and blood solubility [8]. With a compressible gas core, MBs have the high echogenic responsiveness and are primarily used as ultrasound contrast agent in the medical field [1, 2, 9]. MBs decorated with radionuclides, fluorescent agents, or nanoparticles have also been extensively studied for multimodal imaging [10-12].

Theranostic refers to the coupling of the diagnostic with the therapeutic approaches, and MBs have been proposed for their possibilities of being utilized for theranostic applications [8, 13,

[2] A version of this chapter was accepted for publication on *Colloids and Surfaces B: Biointerfaces*.

14]. In addition to their contrast-enhancing role at the initial diagnostic stage, MBs can release their carried payloads either simultaneously or subsequently at the therapeutic stage. The payloads can be incorporated into the shell during the synthesis of MBs or onto the shell using cross-linkers after the synthesis of MBs [15-17]. The release of their payloads can be triggered by various stimuli, such as ultrasound, light, pH, and temperature [18]. Upon exposing to these stimuli, the carried drug can be site-specifically discharged in a controllable way and locally accumulated for a period of time [18]. Leong-Poi *et al.* intravenously delivered vascular endothelial growth factor-165 ($VEGF_{165}$) plasmid DNA- bearing MBs to enhance the expression of $VEGF_{165}$ in rats and consequently to induce arteriogenesis to treat ischemic skeletal muscles [19]. Ting *et al.* demonstrated that the use of 1,3-bis(2-chloroethyl)-1- nitrosourea (BCNU)-carried MBs effectively caused the disruption of the blood-brain barrier (BBB) and simultaneously dispense BCNU upon the application of focused ultrasound (FUS) [20].

Doxorubicin (Dox), a family of anthracyclines, has been prevalently used in chemotherapy today for its effectiveness of suppressing most of the cancer cells [21, 22]. Dox has been reported to intercalate with DNA and to prevent its transcription [23, 24]. At the intercalation sites, the progression of an enzyme topoisomer, one of the key enzymes associated with the DNA transcription process, can be terminated. As a result, the biosynthesis of macromolecules can be largely inhibited [24, 25]. Several key issues have been reported to be associated with the administration of free Dox into the bloodstream, such as the destruction of healthy tissue cells and low accumulation of Dox at the targeted tumor site [26-28]. These disadvantages require the development of a carrier to site-specifically deliver Dox instead of intravenously injecting the free form of Dox [29-31]. With a carrier, the exposure of free Dox to healthy tissue cells could be substantially minimized, and ideally, the release could be specifically targeted, resulting in a

transiently high local accumulation of Dox [31, 32].

The payload drugs can be loaded onto a carrier either through electrostatic interaction or bond formation; however, a protective outer shell is particularly needed for the electrostatic loadings of drugs to prevent any premature release [33-35]. Although the payloads can be dramatically increased through layer-by-layer approach [36, 37], the exposed payloads can significantly interact with the vesicular environment. As the electrostatic interaction is typically non-specific, the negatively charged cells can interact with the positively charged payload-bearing MBs, resulting in an early release of the payload, formation of oversized aggregates, and potential hazard of blocking the vasculature [38]. To overcome the drawbacks of non-specific, premature release of the payload, a protective outer shell would be needed to greatly reduce the exposure of the payload to the blood components. Poly(N-isopropylacrylamide-block-acrylic acid) (poly(NIPAM-b-AAc)) copolymerized from the monomers of N-isopropylacrylamide (NIPAM) and acrylic acids (AAc) have already been considered as a suitable candidate for drug delivery for its multiple responsive properties [39, 40]. Upon increasing the temperature, decreasing the pH value, or increasing the salt concentration to a critical threshold, poly(NIPAM-b-AAc) shrinks and coils up, squeezing out the encapsulated payload.[41] The incorporation of AAc into the polymer increases its lower critical solution temperature (LCST), and its content could be manipulated to reach a biologically relevant LCST [42-44].

In this work, a chemotherapeutic agent, Dox, was loaded onto proteinaceous MBs electrostatically, and the Dox-loaded MBs were further encapsulated by a temperature-sensitive poly(NIPAM-b-AAc) shell. By incorporating 4 mol% AAc, the synthesized poly(NIPAM-b-

AAc) was fine-tuned to alter its LCST slightly above the body temperature, 39 °C, and later used as a temperature-responsive shell which lowers the propensity of premature release. The successive loadings of Dox and poly(NIPAM-b-AAc) on MBs were confirmed by different characterization techniques, such as scanning electron microscope (SEM) imaging, fluorescent confocal laser scanning microscope (CLSM) imaging, zeta potential measurement, Fourier transform infrared spectroscopy (FTIR), and quartz crystal microbalance with dissipation (QCM-D). Based on the in-vitro release testing (IVRT), compared with the bare MBs, the poly(NIPAM-b-AAc)-shelled MBs exclusively showed an excellent retention of the loaded Dox at room temperature and a temperature-sensitive release of Dox upon elevating the temperature from 37 °C to 39 °C.

5.2 Materials and Methods

Lyophilized BSA, Traut's reagent, doxorubicin hydrochloride (Dox), N-Isopropylacrylamide (NIPAM), acrylic acid (AAc), 2,2′-Azobis(2-methylpropionitrile) (AIBN), and 2-Aminoethanethiol hydrochloride were purchased from Sigma Aldrich. Dialysis tubing, spin desalting columns, and phosphate buffered saline (PBS) were obtained from ThermoFisher Scientific. Methanol and ethyl ether were acquired from Fisher Scientific. 2-Aminoethanethiol hydrochloride was purchased from Acros Organic. All chemicals were of analytical grade and used as received without further purification unless specified. Milli-Q water with a resistivity of 18.2 MΩ•cm was used to prepare all the stock solutions.

5.2.1 Synthesis of MBs

The synthesis of protein-stabilized MBs used for our experiment was extensively described in our previous study [45]. In brief, BSA (50 mg) and Traut's reagent (2 mg) were mixed in 1 ml of PBS and incubated at 23 °C for 1 hr before removing the excess Traut's reagent using either a desalting column or a dialysis bag. Following a brief heat shock at 45 °C, an ultrasonic tip (3 mm) of a dismembrator (Fisher ScientificTM Model 705) was placed at the air-solution interface to generate an impulse (173 W, 20 kHz) for 45 sec. The synthesized MBs were purified through either gentle centrifugation[46] or column flotation [47].

5.2.2 Synthesis of Poly(NIPAM-b-AAc)

Poly(NIPAM-b-AAc) were synthesized using free radical polymerization described as following. NIPAM (80 mmol), AAc (3.2 mmol), AIBN (1 mmol), and AET (1 mmol) were added to a round-bottom flask containing 40 ml of methanol, followed by a nitrogen purge for 30 mins. The copolymerization was allowed to proceed at 60 °C for 16 hrs. The copolymerized polymer was purified from the unreacted reagents through selective precipitation. In specific, upon introducing the reaction mixture into diethyl ether drop-wisely, the polymer was precipitated out while the unreacted monomers and other reagents were dissolved. Following the filtration, the precipitated polymer was re-dissolved in methanol and taken for precipitation in diethyl ether to repeat in triplicates. Further purification of the synthesized poly(NIPAM-b-AAc) was achieved through dialysis using a dialysis tube against Mili-Q water for five days before freeze drying (Labconco FreeZone 4.5) for storage.

5.2.3 Successive loadings of Dox and poly(NIPAM-b-AAc) onto MBs

MBs (30 mg/ml) were used to react with Dox (10 μg/ml) in a 2 ml solution of PBS at 35 °C for 2 hrs. Following the reaction, the Dox-loaded MBs were separated from the unreacted Dox through the column flotation at room temperature. In detail, the reacted mixture was slowly injected from a long-tipped pipet at the bottom of a column, and the Dox-loaded MBs were effectively separately from the unreacted Dox because the flotation speed of MBs towards to the top of the column was much faster than the diffusion speed of the free Dox. With this step repeated three times, the Dox-loaded MBs were introduced to react with excessive poly(NIPAM-b-AAc) (50 mg/ml) for 2 hrs to assemble a polymer outer shell. The poly(NIPAM-b-AAc) shelled, Dox-encapsulated MBs were then purified through the column flotation for three times as mentioned before and subsequently stored at 4 °C for both the releasing and characterization tests.

5.2.3 SEM and CLSM imaging analysis

To access the surface morphology, SEM images were taken using a field emission scanning electron microscope (FESEM: Carl-Zeiss Sigma) at an operating acceleration voltage of 5 kV. A single drop of the solution containing the freshly-prepared MBs with various loadings was dipped onto a silicon wafer and left to evaporate. A carbon coating was used to cover the dried silicon wafer before the measurements for better conductivity. With an intrinsic fluorescent emission at 575 ± 20 nm when excited at 490 nm due to the three planar and aromatic hydroxyanthraquinonic rings, confocal microscope images were collected to confirm the loading

of Dox onto MB using a CLSM (Quorum Wave FX-Spinning Disk) equipped with a multi-modal imaging (MMI) optical tweezer. A small aliquot of Dox-loaded MBs was dropped onto a glass slide and left to dry in the dark overnight. The 100×, oil immersion lens was used for collecting the images.

5.2.4 Hydrodynamic size, zeta potential, and FTIR measurements

The hydrodynamic sizes of the synthesized poly(NIPAM-b-AAc) were determined through dynamic light scattering (DLS) measurement using an ALV/CGS-3 compact goniometer system. The solution of poly(NIPAM-b-AAc) was diluted and put into a test tube for temperature stabilization before data collection. Zeta potential measurements of MBs, Dox-loaded MBs, and Dox-loaded MBs with an outer shell of poly(NIPAM-b-AAc) were performed using a ZetaPALS analyzer (Brookhaven Instrument, USA). Except for the Dox used as purchased, MBs, Dox-loaded MBs, poly(NIPAM-b-AAc), and poly(NIPAM-b-AAc)-shelled, Dox-loaded MBs were lyophilized using a freeze dryer (Labconco FreeZone 4.5) and taken for FTIR absorbance measurements. The measured spectra were recorded with 32 scans at a resolution of 1 cm^{-1} using a Nicolet iS50 FT-IR spectrometer equipped with an iS50 automated beamsplitter exchange (ABX) from 700 to 4000 cm^{-1}.

5.2.5 QCM-D measurements

Using a D300 QCM-D (Q-Sense Västra Frölunda, Sweden) with a QAFC 302 axial flow measurement chamber, QCM-D measurements were conducted to both confirm the loadings and

surface charges through interactions with SiO_2 and Al_2O_3 sensors (QSX303, Q-Sense AB) at pH 7. The fundamental resonant frequency of all sensors was excited at ~ 4.9 MHz before injecting any solutions. The flow rate to the chamber was maintained at 25 μL/min using a flow dispenser (ISM935C, ISMATEC). With a constantly controlled temperature at 23 °C, the background solution of PBS was injected into the chamber to flow for approximately 10 mins, followed by the injection of the solutions. After stabilizing at the equilibrium for a certain period of time, the background solution of PBS was injected to wash away any accidental attachment or loosely-bound MBs or molecules for another 10 - 15 min.

5.2.6 IVRT of Dox-loaded MBs and Dox-loaded MBs with a poly(NIPAM-b-AAc) shell

Dox-loaded MBs and Dox-loaded MBs with an outer poly(NIPAM-b-AAc) shell were respectively immersed into a dialysis tube containing 5 ml of PBS, and the tube was placed into a 50 ml PBS environment with a constant stirring at different temperatures for up to 40 h. 1 ml of the solution from the dialysate outside the tube was withdrawn at 1 hr interval and replaced with fresh PBS to maintain the sink condition. The released Dox was subsequently quantified with a fluorescence spectrophotometer (Cary Eclipse FLR) by measuring the fluorescence intensity at 575 ± 20 nm when excited at 490 nm.

5.3 Results and discussion

5.3.1 Loading of Dox onto MBs

With a slightly basic pKa value of 8.3 [48, 49], Dox was positively charged at pH 7 because of its amine moiety; in the meantime, the bare MBs (pKa = 4.5) were negatively charged, as

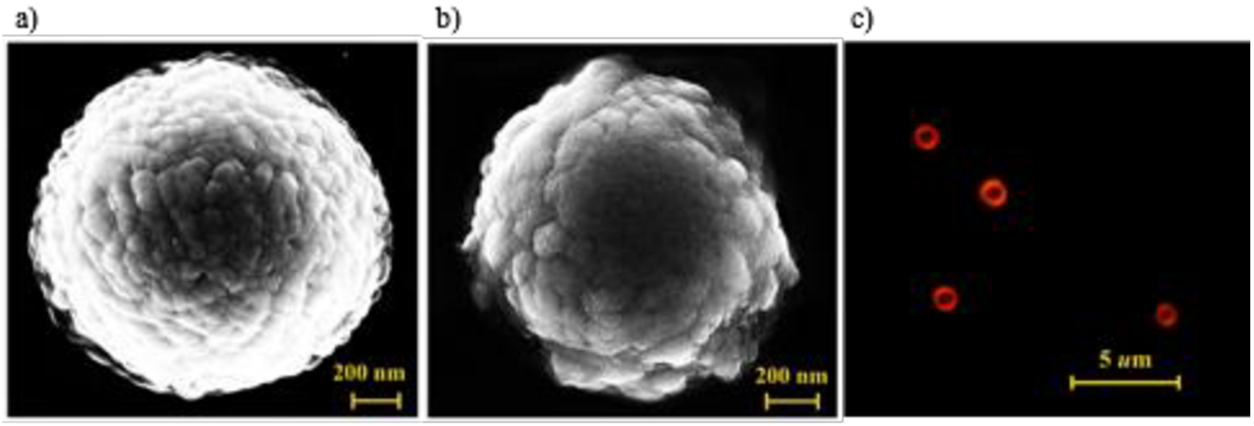

Figure 5.1 SEM micrographs of the bare MBs (a) and Dox-loaded MBs (b) and a fluorescent CLSM micrograph of the Dox-loaded MBs.

reported in our previous study [45]. The electrostatic opposition created a favorable condition for the loading of Dox onto MBs, and the successful loading of Dox was demonstrated using SEM, fluorescent CLSM, QCMD, zeta potential measurement, and FTIR measurement. On the surface morphological aspect, a smoother surface was observed after the loading of Dox; in other words, the initial bumpy surface of the bare MBs became less pronounced after the loading of Dox (Figure 5.1a, b). The appearance of red-circled MBs was another evidence of the successful loading due to the intrinsic fluorescence of the loaded Dox upon excitation at 490 nm (Figure 5.1c). A fairly evenly allocated, thick fluorescent layer also revealed that the surface loading of Dox on MBs was well distributed and in appreciable quantity (Figure 5.1c).

QCM-D was also adopted to confirm the occurrence of the loading of Dox (Figure 5.2a, b). As the Sauerbrey equation states, a drop in the frequency of a piezoelectric crystal indicates the

attachment or adsorption of the incoming molecules or particles onto the crystal surface [50]. MBs were initially anchored onto an Al_2O_3 surface (Figure 5.2b (II)) at pH 6 by virtue of the electrostatic interaction, shown by a drop followed by a plateau from 10 to 50 mins (Figure 2a

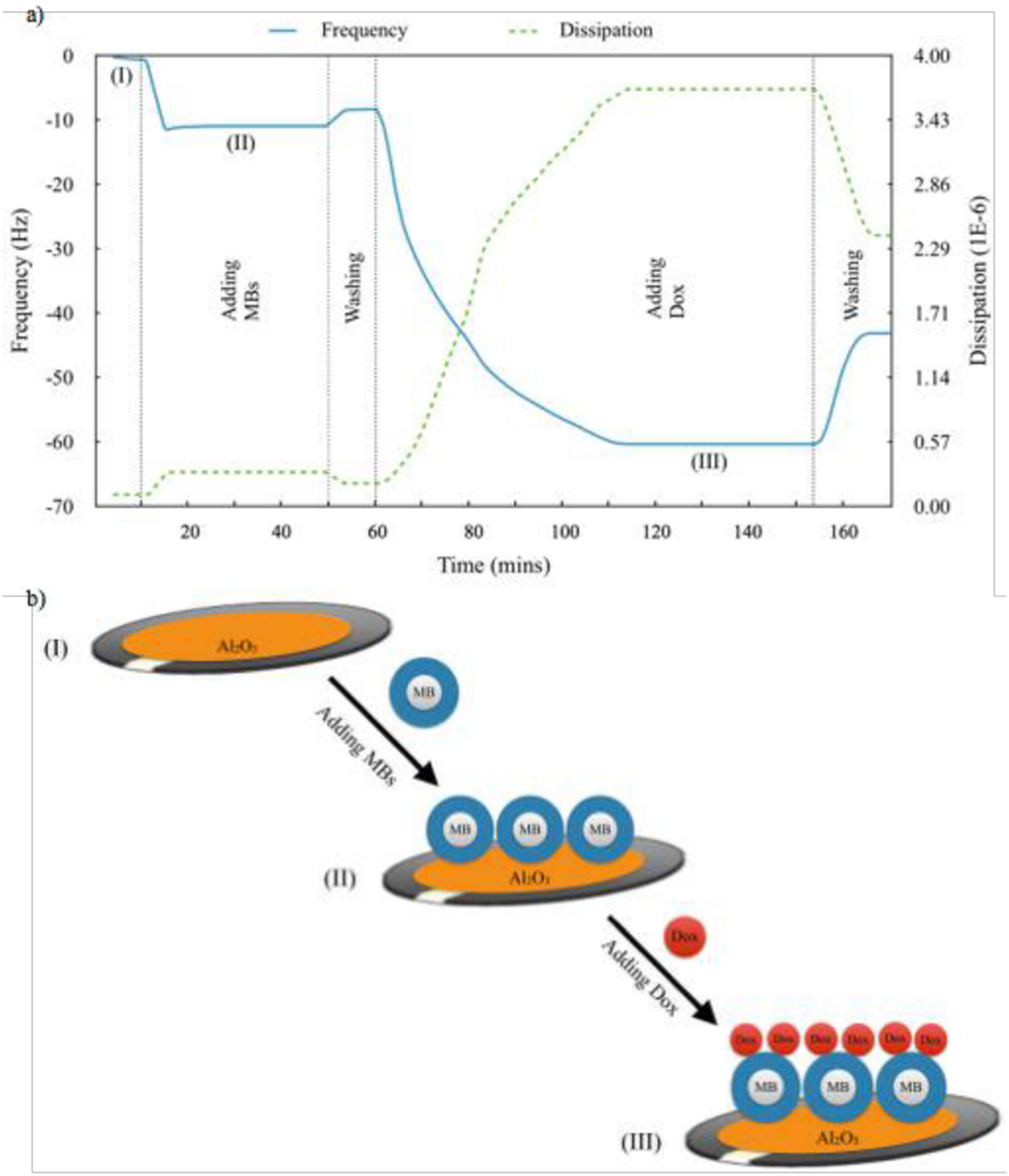

Figure 5.2 QCM-D analysis (a) and schematic (b) showing the deposition of MBs (II) on a Al_2O_3 (II)). After reaching the equilibrium, the background solution of PBS was used to wash the sensor (I) and the subsequent loading of Dox (III) on the deposited MBs (II).

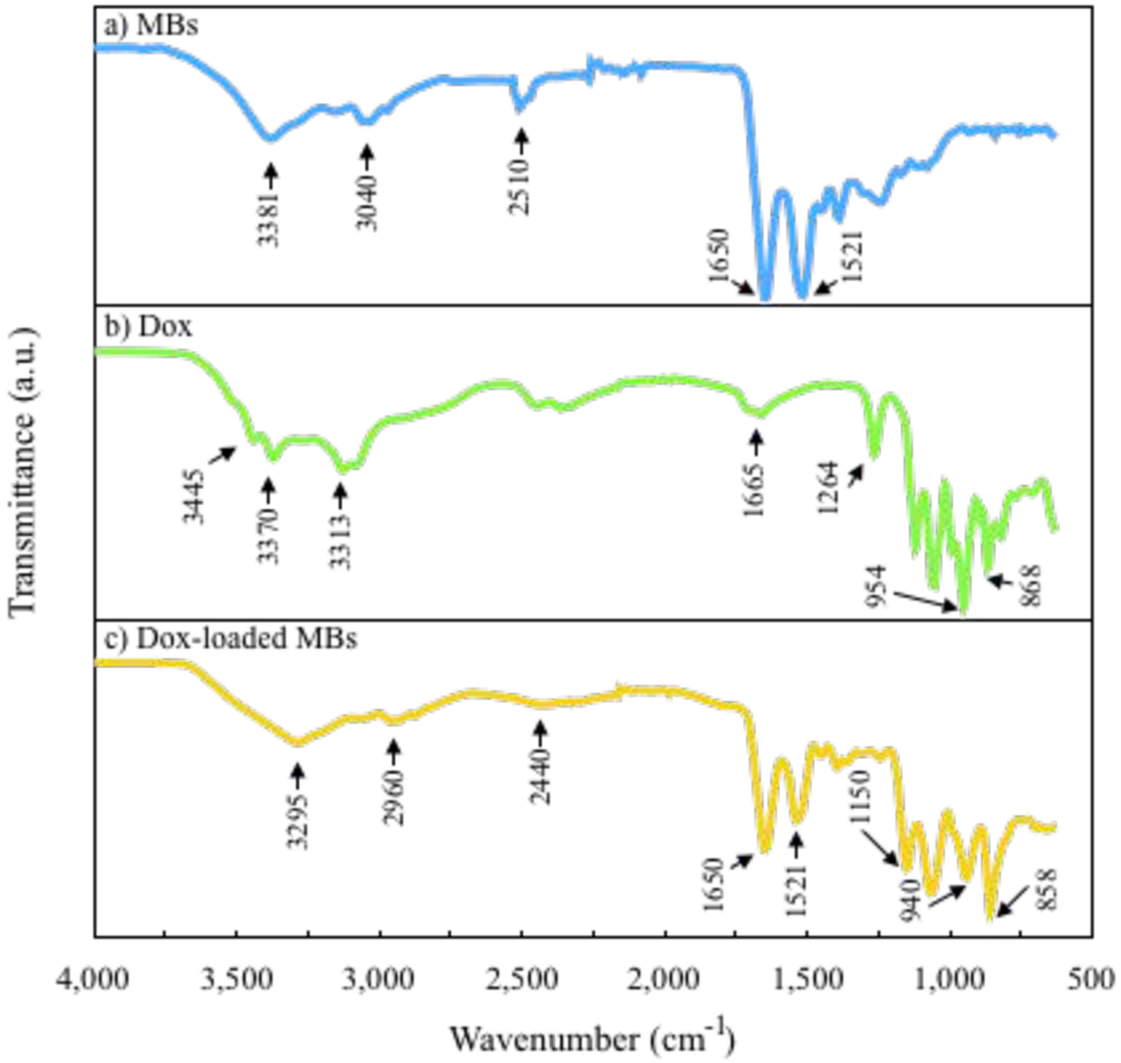

Figure 5.3 FTIR spectra of the bare MBs (a), Dox (b), and Dox-loaded MBs (c).

sensor to remove the loosely bound MBs, resulting in a slight increment of the frequency. Dox was subsequently introduced into the MBs-deposited Al_2O_3 surface (Figure 5.2b (III)), exhibiting

another drop and approaching to the second plateau at 60 - 150 mins (Figure 5.2a (III)). Compared to the quick deposition of MBs to the Al_2O_3 surface, a much longer time (approximately 50 mins) was taken to fully load Dox on MBs. Followed by a similar washing step, a much greater amplitude of drop in frequency was detected after the loading of Dox (~30 Hz) (Figure 5.2a (II), (III)) than after the initial anchoring of MBs (~10 Hz) (Figure 5.2a (I), (II)), indicating a much heavier loading of Dox compared to the initially anchored MBs. As a cross-check, Dox-loaded MBs were synthesized externally and directly injected into the QCM-D chamber, interacting with a positively-charged Al_2O_3 and a negatively-charged Si_2O surface at pH 7 (Figure 5.S1a, c). It was shown that successful attachment only occurred between the positively-charged, Dox-loaded MBs and the Si_2O surface (Figure 5.S1a). Upon interaction with the Al_2O_3 surface, unspecific adsorption of Dox-loaded MBs was observed, and they were nearly completely washed away because of the electrostatic repulsion (Figure 5.S1c). The reversal of the zeta potential from -23.0 ± 3.0 to 30.0 ± 5.1 mV was another direct evidence of the successful loading Dox onto MBs through the zeta potential measurement.

FTIR spectra of MBs, Dox, and Dox-loaded MBs were also collected in order to investigate the interaction between Dox and MBs (Figure 5.3). The successful loading of Dox (Figure 5.3b) onto MBs (Figure 5.3a) was demonstrated by the appearance of the functional groups of Dox on Dox-loaded MBs (Figure 5.3c); specifically, the C-O-C stretching of ethers and the N-H wagging of amines on Dox at 1150, 954 and 868 cm^{-1} (Figure 5.3c) appeared after the loading of Dox in comparison with the bare MBs (Figure 5.3a) [51, 52]. The downward shift of the O-H stretching of carboxylic acids of MBs from at 3040 (Figure 5.3a) to 2960 cm^{-1} (Figure 5.3c) suggested an electrostatic interaction with the amine group of Dox which was also accompanied

with similar downward shifts of the N-H wagging from 954 and 868 (Figure 5.3b) to 940 and 855 cm^{-1} (Figure 5.3c), respectively [53, 54]. The downward shifts and broadenings of the S-H stretching of thiols from 3381 (Figure 5.3a) to 3295 cm^{-1} (Figure 5.3c) and the O-H stretching of alcohols from 2510 (Figure 5.3a) to 2440 cm^{-1} (Figure 5.3c) revealed their significant involvement of hydrogen bonding facilitating the loading of Dox.

5.3.2 Coating of poly(NIPAM-b-AAc) on Dox-loaded MBs

The temperature-sensitive polymer, poly(NIPAM-b-AAc) was specifically designed to have an LCST of 39 °C (Figure 5.4a, b), slightly higher than the body temperature, 37 °C, by incorporating 4 mol% AAc. At the interval from 38 to 39 °C, poly(NIPAM-b-AAc) underwent a major conformational change, and its hydrodynamic size greatly reduced from ~300 to ~200 nm (Figure 5.4a). Such a conformational change was, in the meantime, accompanied by an increased turbidity experimentally measured by the UV/Vis absorbance at 350 nm (Figure 5.4b). With a pre-tuned LCST of 39 °C, an outer shell of poly(NIPAM-b-AAc) acted as a temperature-responsive cage, switching on above its LCST and off below its LCST.

The coating of poly(NIPAM-b-AAc) onto the Dox-loaded MBs primarily relied on their opposite charges. Due to the inclusion of AAc, poly(NIPAM-b-AAc) was negatively charged at pH 7 and therefore attractive to the positively-charged Dox-loaded MBs. The successive loadings of Dox on MBs and poly(NIPAM-b-AAc) on Dox-loaded MBs were analogous to the layer-by-layer (LbL) assembly technique reported in the literature [36, 55, 56]. As a reliable tool for monitoring the LbL buildup [57, 58], QCM-D measurement was adopted and continued from the previous

one (Figure 5.2). Starting at 170 mins (Figure 5.5a), poly(NIPAM-b-AAc) was injected into the QCM-D chamber to shell the Dox-loaded MBs (Figure 5.5b). A drop was

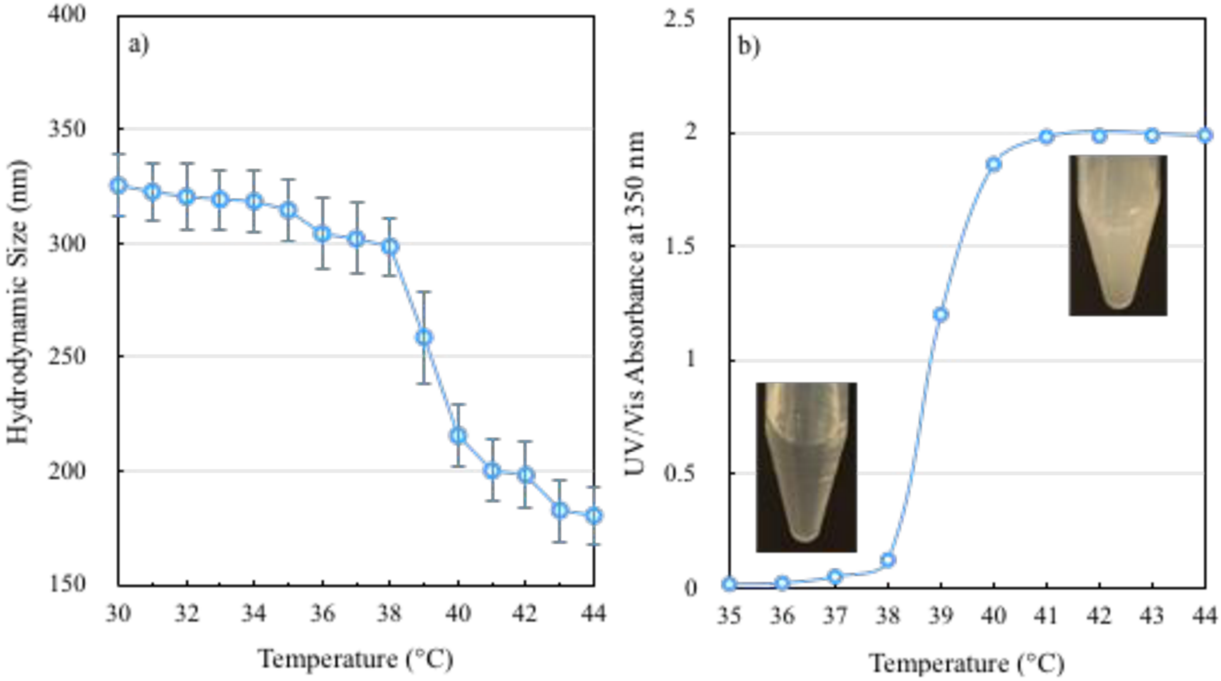

Figure 5.4 The temperature-dependence of the hydrodynamic size (nm) (a) and UV/Vis absorbance at 350 nm (b) of the synthesized poly(NIPAM-b-AAc). The inlet images (b) were the snapshots of poly(NIPAM-b-AAc) before (left) and after the heating (right).

immediately observed and followed by a plateau from ~175 to ~220 mins (Figure 5.5a (IV)), confirming the successful coating of the polymer layer. After the washing step to remove any physically attached or loosely bound polymers, the equilibrium was reached again after ~225 mins (Figure 5.5a). The stepped drops for three consecutive times (Figure 5.2a (II), (III), Figure 5.5a (IV)) was a strong evidence of the successive loadings of each oppositely-charged layer (Figure 5.2b (II), (III), Figure 5.5b (IV). As a similar cross-check, the Dox-loaded MBs with a coated shell of poly(NIPAM-b-AAc) were introduced to react with Al_2O_3 (Figure 5.S1b) and

Si_2O (Figure 5.S1d) surfaces at pH 7. As expected, the negatively-charged, polymer-shelled, and

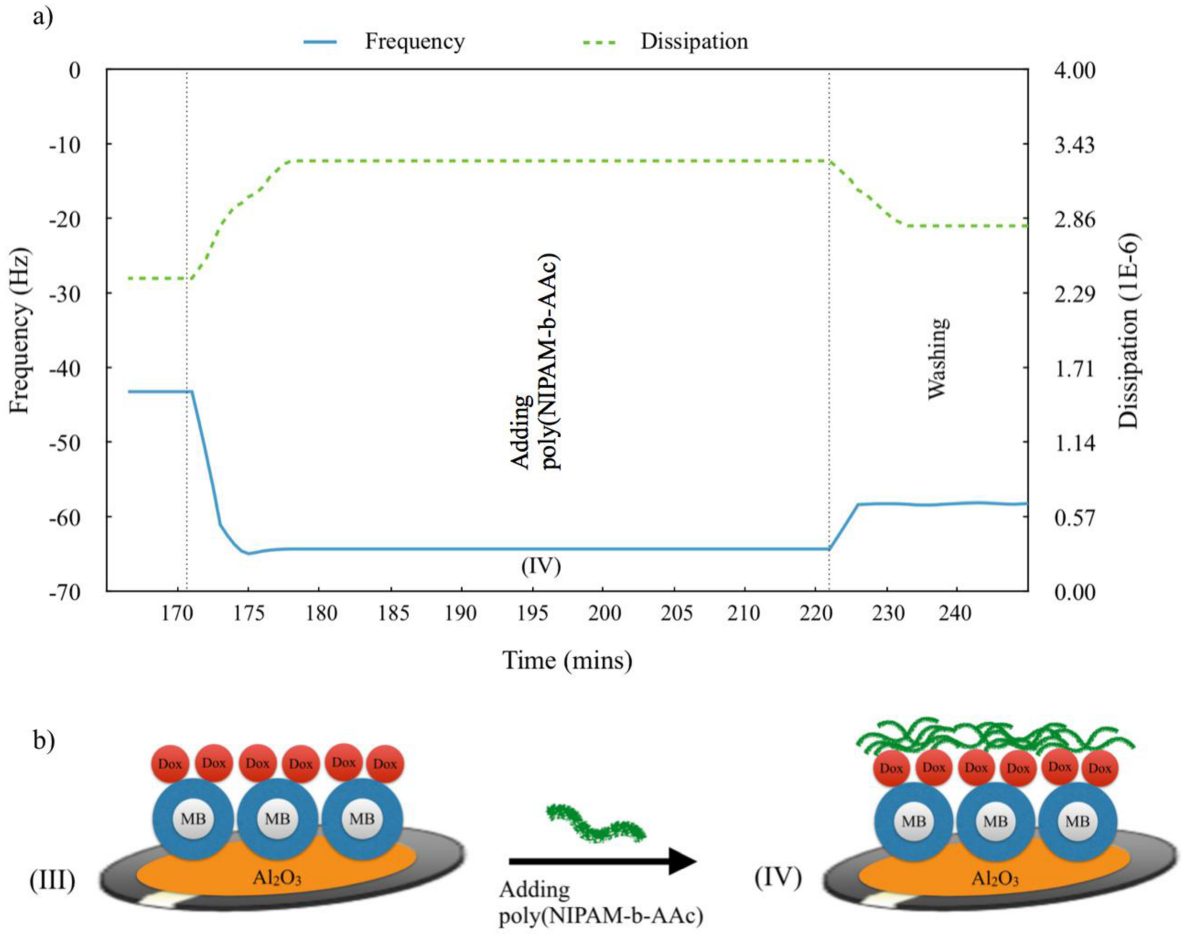

Figure 5.5 QCM-D analysis (a) and schematic (b) showing the encapsulation of poly(NIPAM-b-AAc) (IV) on Dox-loaded MBs (III).

Morphologically, an even smoother surface was observed after the coating of poly(NIPAM-b-AAc) through SEM (Figure 5.6); collectively, a smoothening trend was observed from the bare MBs (Figure 5.1a) to the Dox-loaded MBs (Figure 5.1b) and from the Dox-loaded MBs (Figure 5.1b) to polymer-shelled, Dox-loaded MBs (Figure 5.6). The disappearance of the fluorescent MBs under CLSM was another indication of the successful formation of the outer polymer shell. Dox-loaded MBs only attached to the positively-charged Al_2O_3 (Figure 5.S1b) but not on Si_2O

(Figure 5.S1d) surfaces, represented by a sharp decrease and an insignificant change in frequency, respectively.

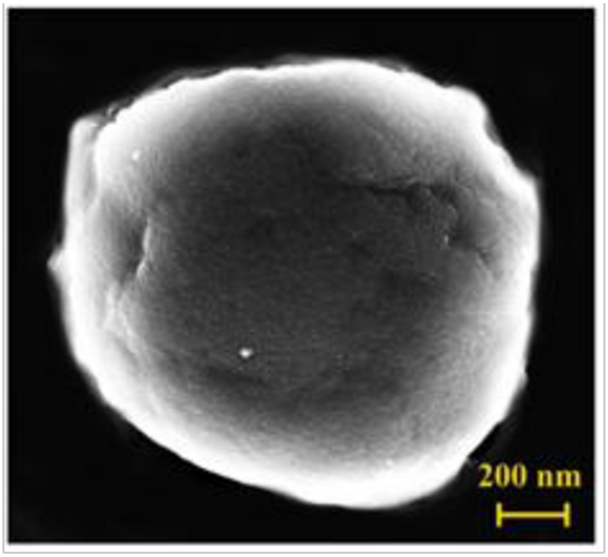

Figure 5.6. An SEM micrograph of Dox-loaded MBs with a poly(NIPAM-b-AAc) shell.

only appeared after the loading of Dox due to the intrinsic fluorescence of Dox (Figure 5.1c); in other words, the bare MBs and the Dox-loaded MBs with an outer shell of polymer did not show any CLSM images due to the lack of fluorescence. Based on the zeta potential measurement, another zeta reversal from 30.0 ± 5.1 to -40.0 ± 4.5 mV was exhibited after the encapsulation of Dox-loaded MBs with a poly(NIPAM-b-AAc) shell, indicative of its successful coating through the electrostatic interaction. poly(NIPAM-b-AAc) (b).

The identity of poly(NIPAM-b-AAc) was confirmed through its characteristic peaks of the O-H stretching of carboxylic acids at 3430 cm^{-1}, N-H stretching at 3310 cm^{-1}, C-H stretching at 2970

cm^{-1}, C-C stretching at 2805-3000 cm^{-1}, amide I (C=O stretching) at 1615 cm^{-1}, amide II (N-H and C-N stretching) at 1549 cm^{-1}, and C-C bending at 1350-1470 cm^{-1} (Figure 7a) [41, 59]. The

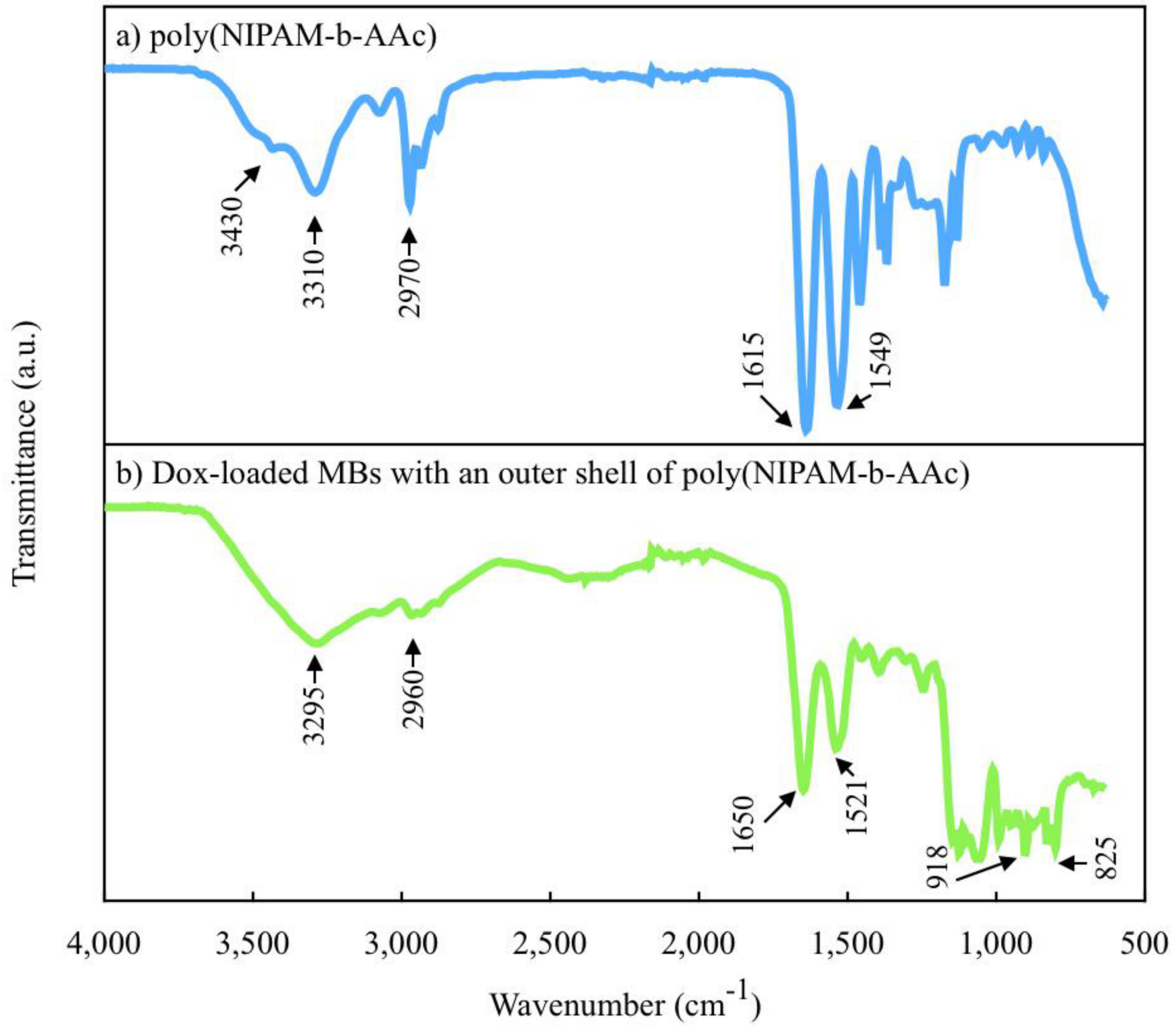

Figure 5.7 FTIR spectra of poly(NIPAM-b-AAc) (a) and Dox-loaded MBs with a shell of The fluorescent MBs

absence of C=C stretching further showed the exclusive presence of poly(NIPAM-b-AAc) without any existence of the starting monomers, NIPAM and AAc, respectively (Figure 5.7a) [41]. The shell formation of poly(NIPAM-b-AAc) on the Dox-loaded MBs through an

electrostatic interaction was confirmed by the blue-shift and the broadening of the N-H wagging of the Dox-loaded MBs from 940 and 855 cm^{-1} (Figure 5.3c) to 918 and 825 cm^{-1} (Figure 5.7b) and by the overlapped, broadened peak of the O-H stretching of carboxylic acids of the polymer from 3430 (Figure 5.7a) to 2960 cm^{-1} (Figure 5.7b).

5.3.3 IVRT of Dox from Dox-loaded MBs and Dox-loaded MBs with a poly(NIPAM-b-AAc) shell

A poly(NIPAM-b-AAc) shell was implemented in an effort to hinder any premature release,[34] and its critical role was demonstrated through comparing the releasing profiles of Dox from Dox-loaded MBs (Figure 5.8a) and Dox-loaded MBs with the polymer shell (Figure 5.8b). At a relatively low concentration of free Dox (0.1-1 μg/ml), a linear relationship with its fluorescent emission was experimentally observed (Figure 5.S2a). However, at a higher concentration of Dox (above 1 μg/ml), such a relationship (Figure 5.S2b, c) became non-linear and might be from the self-quenching mechanism of Dox [60, 61]. By measuring the concentration of the free Dox in the releasing medium, the releasing profiles of polymer-shelled and shell-free carriers were compared as following. With a polymer shell encapsulating the Dox-loaded MBs, no appreciable amount of Dox was detected at room temperature (23 °C) in the releasing media, confirming the retention of the loaded Dox over time (Figure 5.8b). On the contrary, the capability of retaining Dox from the shell-free MBs at 23 °C was much poorer, releasing nearly 75%, within 8 hrs (Figure 5.8a). In addition to the poor retention of Dox from these shell-free carriers, a quick release burst of over 50% of the loaded Dox was detected within 1 hr in the releasing media, emphasizing the needs of a protective outer shell (Figure 5.8a).

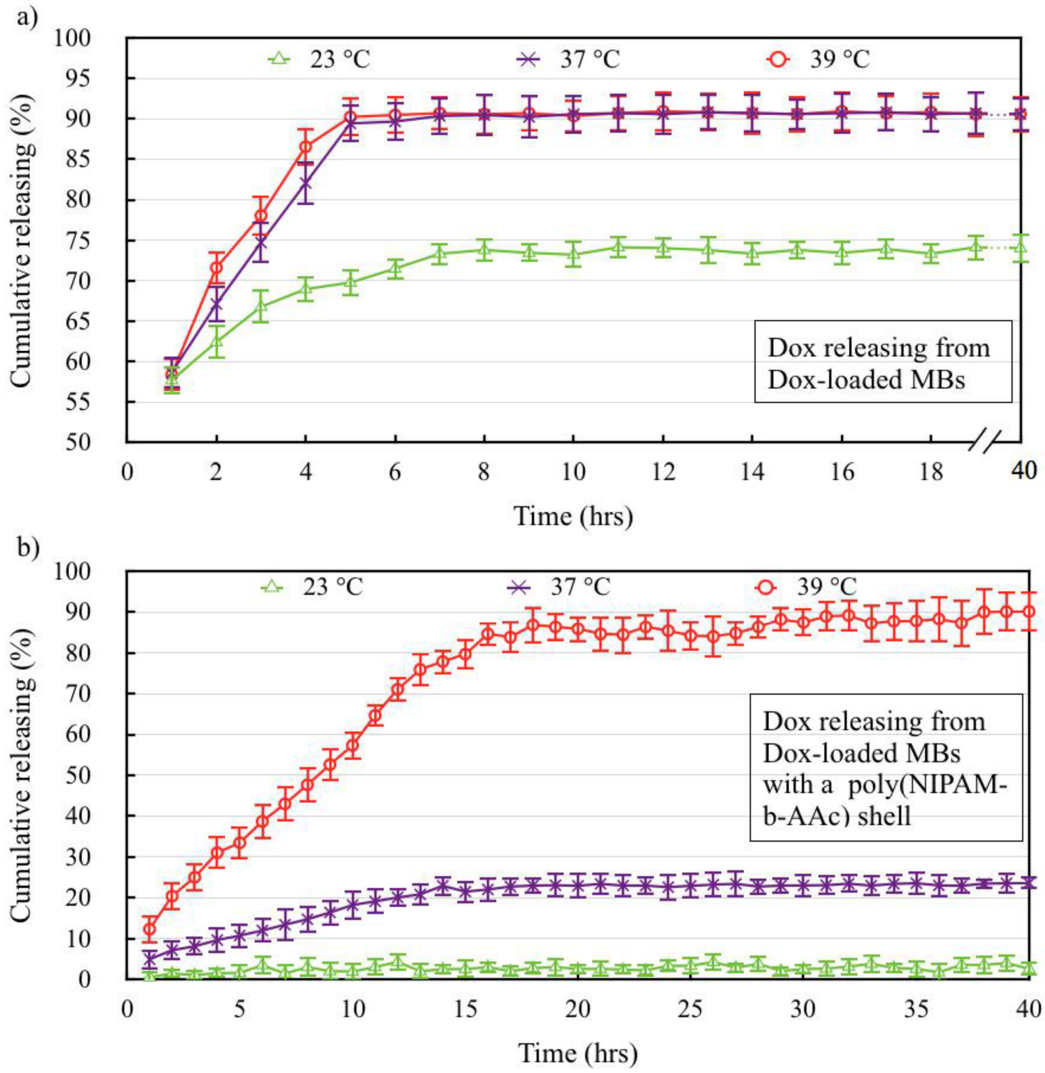

Figure 5.8 Dox releasing profiles from Dox-loaded MBs (a) and Dox-loaded MBs with a poly(NIPAM-b-AAc) shell (b).

At shown in Figure 8b, only a minor portion of the Dox (~20%) was released at the body temperature, 37 °C. In contrast, the most of the loaded Dox (~90%) was discharged into the media at 39 °C. Such a substantial difference upon heating from 37 °C to 39 °C was not observable when shell-free MBs were used (Figure 5.8a). It was also worth mentioning that the

release of Dox from the poly(NIPAM-b-AAc)-shelled MBs at 39 °C was significantly slower than that from shell-free MBs. Specifically, the time used to discharge 90% of the loaded Dox from the polymer-shelled MBs was approximately 18 hrs (Figure 5.8b) in comparison with the ~5 hrs (Figure 5.8a) consumed by the shell-free carriers. The temperature-responsive switch and the gradually-released profile collectively demonstrate the suitability of utilizing poly(NIPAM-b-AAc)-encapsulated, Dox-loaded MBs as a drug carrier.

5.4 Conclusions

A representative chemotherapeutic agent, Dox was electrostatically loaded onto the previously studied protein-stabilized MBs, and a temperature-responsive outer shell of poly(NIPAM-b-AAc) was used to encapsulate the Dox-loaded MBs. Successive loadings of Dox and poly(NIPAM-b-AAc) were confirmed using techniques such as QCM-D, zeta potential measurement, SEM, fluorescent CLSM, and FTIR. Compared to the Dox release from the shell-free MBs, the poly(NIPAM-b-AAc)-shelled MBs exhibited both a significantly improved retention of the loaded Dox and a temperature-controlled release. At 37 °C, only ~20% of the loaded Dox was observed while ~90% was released in ~18 hrs.

5.5 References

[1] Dayton, P., et al., Acoustic radiation force in vivo: a mechanism to assist targeting of microbubbles. Ultrasound in medicine & biology, 1999. **25**(8): 1195-1201.

[2] Forsberg, F., W.T. Shi, and B. Goldberg, *Subharmonic imaging of contrast agents.*

Ultrasonics, 2000. **38**(1): 93-98.

[3] Kabalnov, A., et al., Dissolution of multicomponent microbubbles in the bloodstream: 1. Theory. Ultrasound in medicine & biology, 1998. **24**(5): 739-749.

[4] Kloek, W., T. van Vliet, and M. Meinders, Effect of bulk and interfacial rheological properties on bubble dissolution. Journal of Colloid and Interface Science, 2001. **237**(2): 158-166.

[5] Sirsi, S. and M. Borden, Microbubble compositions, properties and biomedical applications. Bubble Science, Engineering & Technology, 2009. **1**(1-2): 3-17.

[6] Christiansen, J.P., et al., Targeted tissue transfection with ultrasound destruction of plasmid-bearing cationic microbubbles. Ultrasound in medicine & biology, 2003. **29**(12): 1759-1767.

[7] Klibanov, A.L., Ligand-carrying gas-filled microbubbles: ultrasound contrast agents for targeted molecular imaging. Bioconjugate chemistry, 2005. **16**(1): 9-17.

[8] Martin, K.H. and P.A. Dayton, *Current status and prospects for microbubbles in ultrasound theranostics.* Wiley Interdisciplinary Reviews: Nanomedicine and Nanobiotechnology, 2013. **5**(4): 329-345.

[9] Quaia, E., Microbubble ultrasound contrast agents: an update. European radiology, 2007. **17**(8): 1995-2008.

[10] Cai, W. and X. Chen, Multimodality molecular imaging of tumor angiogenesis. Journal of Nuclear Medicine, 2008. **49**(Suppl 2): 113S-128S.

[11] Cherry, S.R. Multimodality imaging: Beyond pet/ct and spect/ct. in Seminars in nuclear medicine. 2009. Elsevier.

[12] Brismar, T.B., et al., Magnetite nanoparticles can be coupled to microbubbles to support

multimodal imaging. Biomacromolecules, 2012. **13**(5): 1390-1399.

[13] Janib, S.M., A.S. Moses, and J.A. MacKay, Imaging and drug delivery using theranostic nanoparticles. Advanced drug delivery reviews, 2010. **62**(11): 1052-1063.

[14] Kiessling, F., et al., Ultrasound microbubbles for molecular diagnosis, therapy, and theranostics. Journal of nuclear medicine, 2012. **53**(3): 345-348.

[15] Lindner, J.R., Microbubbles in medical imaging: current applications and future directions. Nature Reviews Drug Discovery, 2004. **3**(6): 527-533.

[16] Ferrara, K., R. Pollard, and M. Borden, Ultrasound microbubble contrast agents: fundamentals and application to gene and drug delivery. Biomedical Engineering, 2007. **9**.

[17] Sirsi, S.R. and M.A. Borden, Advances in ultrasound mediated gene therapy using microbubble contrast agents. Theranostics, 2012. **2**(12): 1208-1222.

[18] Mura, S., J. Nicolas, and P. Couvreur, Stimuli-responsive nanocarriers for drug delivery. Nature materials, 2013. **12**(11): 991-1003.

[19] Leong-Poi, H., et al., Therapeutic arteriogenesis by ultrasound-mediated VEGF165 plasmid gene delivery to chronically ischemic skeletal muscle. Circulation research, 2007. **101**(3): 295-303.

[20] Ting, C.-Y., et al., Concurrent blood–brain barrier opening and local drug delivery using drug-carrying microbubbles and focused ultrasound for brain glioma treatment. Biomaterials, 2012. **33**(2): 704-712.

[21] Weiss, R.B. The anthracyclines: will we ever find a better doxorubicin? in Seminars in oncology. 1992.

[22] Hortobagyi, G., Anthracyclines in the treatment of cancer. Drugs, 1997. **54**(4): 1-7.

[23] Momparler, R.L., et al., Effect of adriamycin on DNA, RNA, and protein synthesis in cell-

free systems and intact cells. Cancer research, 1976. **36**(8): 2891-2895.

[24] Fornari, F.A., et al., Interference by doxorubicin with DNA unwinding in MCF-7 breast tumor cells. Molecular pharmacology, 1994. **45**(4): 649-656.

[25] Pang, B., et al., Drug-induced histone eviction from open chromatin contributes to the chemotherapeutic effects of doxorubicin. Nature communications, 2013. **4**: 1908.

[26] Keizer, H., et al., Doxorubicin (adriamycin): a critical review of free radical-dependent mechanisms of cytotoxicity. Pharmacology & therapeutics, 1990. **47**(2): p. 219-231.

[27] Nemati, F., et al., Some parameters influencing cytotoxicity of free doxorubicin and doxorubicin-loaded nanoparticles in sensitive and multidrug resistant leucemic murine cells: incubation time, number of nanoparticles per cell. International journal of pharmaceutics, 1994. **102**(1-3): 55-62.

[28] Wang, S., et al., Doxorubicin induces apoptosis in normal and tumor cells via distinctly different mechanisms intermediacy of H2O2-and p53-dependent pathways. Journal of Biological Chemistry, 2004. **279**(24): 25535-25543.

[29] Lum, A.F., et al., Ultrasound radiation force enables targeted deposition of model drug carriers loaded on microbubbles. Journal of controlled release, 2006. **111**(1): 128-134.

[30] Rapoport, N., Z. Gao, and A. Kennedy, Multifunctional nanoparticles for combining ultrasonic tumor imaging and targeted chemotherapy. Journal of the National Cancer Institute, 2007. **99**(14): 1095-1106.

[31] Lentacker, I., et al., Design and evaluation of doxorubicin-containing microbubbles for ultrasound-triggered doxorubicin delivery: cytotoxicity and mechanisms involved. Molecular Therapy, 2010. **18**(1): 101-108.

[32] Cochran, M.C., et al., Doxorubicin and paclitaxel loaded microbubbles for ultrasound

triggered drug delivery. International journal of pharmaceutics, 2011. **414**(1): 161-170.

[33] Lentacker, I., S.C. De Smedt, and N.N. Sanders, Drug loaded microbubble design for ultrasound triggered delivery. Soft Matter, 2009. **5**(11): 2161-2170.

[34] Geers, B., et al., Crucial factors and emerging concepts in ultrasound-triggered drug delivery. Journal of controlled release, 2012. **164**(3): 248-255.

[35] Zhou, Y., Principles and Applications of Therapeutic Ultrasound in Healthcare. 2015: CRC Press.

[36] Borden, M.A., et al., DNA and polylysine adsorption and multilayer construction onto cationic lipid-coated microbubbles. Langmuir, 2007. **23**(18): 9401-9408.

[37] Ferrara, K.W., M.A. Borden, and H. Zhang, Lipid-shelled vehicles: engineering for ultrasound molecular imaging and drug delivery. Accounts of chemical research, 2009. **42**(7): 881-892.

[38] Camarozano, A.C., et al., Effects of microbubbles and ultrasound on the microcirculation: observation on the hamster cheek pouch. Journal of the American Society of Echocardiography, 2010. **23**(12): 1323-1330.

[39] Galaev, I. and B. Mattiasson, Smart polymers: applications in biotechnology and biomedicine. 2007: CRC Press.

[40] Samah, N.H.A. and C.M. Heard, Enhanced in vitro transdermal delivery of caffeine using a temperature-and pH-sensitive nanogel, poly (NIPAM-co-AAc). International journal of pharmaceutics, 2013. **453**(2): 630-640.

[41] Farooqi, Z.H., et al., Stability of poly (N-isopropylacrylamide-co-acrylic acid) polymer microgels under various conditions of temperature, pH and salt concentration. Arabian Journal of Chemistry, 2013.

[42] Mejac, I., et al., Visualizing the Lower Critical Solution Temperature Phase Transition of Individual Poly (Nipam)-Based Hydrogel Particles Using Near-Infrared Multispectral Imaging Microscopy. Analytical chemistry, 2010. **82**(5): 1698-1704.

[43] Perelman, L.A., et al., Preparation and Characterization of a pH-and Thermally Responsive Poly (N-isopropylacrylamide-co-acrylic acid)/Porous SiO2 Hybrid. Advanced functional materials, 2010. **20**(5): 826-833.

[44] Lue, S.J., C.-H. Chen, and C.-M. Shih, Tuning of lower critical solution temperature (LCST) of poly (N-isopropylacrylamide-co-acrylic acid) hydrogels. Journal of Macromolecular Science, Part B, 2011. **50**(3): 563-579.

[45] Ma, X., Bussonniere, A., & Liu, Q. (2017). A facile sonochemical synthesis of shell-stabilized reactive microbubbles using surface-thiolated bovine serum albumin with the Traut's reagent. *Ultrasonics Sonochemistry*, *36*, 454-465.

[46] Feshitan, J.A., et al., Microbubble size isolation by differential centrifugation. Journal of colloid and interface science, 2009. **329**(2): 316-324.

[47] Kaya, M. and P.A. Dayton, Changes in lipid-encapsulated microbubble population during continuous infusion and methods to maintain consistency. Ultrasound in medicine & biology, 2009. **35**(10): 1748-1755.

[48] Subedi, R.K., K.W. Kang, and H.-K. Choi, Preparation and characterization of solid lipid nanoparticles loaded with doxorubicin. European journal of pharmaceutical sciences, 2009. **37**(3): 508-513.

[49] Sanson, C., et al., A simple method to achieve high doxorubicin loading in biodegradable polymersomes. Journal of Controlled Release, 2010. **147**(3): 428-435.

[50] Sauerbrey, G., Verwendung von Schwingquarzen zur Wägung dünner Schichten und zur

Mikrowägung. Zeitschrift für physik, 1959. **155**(2): 206-222.

[51] Kayal, S. and R. Ramanujan, Doxorubicin loaded PVA coated iron oxide nanoparticles for targeted drug delivery. Materials Science and Engineering: C, 2010. **30**(3): 484-490.

[52] Mhlanga, N., et al., Polylactide-based Magnetic Spheres as Efficient Carriers for Anticancer Drug Delivery. ACS applied materials & interfaces, 2015. **7**(40): 22692-22701.

[53] Yuan, Q., et al., Controlled and extended drug release behavior of chitosan-based nanoparticle carrier. Acta biomaterialia, 2010. **6**(3): 1140-1148.

[54] Mirza, A.Z. and H. Shamshad, Preparation and characterization of doxorubicin functionalized gold nanoparticles. European journal of medicinal chemistry, 2011. **46**(5): 1857-1860.

[55] Cavalieri, F., et al., Ultrasonic synthesis of stable, functional lysozyme microbubbles. Langmuir, 2008. **24**(18): 10078-10083.

[56] Shchukina, E.M. and D.G. Shchukin, LbL coated microcapsules for delivering lipid-based drugs. Advanced drug delivery reviews, 2011. **63**(9): 837-846.

[57] Westwood, M., et al., Combined QCMD and AFM studies of lysozyme and poly-l-lysine–poly-galacturonic acid multilayers. Carbohydrate polymers, 2012. **89**(4): 1222-1231.

[58] Deligöz, H. and B. Tieke, QCM-D study of layer-by-layer assembly of polyelectrolyte blend films and their drug loading-release behavior. Colloids and Surfaces A: Physicochemical and Engineering Aspects, 2014. **441**: 725-736.

[59] Farooqi, Z.H., et al., Synthesis, characterization and fabrication of copper nanoparticles in N-isopropylacrylamide based co-polymer microgels for degradation of p-nitrophenol. Materials Science-Poland, 2015. **33**(1): 185-192.

[60] Dai, X., et al., Fluorescence intensity and lifetime imaging of free and micellar-

encapsulated doxorubicin in living cells. Nanomedicine: Nanotechnology, Biology and Medicine, 2008. **4**(1): 49-56.

[61] Mohan, P. and N. Rapoport, Doxorubicin as a molecular nanotheranostic agent: effect of doxorubicin encapsulation in micelles or nanoemulsions on the ultrasound-mediated intracellular delivery and nuclear trafficking. Molecular pharmaceutics, 2010. **7**(6): 1959-1973.

5.6 Supplemental Information

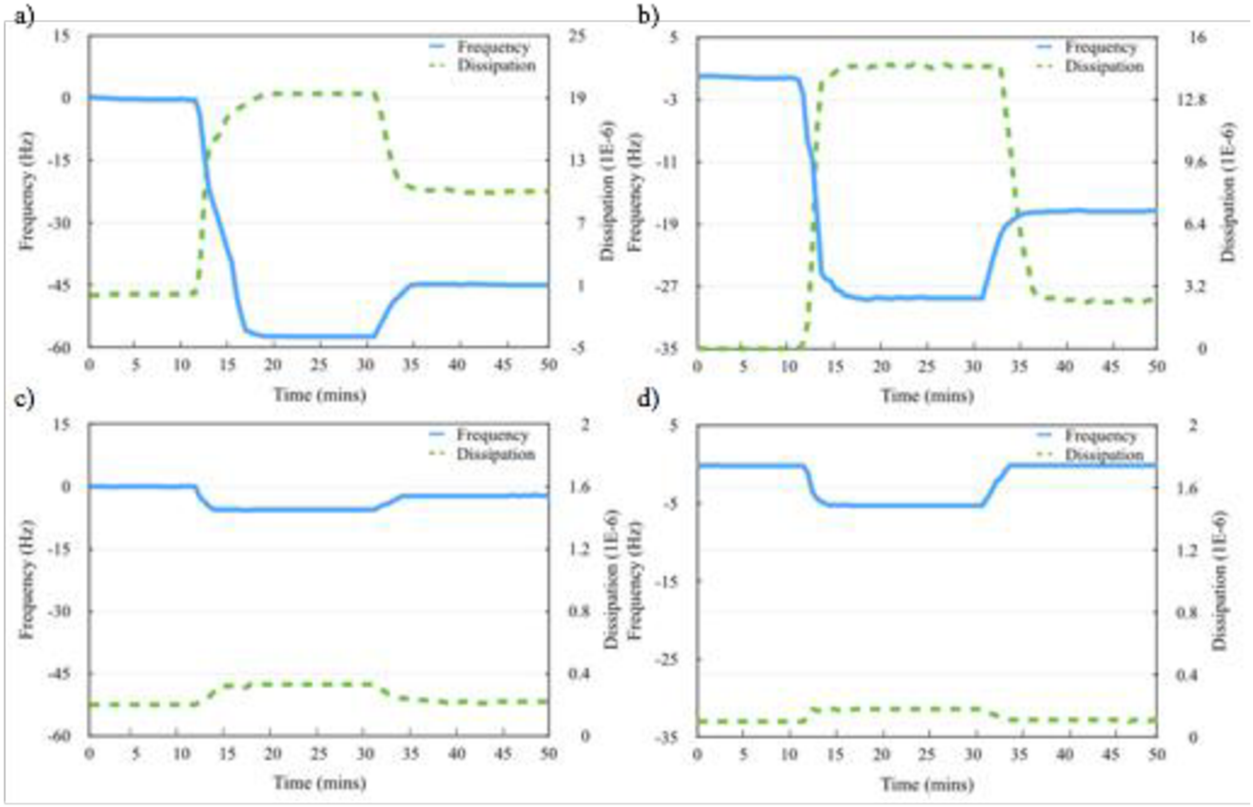

Figure 5.S1 Adsorptions of Dox-loaded MBs and poly(NIPAM-b-AAc)-shelled, Dox-loaded MBs on the Si_2O (a) and Al_2O_3 (b) surfaces, respectively at pH 7 were shown by a sharp decrease of frequency; however, unspecific adsorptions of Dox-loaded MBs and Poly(NIPAM-b-AAc)-shelled, Dox-loaded MBs were almost completely washed away from Al_2O_3 (c) and Si_2O

(d) at pH 7 due to the electrostatic repulsion.

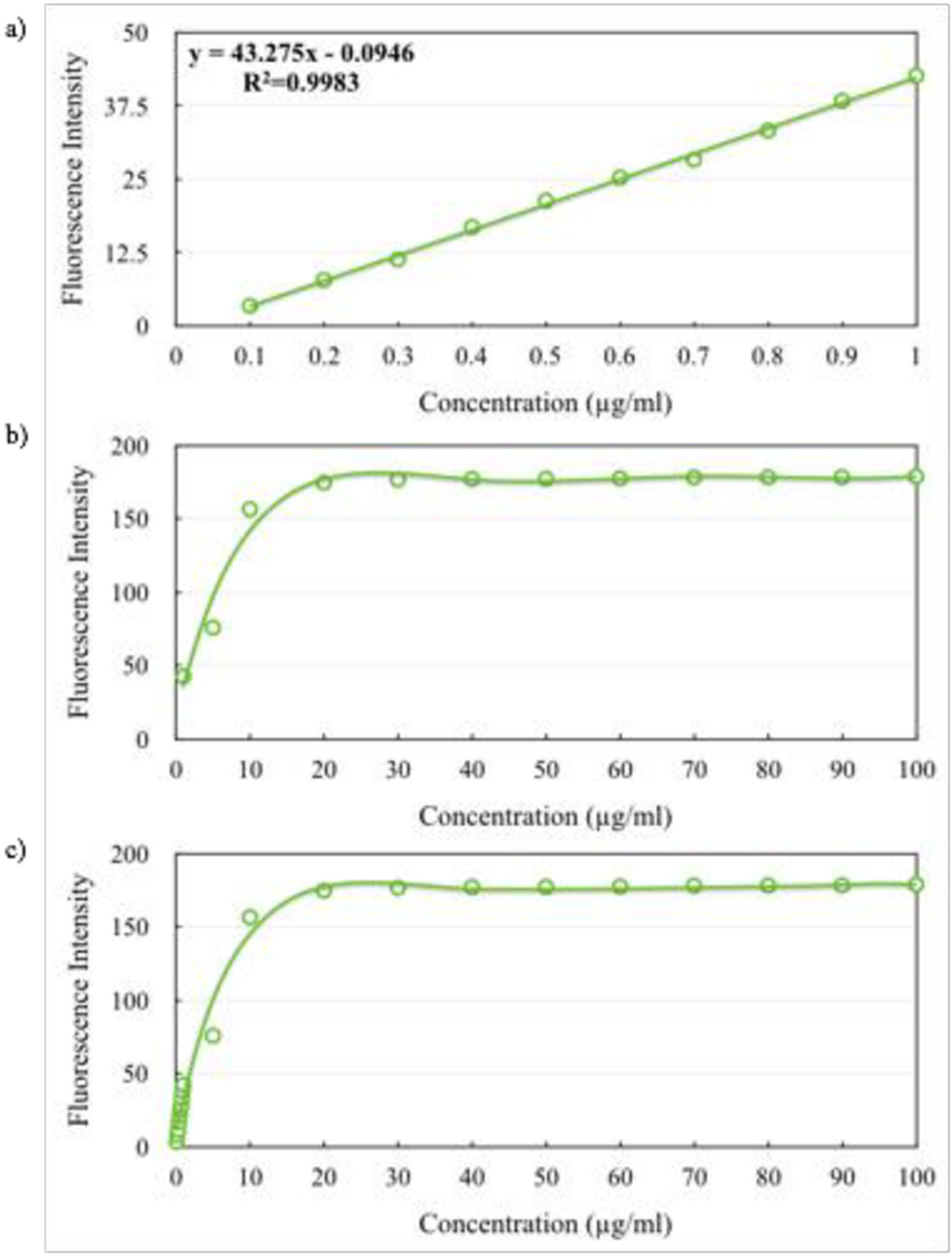

Figure 5.S2 The standard curves showing the dependance of fluorescence intensity of Dox on its concentration over a range from 0.1 to 1 µg/ml (a), 1 to 100 µg/ml (b), and 0.1 to 100 µg/ml (c).

Chapter 6 Optimization and kinetic study of the loadings of doxorubicin on proteinaceous microbubbles encapsulated by a poly(N-isopropylacrylamide)-block-(acrylic acid) shell[3]

6.1 Introduction

Microbubbles (MBs) have been proposed as a promising drug carrier because of its capability of being a theranostic agent which combines the diagnostic imaging and the on-site treatment [1-3]. Depending on the different shell materials, the properties of MBs can be fine-tuned to accommodate the needs of either functionalization or stimulus responsiveness [4,5]. Through chemical bonding or electrostatic interactions, the payload drugs are frequently anchored onto or into the surface of MBs [6,7]. Upon the exposure to certain stimuli, the loaded drugs can be released into the area of interest [8]. For example, ultrasound-triggered drug delivery using MBs greatly improve the ultrasound energy deposition in the tissues and increase the intracellular drug delivery [9].

Doxorubicin (Dox) has been widely used as a chemotherapeutic agent in both preliminary studies and clinical applications [10,11]. Dox can effectively prevents DNA transcription by intercalating with DNA and blocking the progression of an enzyme topoisomer [12]. It has been reported that Dox-loaded MBs killed at least two times more tumor cells than Dox-contained liposomes; in addition, a much more reduced cytotoxicity was observed due to the high accumulation of Dox at the tumor site when locally triggered [13]. Additionally, the utilization of

[3] A version of this chapter will be submitted for publication on *Colloids and Surfaces B: Biointerfaces*.

MBs as a Dox-carrier could greatly solve the disadvantages of administrating free Dox such as damage to healthy tissue cells and low accumulation of Dox at the targeted site [14-16]. Drug retention is therefore the key for Dox-loaded MBs to reduce the exposure of the healthy cells to Dox; for instance, a stable cross-linker or additional coating would be necessary to facilitate the drug retention [17, 18].

Gold nanoparticles (AuNPs), known for their unique optical and surface properties, have been widely used in many different fields including diagnostics, biomedical, and drug delivery [19,20]. Analogous to other metal nanoparticles (NPs), AuNPs can also be used to strength the stability of MBs by inhibiting gas diffusion and bubble coalescence [21]. In addition, the AuNPs-coated MBs provide both ultrasonic and photoacoustic responses, much better than either the ultrasonic response solely from MBs or the photoacoustic response solely from AuNPs. AuNPs, highly cited for their affinity to Dox, were once believed to interact with Dox by virtue of their electrostatic opposition [22, 23], and later accredited to the hydrophobic forces in place followed by cation-π interactions [24].

In our previous study, proteinaceous MBs were used as a template to load Dox electrostatically and further encapsulated by a temperature-sensitive poly(NIPAM-b-AAc) shell. Herein, we compared the loading efficiencies of Dox onto MBs with and without the aid of an in-between layer of AuNPs through UV/Vis and fluorescent spectrophotometric measurements. Different contributing factors of the loading of Dox onto the bare MBs were also investigated by varying the pH environment, dosages of MBs, temperature, and time. Based on the in-vitro release testing (IVRT), compared with the AuNPs-coated MBs, the poly(NIPAM-b-AAc)-shelled MBs

exclusively showed a temperature-sensitive release of Dox upon elevating the temperature from 37 to 39 °C. Based on the kinetic studies, such a temperature-controlled release was governed by the Korsmeyer-Peppas model, simultaneously controlled by the Fickian diffusion and the conformational change of the polymer shell.

6.2 Materials and Methods

Bovine serum albumin (BSA), Traut's reagent, gold chloride trihydrate, sodium citrate tribasic dehydrate, doxorubicin hydrochloride (Dox), N-Isopropylacrylamide (NIPAM), acrylic acid (AAc), 2,2′-Azobis(2-methylpropionitrile) (AIBN), and 2-Aminoethanethiol hydrochloride were obtained from Sigma Aldrich. Methanol and ethyl ether were obtained from Fisher Scientific. 2-Aminoethanethiol hydrochloride was purchased from Acros Organic. All chemicals were of analytical grade and used without further purification unless specified. Milli-Q water with a resistivity of 18.2 MΩ•cm was used for the all the experiments in this work.

6.2.1 Synthesis of MBs

As reported in our previous studies [25], proteinaceous MBs were prepared using surface-treated BSA with the Traut's agent. In brief, BSA (50 mg) was mixed with Traut's reagent (2 mg) in PBS (pH = 8, 1 ml) to react for 1 hr. The surface-treated BSA was given a heat shock at 45 °C and subsequently sonicated using a dismembrator (Fisher ScientificTM Model 705) at 173W for 45 sec. The synthesized MBs were collected and purified through either centrifugation [26] or column flotation [27].

6.2.2 Synthesis of AuNPs

AuNPs were synthesized according to the traditional Turkevich method [20, 28], refined by G. Frens [29]. In brief, 1 ml of 25 mM gold (III) chloride trihydrate solution was added to a round-bottom flask containing 99 ml of Milli-Q water. After bringing the mixture to boil, 1 ml of sodium citrate tribasic dehydrate solution (2.5 %) was quickly added to the reaction flask to react until the mixture stopped changing color, typically for 15-20 mins. The synthesized colloidal AuNPs were gradually cooled and later stored at 4 °C.

6.2.3 Synthesis of poly(NIPAM-b-AAc)

The synthesis of poly(NIPAM-b-AAc) was described as following. NIPAM (80 mmol), AAc (3.2 mmol), AIBN (1 mmol), and AET (1 mmol) were mixed in 40 ml of methanol followed by a nitrogen purge for 30 mins. The copolymerization was allowed to proceed at 60 °C for 16 hrs. The synthesized polymer was then purified from the unreacted reagents by selective precipitation. By drop-wisely adding into diethyl ether, the polymer was precipitated out while the unreacted monomers and other reagents were dissolved. The precipitated polymer was then filtered out and this selective precipitation procedure was repeated in triplicates. The purified poly(NIPAM-b-AAc) was further purified by dialyzing against Milli-Q water for five days followed by freeze drying (Labconco FreeZone 4.5) for storage.

6.2.4 Optimization of loadings of Dox onto MBs

Loading efficiencies of Dox onto MBs were initially compared by using or not using AuNPs as a coating onto MBs, as the AuNPs were reported to have an intrinsic affinity to Dox [22-24]. Due to the presence of free thiols on MBs, AuNPs could be easily coated onto MBs by forming the gold-sulfur bond [30, 31]. The partial and full deposition of AuNPs were achieved by fine-tuning the ratios of the AuNPs to MBs (v/v%) from 1:10 to 2:1. Following the reaction for one hr, the AuNPs-coated MBs were separated from the excessive AuNPs using flotation for three times. The full deposition of AuNPs on MBs (2:1, v/v%) was used to compare their affinity to Dox with the bare MBs'. Dox was then introduced to react with the bare MBs and the AuNPs-coated MBs for two hr, both of which were of the same quantity (5, 10, 25, 50 mg) for the purpose of comparison. Following the column purification, the free Dox remaining after the reaction was quantitatively compared using UV/Vis spectrophotometer described below. As a cross-check of those results, the Dox residues after the reaction with the bare MBs and the AuNPs-coated MBs of the two extreme values (1 and 10 mg) were doubly compared using fluorescent spectrophotometric measurement also described below. The effect of other contributing factors on the loading efficiencies onto MBs were also investigated by varying pH (2, 4, 6, 8, and 10), dosage of MBs (5, 10, 15, 20, 25, 30, 35, and 40 mg), temperature, (5, 15, 25, and 35 °C) and reaction time (4, 8, 12, 16, 20, 24, 28 min). After the reaction to MBs, the free Dox was collected and qualitatively compared using fluorescence spectrophotometer. The loading efficiency (w/w%) was calculated using the following equation:

$$\%\text{Loading efficiency} = \frac{I_{\text{Total}} - I_{\text{residue}}}{I_{\text{Total}}} \times 100$$

where I_{Total} and $I_{residue}$ are the fluorescence intensity of the total Dox before the reaction and the residue Dox after the reaction, respectively.

6.2.5 Successive loadings of Dox and poly(NIPAM-b-AAc) onto MBs

MBs (30 mg) were used to react with Dox (10 μg) in PBS (2ml) at 35 °C for 2 hrs. After the reaction, the Dox-loaded MBs were separated from the unreacted Dox through the column flotation at room temperature. After repeating this purification step for three times, the Dox-loaded MBs were introduced to react with excessive poly(NIPAM-b-AAc) (50 mg/ml) for 2 hrs to assemble a polymer outer shell. The poly(NIPAM-b-AAc) shelled, Dox-encapsulated MBs were then purified again through the column flotation

6.2.6 UV/Vis and fluorescent spectrophotometric measurements

To investigate the interaction between MBs and AuNPs and quantify the free Dox in the medium, UV/Vis absorbance measurements were carried out using a UV/Vis spectrometer (Varian Carey 50). Spectra were recorded in the range of 425 to 600 nm and 300 to 650 nm, respectively for the MBs-AuNPs interaction and the Dox measurement. The samples were diluted in Milli-Q water if needed and kept for the same dilution factor for quantitative measurements. Analogously, the fluorescent intensities of Dox were also carried out using a spectrofluorometer (Varian Carey Eclipse) and correlated with its concentration based on the experimentally established standard curves. The spectra of the fluorescence intensity at 575 ± 20 nm were recorded at an excitation wavelength of 490 nm.

6.2.7 Releasing profiles and kinetic studies

Dox-loaded MBs, Dox-loaded MBs with an in-between layer of AuNPs, Dox-loaded MBs with an outer poly(NIPAM-b-AAc) shell were respectively immersed into a dialysis tube containing 5 ml of PBS, and the tube was placed into a 50 ml PBS environment with a constant stirring at different temperatures for up to 40 h. 1 ml of the solution from the dialysate was withdrawn at one hr interval and replaced with fresh PBS to maintain the sink condition. The released Dox was subsequently quantified with a fluorescence spectrophotometer (Cary Eclipse FLR) by measuring the fluorescence intensity at 575 ± 20 nm when excited at 490 nm. Following the collection of the releasing profiles, different kinetic models, such as zero order, first order, Higuchi, and Korsmeyer-Peppas, were used to fit the data with a linear regression and to identify the nature of the Dox release [32, 33].

6.3 RESULTS AND DISCUSSION

6.3.1 Deposition of AuNPs onto MBs

AuNPs with a size of 150 ± 30 nm (Figure 6.1a) were synthesized using the conventional Turkevich method [20, 28] and subsequently loaded onto the surface of MBs. As reported in our previous paper, our synthesized MBs possess thiol groups on their outer surface. Due to the formation of strong gold-sulfur bonds [30, 31], gold nanoparticles can readily bind to MBs with a high affinity. The deposition of AuNPs on MBs was dually confirmed using UV/Vis

spectrophotometric measurements (Figure 6.2a) and SEM analysis (Figure 6.2b, c). The shift and broadening in the surface plasmon band of AuNPs from ~550 to ~565 nm (Figure 6.1a) verified the occurrence of the deposition because of the dependence of the surface plasmon resonance on

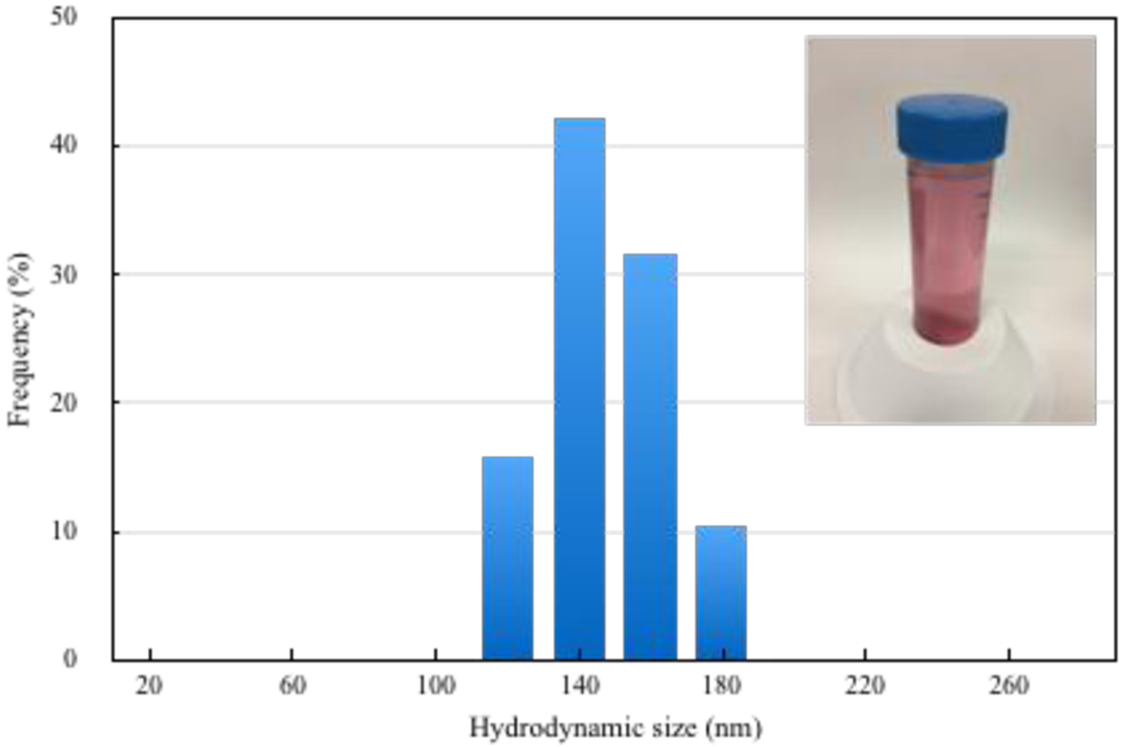

Figure 6.1 The hydrodynamic size distribution of the synthesized AuNPs (the inset) used for the deposition onto MBs

the size and shape of AuNPs [34-36]. In the range from 425 to 600 nm, bare MBs present no discernible peak, and the appearance of peaks at ~565 are attributable to the surface-loaded AuNPs, further demonstrating the success deposition of AuNPs on the MBs. As a cross-check, SEM analysis was performed to visualize the AuNPs-coated MBs directly. Due to a higher conductivity, AnNPs were shown with a much greater brightness than proteins as either brighter dots (Figure 6.2b) or brighter layers (Figure 6.2c). In detail, upon increasing the reaction ratio between AuNPs and MBs (v/v%), a higher surface coverage of AuNPs could be reached, and a

transition from a partial (Figure 6.2b) to a complete deposition of AuNPs on MBs was observed from the ratio of 1:5 to 2:1.

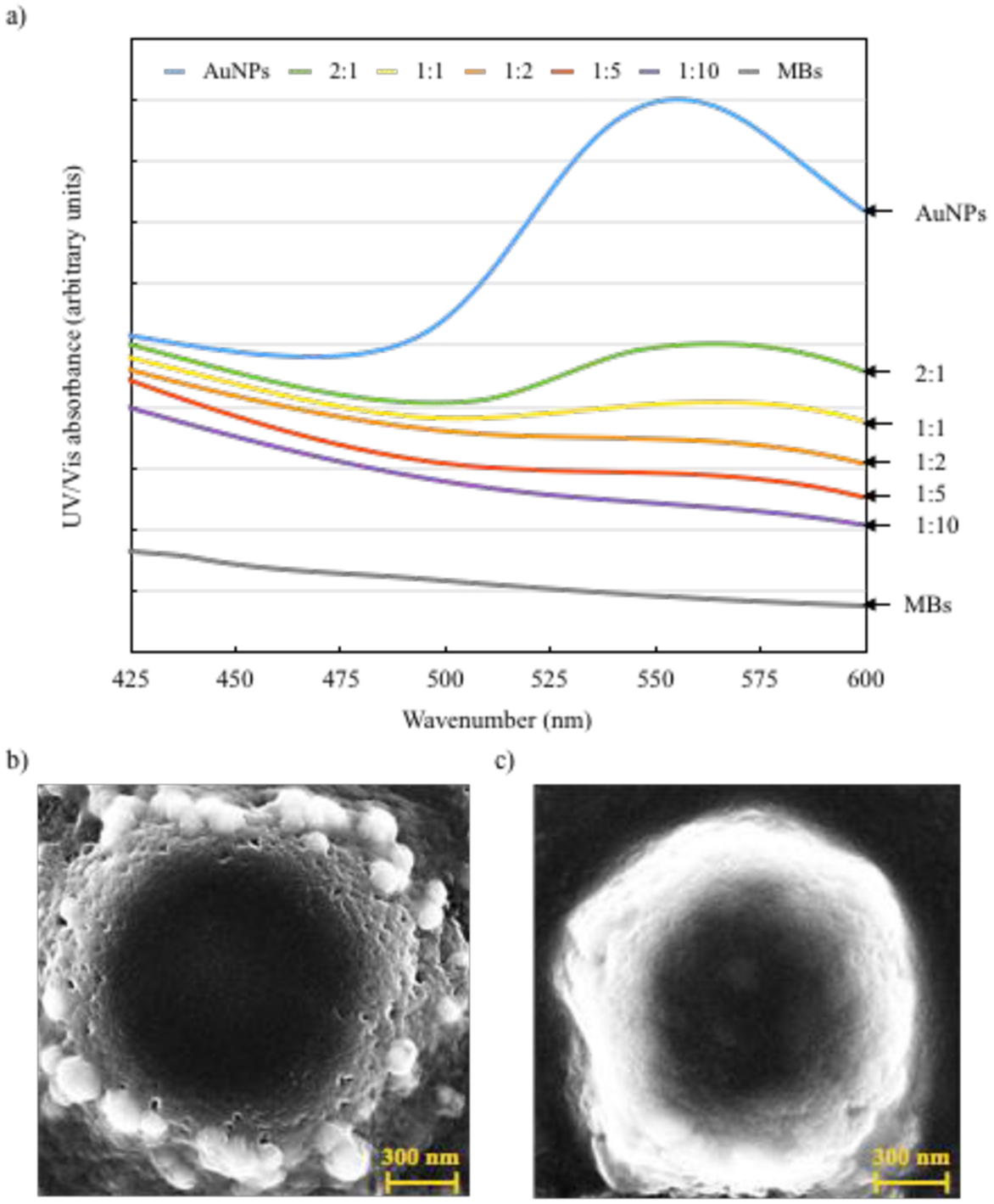

Figure 6.2 The depositions of AuNPs onto MBs in different ratios (v/v%) were confirmed by a shifted, broadened peak in the UV spectra(a). The partial (b) and complete (c) coverages of

AuNPs on MBs were achieved using the ratios (v/v%) of 1:5 and 2:1, respectively and recorded by SEM micrographs.

6.3.2 Comparison of the loading efficiencies of Dox onto AuNPs-MBs and bare MBs

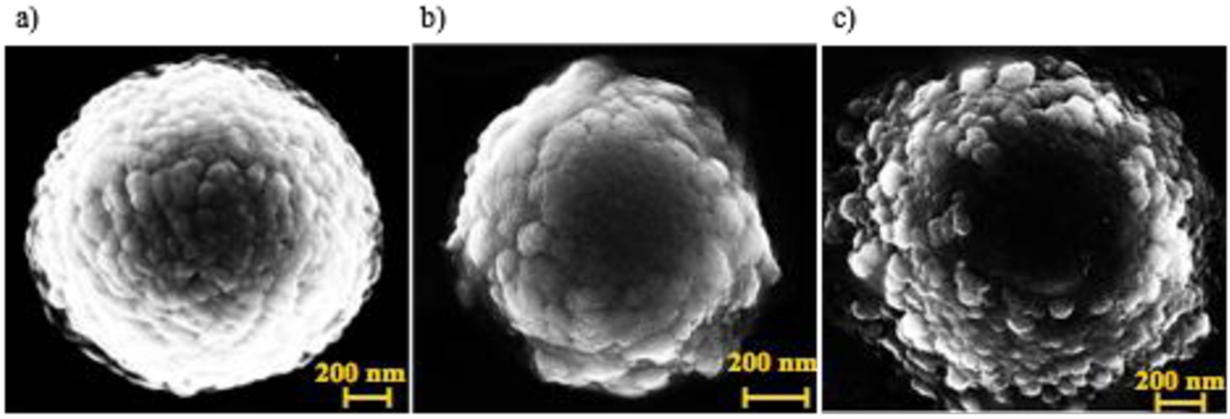

Figure 6.3 SEM micrographs of a bare MB (a), a Dox-loaded MB (b), and a Dox-loaded AuNP-MB (c).

The bare MBs carry a negative charge at the physiological pH [25], thereby facilitating the loading of the positively charge Dox onto their shell. As a result, efforts have been made to compare the loading efficiencies of Dox onto MBs with and without the in-between layer of AuNPs. Morphologically, a smoother texture appeared on the shell of MBs after the loading of Dox (Figure 6.3a, b). On the AuNPs-coated MBs, the loading of Dox predominantly occurred on the AuNPs, preserving its rough surface (Figure 6.3c). The characteristic absorbance peak of Dox at 490-498 nm has been widely used for quantifying its amount [23, 37-39], and the linear relationship between the UV/Vis absorbance and the concentration of free Dox was experimentally established (Figure 6.S1a, c, e). As the loading process consumes the free Dox, a

lower concentration of the free Dox, shown by a lower absorbance, remaining after the reaction indicates a higher loading efficiency. Upon elevating the amount of either the AuNPs-coated MBs (Figure 6.4a) or the bare MBs (Figure 6.4b) from 5 to 50 mg, a downward trend of the absorbance was shown, suggesting a stepped depletion of free Dox. It can also be readily seen

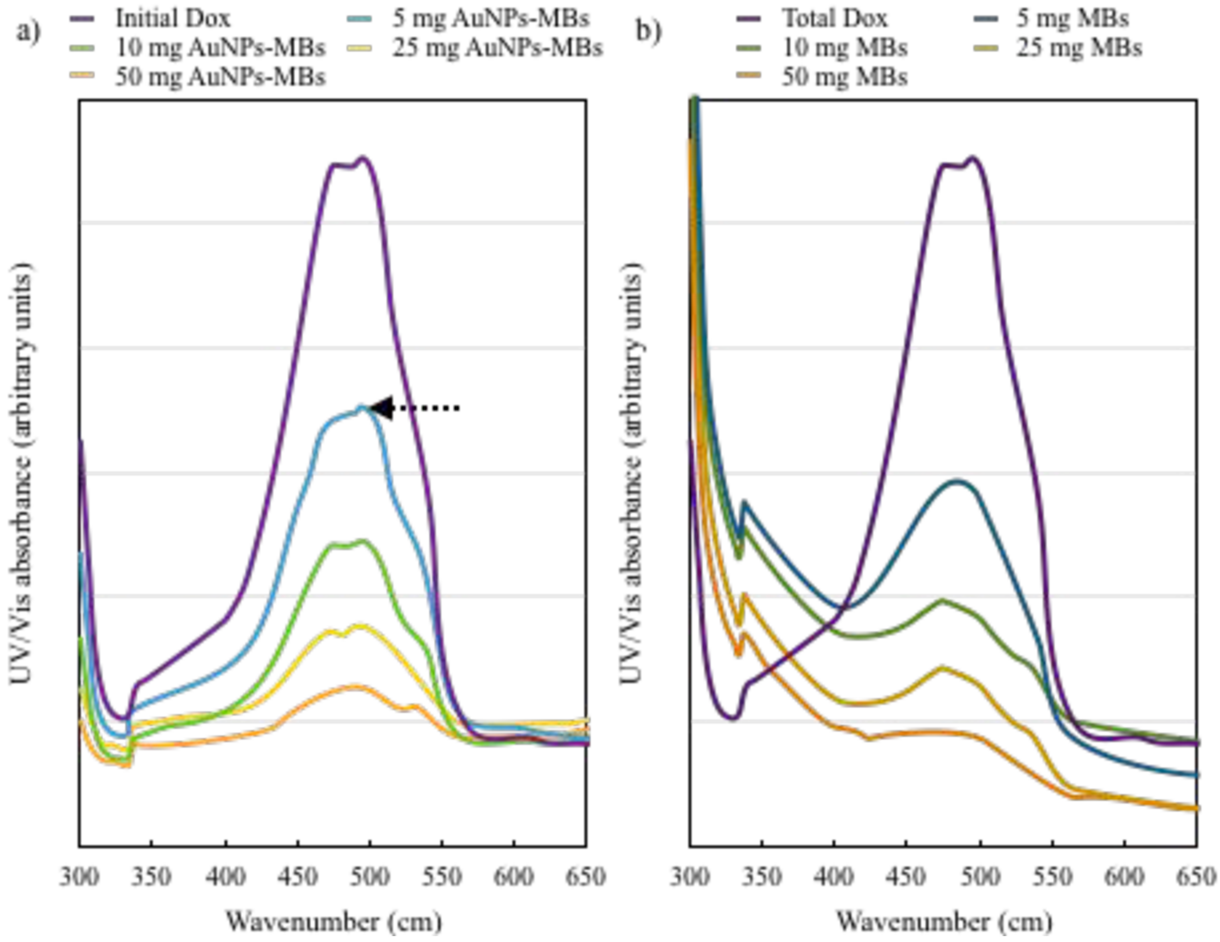

Figure 6.4 Following the loadings of DOX in various ratios onto AuNPs-MBs (a) and MBs (b), the unbound DOX remaining in the solution was quantified by UV absorbance measurements.

that the bare MBs have a higher affinity to Dox than the AuNPs-MBs, revealed by a greater magnitude of the drop in the concentration of free Dox (Figure 6.4a, b). In detail, the bare MBs

resulted in a drop of the UV/Vis absorbance, which is approximately 8-10 % more than AuNPs-coated MBs did, at each weight dosage (5, 10, 25, and 50 mg) (Figure 6.4a, b). The greater drop of the UV/Vis absorbance caused by the bare MBs indicates the higher loading efficiency of free Dox on the AuNPs-free MBs. As a cross-check, the free Dox was doubly quantified using its fluorescence intensity. As there is no discernible absorbance of either MBs or AuNPs-coated

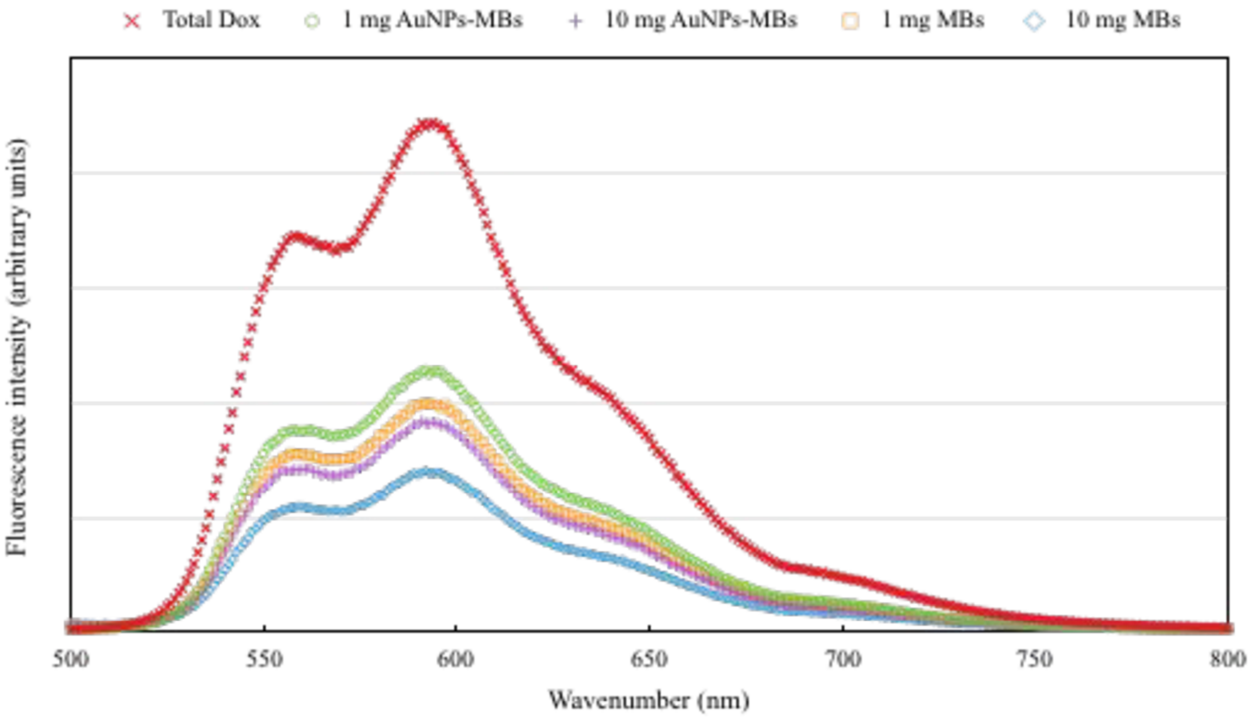

Figure 6.5 The free Dox after the loading onto AuNPs-coated MBs (1 and 10 mg) and MBs (1 and 10 mg) was quantified by fluorescence intensity measurements, and the loading efficiencies (the inset) were calculated respectively using the equation specified above.

MBs, the fluorescence emission was exclusively from Dox. The linear relationship between the fluorescence emission and the concentration of Dox was confirmed in a range from 0.1-1 μg/ml, and the non-linear relationship beyond this range might be from the self-quenching of Dox [40-41]. AuNPs-MBs and MBs at the two extreme weight dosages, 1 and 10 mg, were used to load

Dox, and the unbound Dox after the reaction was taken for the measurements of the fluorescence intensities at 590 nm (Figure 6.5). Analogously, a greater drop in fluorescence intensity was observed when MBs were used as a carrier than AuNP-MBs of the same weight, 1 and 10 mg, respectively (Figure 6.5). The drop of a greater magnitude in the fluorescence intensity of the free Dox was an evidence of a more effective loading process; specifically, the calculated loading efficiency (Figure 6.5, inset) revealed a ~10 % difference at both 1 and 10 mg weight dosage.

6.3.3 Optimizations of the Dox loading onto MBs

The loading of Dox onto MBs, primarily governed by the electrostatic interaction, was optimized by varying several contributing factors, namely pH (Figure 6.6a), dosages of MBs (Figure 6.6c), temperature (Figure 6.6e), and reaction time (Figure 6.6g). Fluorescent spectrophotometric measurements of the free Dox after the loading process were performed (Figure 6.6a, c, e, g), and the loading efficiency at each condition was respectively calculated (Figure 6.6b, d, f, h). At pH 6, the fluorescence intensities of the free Dox was the lowest (Figure 6.6a), indicating the highest loading efficiency of Dox compared to other pH environments (Figure 6.6b). With a slightly basic pKa (8.3) [42, 43], Dox was positively charged at pH 6 because of its amine moiety; in the meantime, the bare MBs (pKa = 4.5) were negatively charged, creating an electrostatic opposition. The loading efficiency of Dox reached its maximum to approximately 80% at pH 6 (Figure 6.6b), where the electrostatic interactions were expected to be the strongest. At other pH conditio6.ns, the free Dox remaining after the loading was much more than that at pH 6 (Figure 6.6a), shown as a greater magnitude of fluorescence intensity. The major

contribution of the electrostatic interaction was also revealed from the relatively low loading efficiency at pH 2 and 4. Dox and MBs were both positively charged at pH 2 and pH 4, and the loading of Dox became unfavorable shown by a much-reduced loading efficiency of ~44 % and

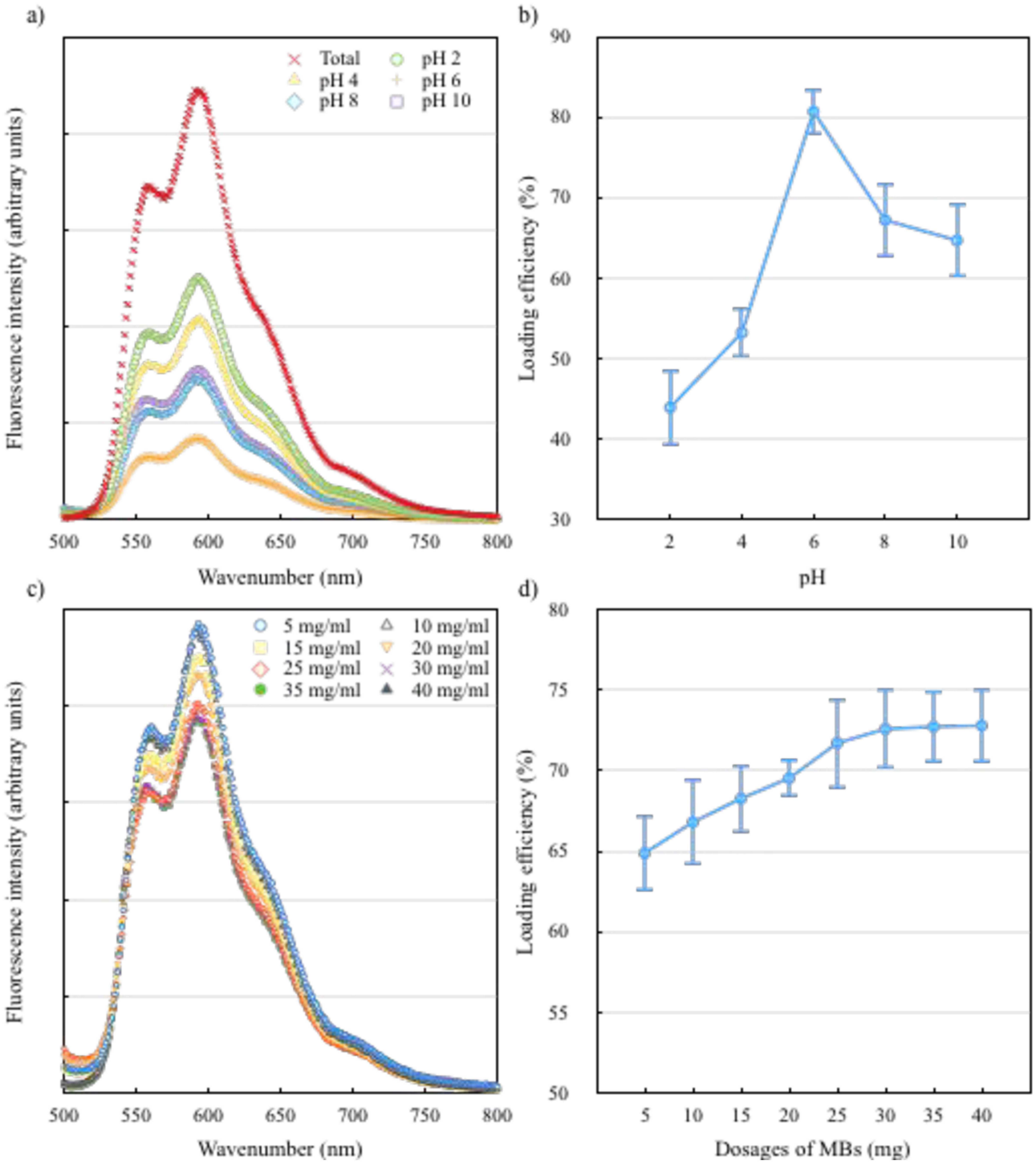

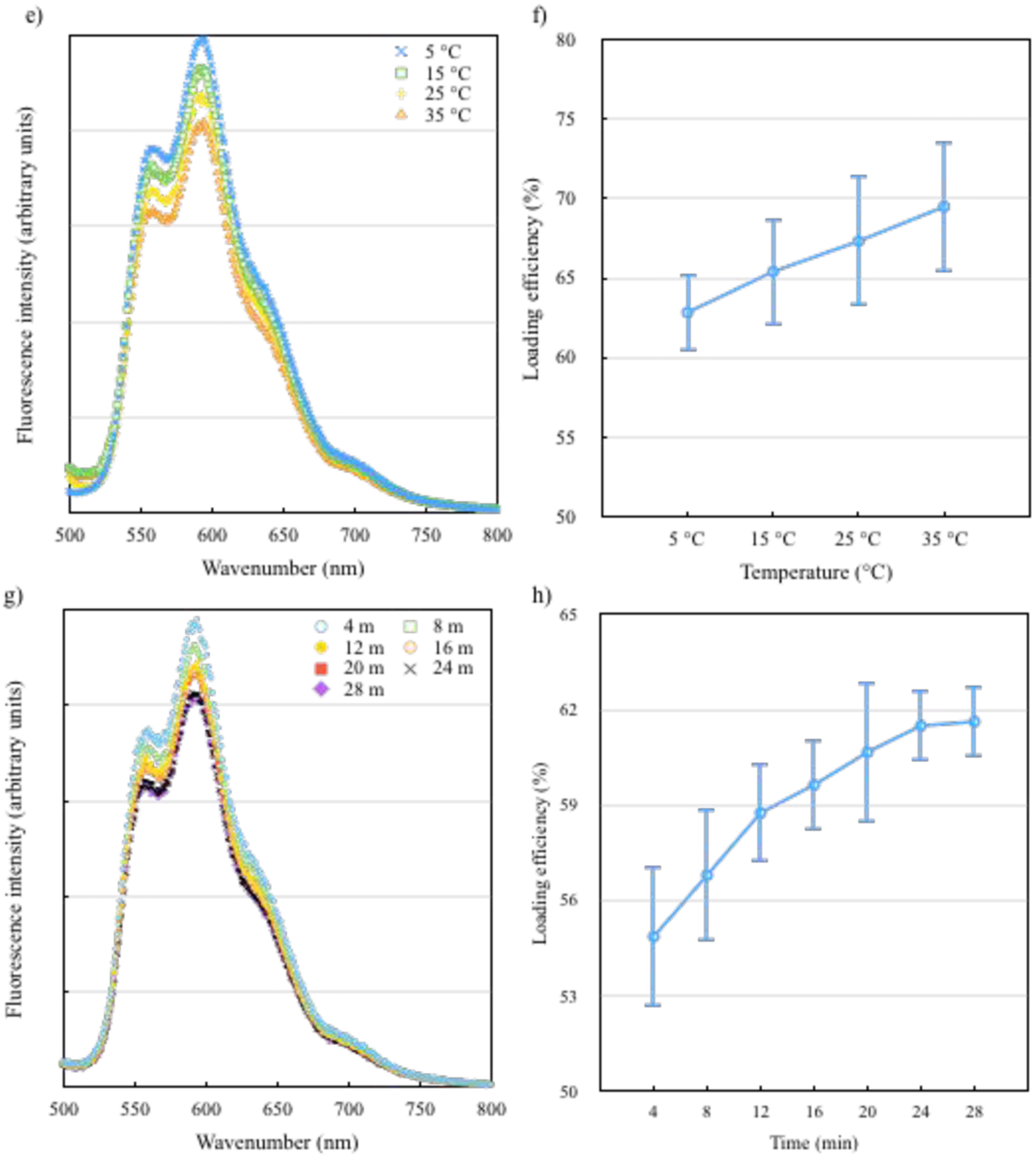

Figure 6.6 The fluorescence intensities of free Dox after the loading were measured by varying pH (a), dosage of MBs (c), temperature (e), and reaction time (g) and used to calculate the loading efficiencies, respectively ((b), (d), (f), and (h)).

~52% (Figure 6.6b). Analogously, Dox became nearly and completely neutrally-charged at pH 8 and 10, respectively, and the reduced electrostatic opposition resulted in a lowered loading efficiency (Figure 6.6b). The loading efficiency was also improved by introducing the number of MBs available to be loaded; however, a plateau was reached until 30 mg/ml of MBs were used to react with 10 μg of Dox (Figure 6.6c, d). Any dosages of MBs above 30 mg/ml did not yield any noticeably higher loading efficiency possibly because the limit of Dox loading was reached by solely varying the dosage of MBs. In addition to the effect of pH and dosage of MBs, an elevated temperature also moderately improved the loading process. From 5 to 35 °C, the loading efficiency was boosted by nearly 10% (Figure 6.6e, f), suggesting the endothermic nature of the loading process. Temperatures above 35 °C were not considered because of the possible adverse effect of temperature on the structure of proteinaceous MBs. On the kinetic aspect, it was shown that the loading of Dox onto MBs was a relatively quick process, reaching a loading efficiency of over 50% within 4 mins and terminating within 30 mins (Figure 6.6g, h). As aforementioned, the optimal condition for loading Dox onto MBs was determined to be the reaction of Dox (10 μg/ml) with MBs (30 mg/ml) at pH 6 and 35 °C for at least 30 mins, and such condition was therefore used for all subsequent experiments.

6.3.4 IVRT and kinetic studies of Dox from Dox-loaded AuNPs-MBs and Dox-loaded MBs with a poly(NIPAM-b-AAc) shell

Compared to the AuNPs-coated, Dox-loaded MBs, the superior capability of retaining the loaded Dox from the poly(NIPAM-b-AAc)-shelled, Dox-loaded MBs was demonstrated through the comparison of their IVRT profiles (Figure 6.7a, b). At room temperature (23 °C), the polymer-

shelled MBs retained the loaded Dox for 40 hrs without showing any appreciable premature release (Figure 6.7a), which in turn proves the role of the leak-proof polymer shell [17]. On the other hand, AuNPs-MBs released nearly 70 % of the payload to the releasing media within 8 hrs (Figure 6.7b). With a small difference between 37 °C and 39 °C, ~85% of the loaded Dox was released into the media from AuNPs within 6 hrs (Figure 6.7a). In comparison, the polymer-shelled MBs exhibited a sensitive response when heated from 37 °C to 39 °C, releasing from ~20% to ~90% (Figure 6.7b).

To further investigate the releasing behavior of the Dox-loaded MBs with a poly(NIPAM-b-AAc) shell, the data were fitted into zero order, first order, Higuchi, and Korsmeyer-Peppas kinetic models [32, 33]. The releasing rate constants (K_0, K_1, K_H, and K_{KP}) and the associated correlation coefficients (R^2) for all the models were summarized (Figure 6.8, 6.S2), and the fittings were evaluated based on the proximity of R^2 to 1. It was readily seen that the Korsmeyer-Peppas model was the best-fitted one because of the highest R^2 values of 0.9913 and 0.9962, respectively for the releasing profiles at 37 and 39 °C. For both swellable and non-swellable systems, the classic empirical law [44]

$$M_t/M_f = K_{KP}\, t^n$$

where M_t/M_f, n, K_{KP}, and t stand for the percentage of the released payload at time t, the release exponent, the release rate constant, and time t, respectively, could be used to identify if the release of payload drug follows the Fickian, non-Fickian (anomalous), or Case II mechanism [44, 45]. After the logarithm transformation, the Korsmeyer-Peppas equation [44] becomes to the

following:

$$\log (M_t/M_f) = n \log (t) + \log K_{KP}.$$

The K_{KP} value is a carrier-dependent parameter depending on the intrinsic properties of various releasing systems, and the n value is utilized to characterize different releases. In detail, for n =

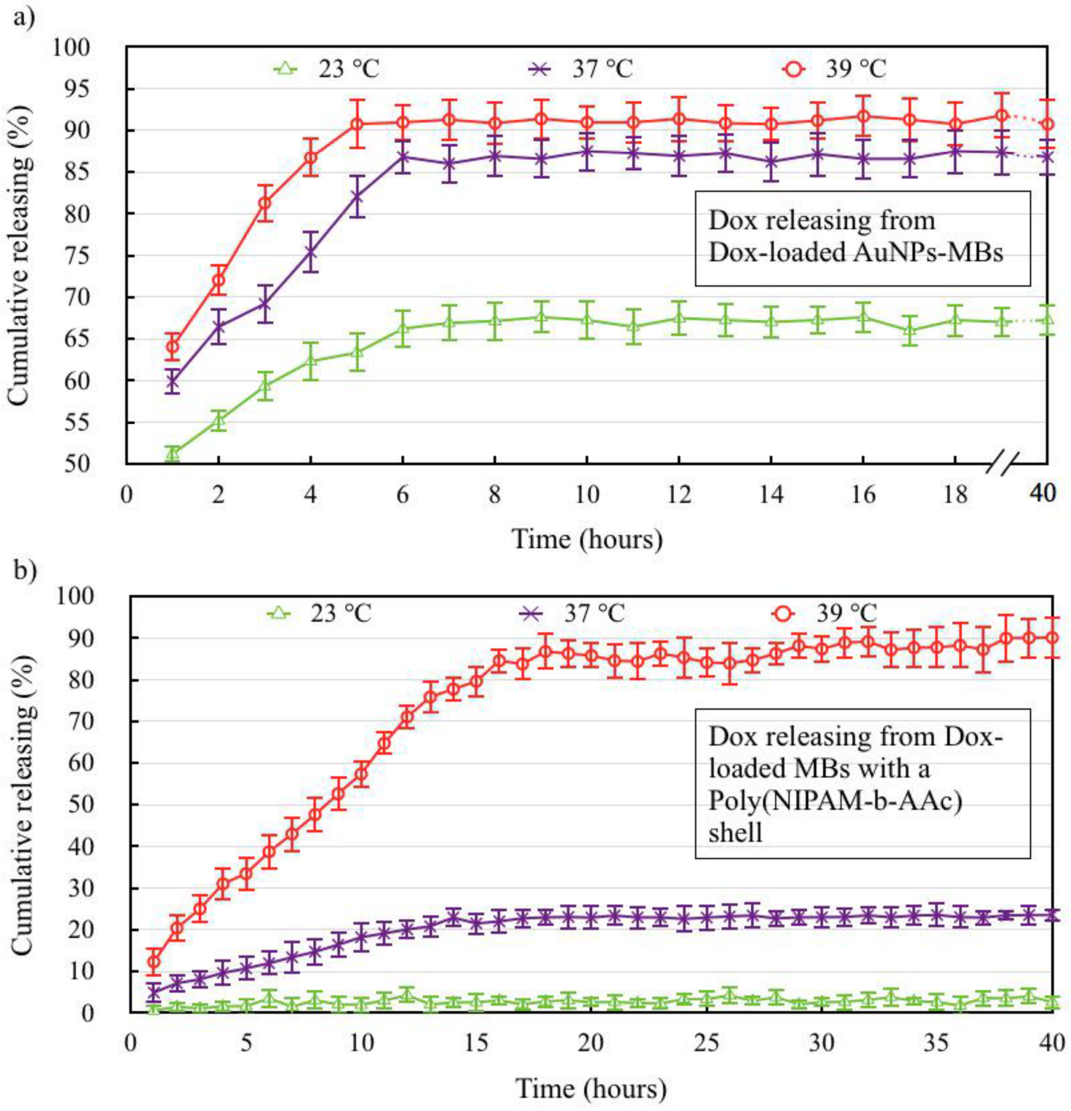

Figure 6.7 Dox releasing profiles from Dox-loaded, AuNPs-MBs (a) and MBs with a poly(NIPAM-b-AAc) shell (b).

	Zero order		First order		Higuchi		Korsmeyer-Peppas	
	K_0	R^2	K_1	R^2	K_H	R^2	K_{KP}	R^2
37°C	4.895	0.9864	0.049	0.9091	0.265	0.9749	0.503	0.9913
39°C	1.2111	0.9739	0.040	0.9122	0.217	0.9773	0.425	0.9962

Figure. 6.8 The releasing rate constants (K_0, K_1, K_H, and K_{KP} for zero order, first order, Higuchi, and Korsmeyer-Peppas, respectively) and correlation coefficient (R^2) for polymer-shelled, Dox-loaded MBs at 37 and 39°C.

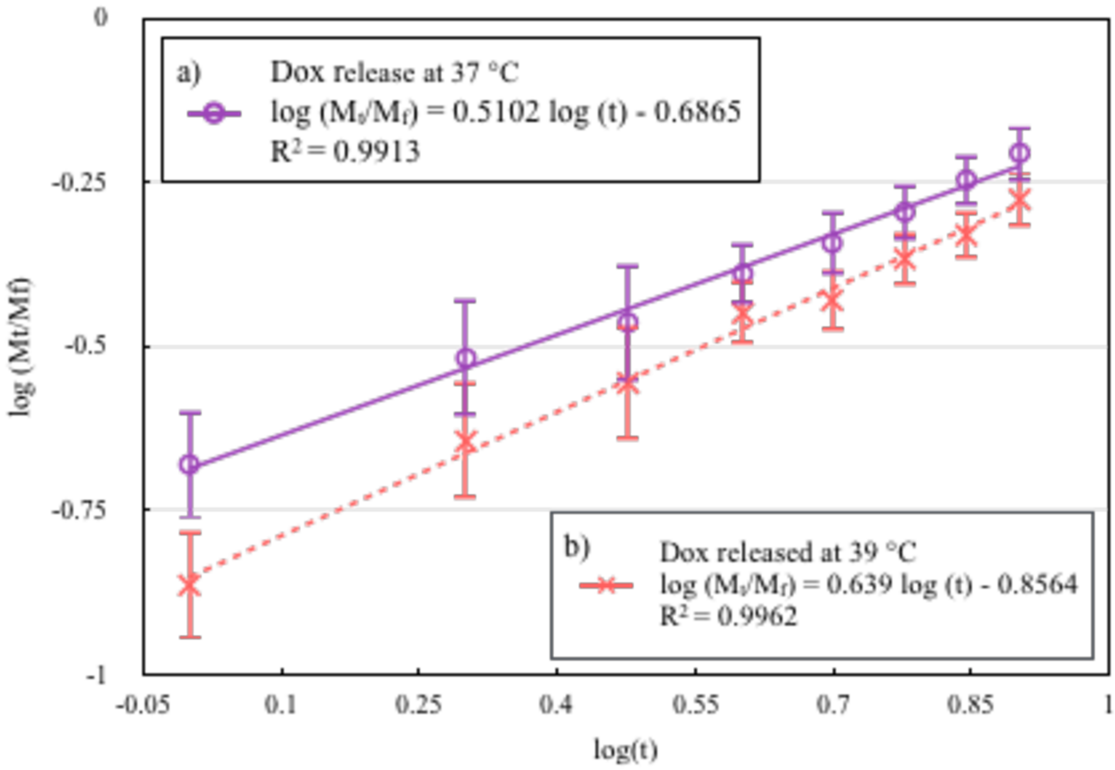

Figure 6.9 Korsmeyer-Peppas fitted Dox release from the poly(NIPAM-b-AAc)-shelled, Dox-loaded MBs at 37 °C (a) and 39 °C (b), respectively, where M_t, M_f, and t stand for the released amount at time t, the final released amount, and time t, respectively. The linear fitted equation was included in the inlets along with the associated R-squared values.

0.50/0.45/0.43, pure Fickian release from slabs/cylinders/spheres can be identified where the concentration gradient dominates the payload release [44, 45]. For $0.5/0.45/0.43 < n < 1/1/1$ and $0.5/0.45/0.43 < n < 1/0.89/0.85$, anomalous release was indicated for release from non-swellable and swellable slabs/cylinders/spheres, respectively [44, 45]. For $1/1/1 < n$ and $1/0.89/0.85$, Case II release was confirmed from non-swellable and swellable slabs/cylinders/spheres, respectively [44, 45]. Based on the linear regression (Figure 6.9a, b), the n values of 0.510 and 0.639 for 37 and 39 °C were shown, revealing the nature of the Dox release from poly(NIPAM-b-AAc)-shelled, Dox-loaded MBs to be anomalous. The mechanism of Dox release was therefore dually governed by Fickian diffusion and polymer relaxation that is also previously referred as the "squeezing" mechanism of temperature-sensitive polymers [46]. As the temperature was elevated above the LCST of the poly(NIPAM-b-AAc) shell, the polymer shrank to a smaller size, expelling the aqueous solution and forming a densely-packed conformation. It was previously reported that such a conformational change leads to either a slower or faster release, varying from study to study [46]. In our case, a nearly 4 times faster release was observed (Figure 6.7b) when the temperature was elevated from 37 to 39 °C, indicative of the critical role of the conformational change of the polymer shell during the temperature-induced release. A plausible explanation for the faster release at 39 °C is that, in addition to the Fickian diffusion, the shrunk polymer causes a higher exposure of Dox to the aqueous solution, collectively contributing to the gradual Dox release over a period of ~18 h.

6.4 Conclusions

For the loadings of Dox onto proteinaceous MBs, the loading efficiencies of Dox were compared

and optimized by using AuNPs as an intermediate layer, pH, dosage of MBs, temperature, and time through UV/Vis and fluorescent spectrophotometric measurements. Compared to the Dox release from the AuNPs-coated MBs, the poly(NIPAM-b-AAc)-shelled MBs exhibited a temperature-controlled release. At 39 °C, ~90% of the loaded Dox was released in ~18h while only ~20% was detected at 37 °C. Based on the kinetic study, the release of Dox from the poly(NIPAM-b-AAc)-shelled MBs follows the Korsmeyer-Peppas model, where the Fickian diffusion and the conformational change of the polymer shell collectively regulate the release of Dox.

6.5 References

[1] Janib, S.M., A.S. Moses, and J.A. MacKay, Imaging and drug delivery using theranostic nanoparticles. Advanced drug delivery reviews, 2010. 62(11): 1052-1063.

[2] Kiessling, F., et al., Ultrasound microbubbles for molecular diagnosis, therapy, and theranostics. Journal of nuclear medicine, 2012. 53(3): 345-348.

[3] Martin, K.H. and P.A. Dayton, *Current status and prospects for microbubbles in ultrasound theranostics.* Wiley Interdisciplinary Reviews: Nanomedicine and Nanobiotechnology, 2013. 5(4): 329-345.

[4] Christiansen, J.P., et al., Targeted tissue transfection with ultrasound destruction of plasmid-bearing cationic microbubbles. Ultrasound in medicine & biology, 2003. 29(12): 1759-1767.

[5] Klibanov, A.L., Ligand-carrying gas-filled microbubbles: ultrasound contrast agents for targeted molecular imaging. Bioconjugate chemistry, 2005. 16(1): 9-17.

[6] Ferrara, K., R. Pollard, and M. Borden, Ultrasound microbubble contrast agents: fundamentals and application to gene and drug delivery. Biomedical Engineering, 2007. 9.

[7] Sirsi, S.R. and M.A. Borden, Advances in ultrasound mediated gene therapy using microbubble contrast agents. Theranostics, 2012. 2(12): 1208-1222.

[8] Mura, S., J. Nicolas, and P. Couvreur, Stimuli-responsive nanocarriers for drug delivery. Nature materials, 2013. 12(11): 991-1003.

[9] Hernot, S. and A.L. Klibanov, Microbubbles in ultrasound-triggered drug and gene delivery. Advanced drug delivery reviews, 2008. 60(10): 1153-1166.

[10] Weiss, R.B. The anthracyclines: will we ever find a better doxorubicin? in Seminars in oncology. 1992.

[11] Hortobagyi, G., Anthracyclines in the treatment of cancer. Drugs, 1997. 54(4): 1-7.

[12] Momparler, R.L., et al., Effect of adriamycin on DNA, RNA, and protein synthesis in cell-free systems and intact cells. Cancer research, 1976. 36(8): 2891-2895.

[13] Lentacker, I., et al., Design and evaluation of doxorubicin-containing microbubbles for ultrasound-triggered doxorubicin delivery: cytotoxicity and mechanisms involved. Molecular Therapy, 2010. 18(1): 101-108.

[14] Keizer, H., et al., Doxorubicin (adriamycin): a critical review of free radical-dependent mechanisms of cytotoxicity. Pharmacology & therapeutics, 1990. 47(2): 219-231.

[15] Nemati, F., et al., Some parameters influencing cytotoxicity of free doxorubicin and doxorubicin-loaded nanoparticles in sensitive and multidrug resistant leucemic murine cells: incubation time, number of nanoparticles per cell. International journal of pharmaceutics, 1994. 102(1-3): 55-62.

[16] Wang, S., et al., Doxorubicin induces apoptosis in normal and tumor cells via distinctly

different mechanisms intermediacy of H2O2-and p53-dependent pathways. Journal of Biological Chemistry, 2004. 279(24): 25535-25543.

[17] Geers, B., et al., Crucial factors and emerging concepts in ultrasound-triggered drug delivery. Journal of controlled release, 2012. 164(3): 248-255.

[18] Zhou, Y., Principles and Applications of Therapeutic Ultrasound in Healthcare. 2015: CRC Press.

[19] Yeh, Y.-C., B. Creran, and V.M. Rotello, Gold nanoparticles: preparation, properties, and applications in bionanotechnology. Nanoscale, 2012. 4(6): 1871-1880.

[20] Zhao, P., N. Li, and D. Astruc, State of the art in gold nanoparticle synthesis. Coordination Chemistry Reviews, 2013. 257(3): 638-665.

[21] Mohamedi, G., et al., Effects of gold nanoparticles on the stability of microbubbles. Langmuir, 2012. 28(39): 13808-13815.

[22] Mirza, A.Z. and H. Shamshad, Preparation and characterization of doxorubicin functionalized gold nanoparticles. European journal of medicinal chemistry, 2011. 46(5): 1857-1860.

[23] Elbialy, N.S., M.M. Fathy, and W.M. Khalil, Preparation and characterization of magnetic gold nanoparticles to be used as doxorubicin nanocarriers. Physica Medica, 2014. 30(7): 843-848.

[24] Curry, D., et al., Adsorption of doxorubicin on citrate-capped gold nanoparticles: insights into engineering potent chemotherapeutic delivery systems. Nanoscale, 2015. 7(46): 19611-19619.

[25] Ma, X., Bussonniere, A., & Liu, Q. (2017). A facile sonochemical synthesis of shell-stabilized reactive microbubbles using surface-thiolated bovine serum albumin with the Traut's

reagent. *Ultrasonics Sonochemistry*, *36*, 454-465.

[26] Feshitan, J.A., et al., Microbubble size isolation by differential centrifugation. Journal of colloid and interface science, 2009. 329(2): 316-324.

[27] Kaya, M. and P.A. Dayton, Changes in lipid-encapsulated microbubble population during continuous infusion and methods to maintain consistency. Ultrasound in medicine & biology, 2009. 35(10): 1748-1755.

[28] Kimling, J., et al., Turkevich method for gold nanoparticle synthesis revisited. The Journal of Physical Chemistry B, 2006. 110(32): 15700-15707.

[29] Frens, G., Controlled nucleation for the regulation of the particle size in monodisperse gold suspensions. Nature, 1973. 241(105): 20-22.

[30] Giljohann, D.A., et al., *Gold nanoparticles for biology and medicine.* Angewandte Chemie International Edition, 2010. 49(19): 3280-3294.

[31] Häkkinen, H., The gold-sulfur interface at the nanoscale. Nature chemistry, 2012. 4(6): 443-455.

[32] Dash, S., et al., Kinetic modeling on drug release from controlled drug delivery systems. Acta Pol Pharm, 2010. 67(3): 217-23.

[33] Singhvi, G. and M. Singh, Review: in-vitro drug release characterization models. Int J Pharm Stud Res, 2011. 2(1): 77-84.

[34] Storhoff, J.J., et al., One-pot colorimetric differentiation of polynucleotides with single base imperfections using gold nanoparticle probes. Journal of the American Chemical Society, 1998. 120(9): 1959-1964.

[35] Haiss, W., et al., Determination of size and concentration of gold nanoparticles from UV-vis spectra. Analytical chemistry, 2007. 79(11): 4215-4221.

[36] Amendola, V. and M. Meneghetti, Size evaluation of gold nanoparticles by UV− vis spectroscopy. The Journal of Physical Chemistry C, 2009. 113(11): 4277-4285.

[37] Shuai, X., et al., Micellar carriers based on block copolymers of poly (ε-caprolactone) and poly (ethylene glycol) for doxorubicin delivery. Journal of Controlled Release, 2004. 98(3): 415-426.

[38] Tian, Y., et al., Complexation and release of doxorubicin from its complexes with pluronic P85-b-poly (acrylic acid) block copolymers. Journal of Controlled Release, 2007. 121(3): 137-145.

[39] Zhang, X., et al., Targeted delivery and controlled release of doxorubicin to cancer cells using modified single wall carbon nanotubes. Biomaterials, 2009. 30(30): 6041-6047.

[40] Dai, X., et al., Fluorescence intensity and lifetime imaging of free and micellar-encapsulated doxorubicin in living cells. Nanomedicine: Nanotechnology, Biology and Medicine, 2008. 4(1): 49-56.

[41] Mohan, P. and N. Rapoport, Doxorubicin as a molecular nanotheranostic agent: effect of doxorubicin encapsulation in micelles or nanoemulsions on the ultrasound-mediated intracellular delivery and nuclear trafficking. Molecular pharmaceutics, 2010. 7(6): 1959-1973.

[42] Subedi, R.K., K.W. Kang, and H.-K. Choi, Preparation and characterization of solid lipid nanoparticles loaded with doxorubicin. European journal of pharmaceutical sciences, 2009. 37(3): 508-513.

[43] Sanson, C., et al., A simple method to achieve high doxorubicin loading in biodegradable polymersomes. Journal of Controlled Release, 2010. 147(3): 428-435.

[44] Ritger, P.L. and N.A. Peppas, A simple equation for description of solute release II. Fickian and anomalous release from swellable devices. Journal of controlled release, 1987. 5(1):

37-42.

[45] Ritger, P.L. and N.A. Peppas, A simple equation for description of solute release I. Fickian and non-Fickian release from non-swellable devices in the form of slabs, spheres, cylinders or discs. Journal of controlled release, 1987. 5(1): 23-36.

[46] Trongsatitkul, T. and B.M. Budhlall, Microgels or microcapsules? Role of morphology on the release kinetics of thermoresponsive PNIPAm-co-PEGMa hydrogels. Polymer Chemistry, 2013. 4(5): 1502-1516.

6.6 Supplemental information

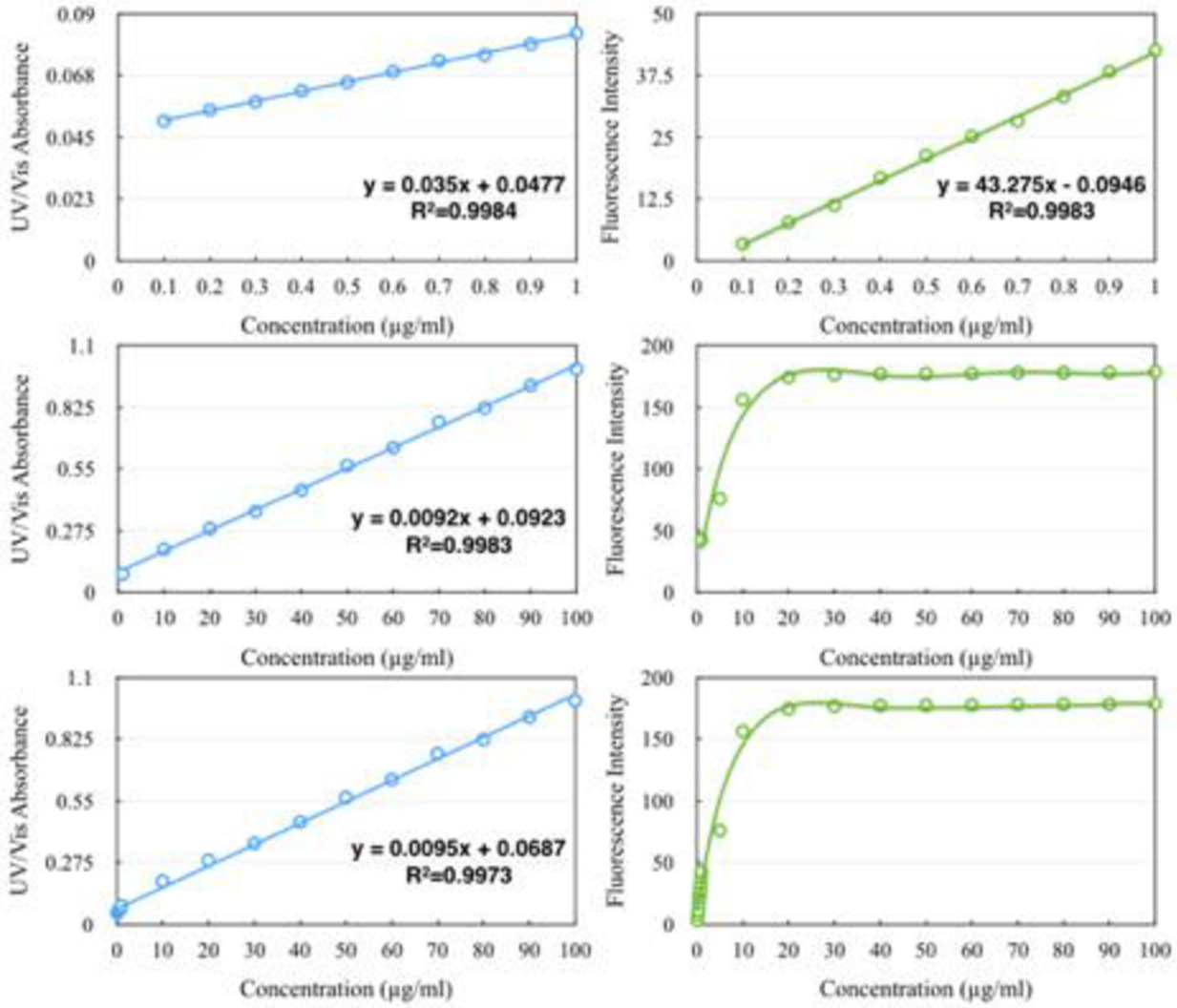

Figure 6.S1 The standard curves showing the dependence of both the UV/Vis absorbance (a, c, e) and the fluorescence intensity (b, d, f) of Dox on its concentration over a range from 0.1 to 1 μg/ml (a, b), 1 to 100 μg/ml (c, d), and 0.1 to 100 μg/ml (e, f).

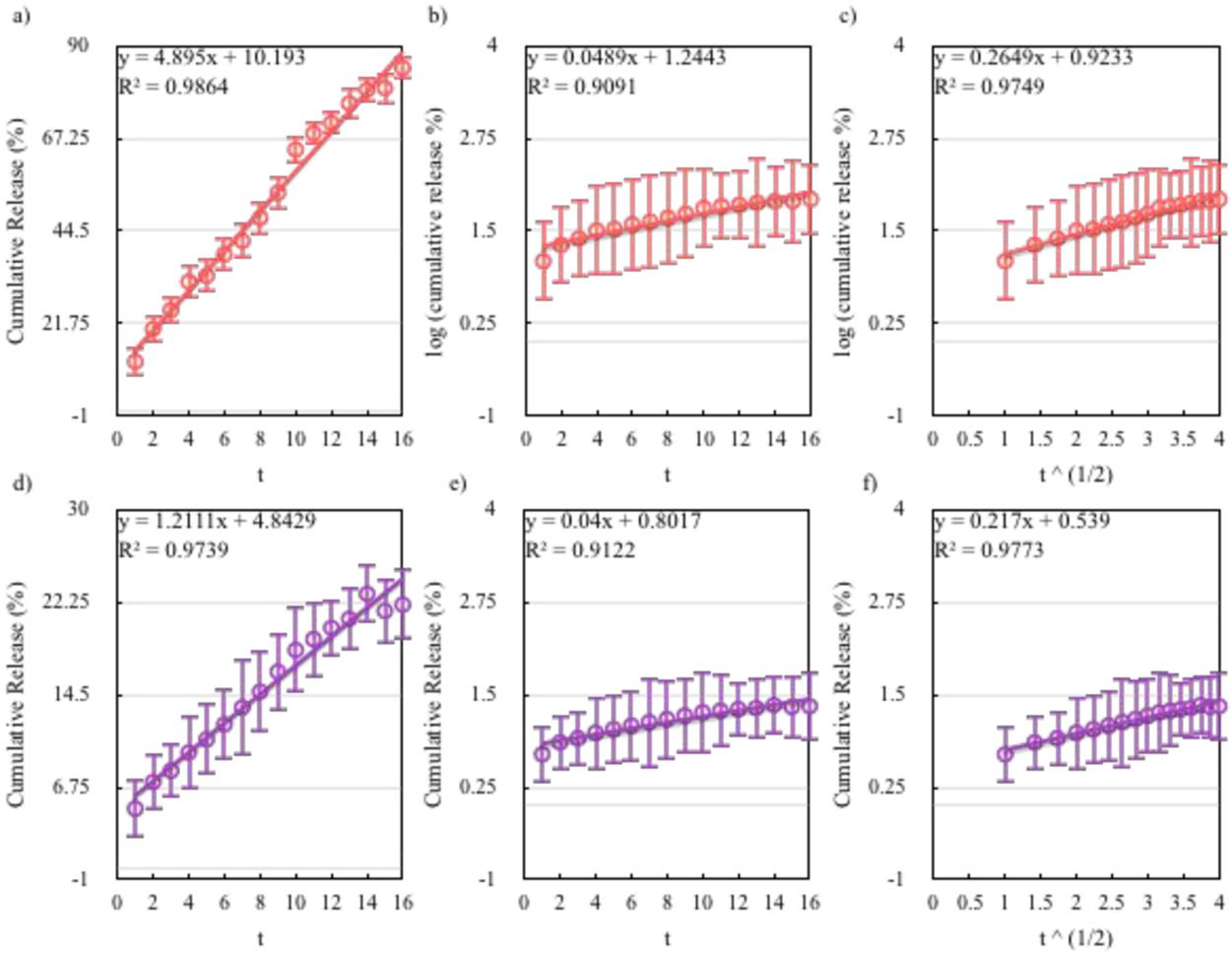

Figure 6.S2 The fitted data of the released Dox from the poly(NIPAM-b-AAc)-shelled, Dox-loaded MBs at 37 (a, b, c) and 39 °C (d, e, f) using zero order kinetic (a, d), first order kinetic (b, e), and Higuchi kinetic (c, f) models.

Chapter 7 Conclusions and Contributions

7.1 Major conclusions

This thesis work has three major parts. The first part was to synthesize stabilized proteinaceous MBs using only one single surface treatment of proteins before the synthesis of MBs. The second part was to utilize the synthesized MBs for the potential applications of drug delivery using Dox as a representative chemotherapeutic agent. The third part was to optimize the loading of Dox onto MBs by examining different factors. The major findings and conclusions are summarized and listed below:

1) A novel, facile synthesis of proteinaceous MBs was introduced by using only one single step of the surface treatment of proteins. BSA, used as a model protein, was selected to demonstrate the successful synthesis of BSA-SH MBs. Opposed to the short lifetime of BSA-shelled MBs (a few hours) reported in the literature, the MBs stabilized by the surface-treated BSA were long-lived sustaining their bubble formations for up to several months at 4 °C.

2) Immediately after the synthesis, BSA-SH MBs were observed to be centered at two portions, 0.5 and 2.5 μm. The 0.5 μm portion quickly vanished while the 2.5 μm portion kept shrinking until reaching the critical size of ~850 nm in ~ 3 days after the synthesis due to the Laplace pressure. The different fate between these two portions was attributed to the different surface coverage of thiols rendered during the surface treatment stage. At

20 times molar excess of the Traut's reagent, the long-lived 2.5 μm portion was the greatest in number and therefore 20 times molar excess was determined to be the optimal dosage of the Traut's reagent for the MBs stabilization.

3) Characterizations of BSA-SH MBs by FTIR and XPS indicated the presence of free unbound thiols, carboxylic, and primary amines on their surface, implying the possibility of further surface modification.

4) In QCM-D tests, the reactivities of the carboxylic and amine groups of BSA-SH MBs were indirectly testified through electrostatic attachments onto the alumina, and the surface thiol groups was directly proved by reacting with the gold sensor. With these reactive functional groups on their surfaces, BSA-SH MBs could be used to load drug molecules through either bond formation or electrostatic interactions. Alternatively, BSA-SH MBs could be directly used to remove metal nanoparticles from wastewater through column flotation.

5) To demonstrate the potential application of drug delivery using BSA-SH MBs, Dox, as a model drug, was electrostatically loaded onto the MBs and then further encapsulated by a temperature-sensitive polymer, poly(NIPAM-b-AAc). The LCST of the polymer shell was fine-tuned to be 39 °C by copolymerizing NIPAM and AAc (25:1, mol/mol). Based on the IVRT, the temperature-responsiveness of poly(NIPAM-b-AAc)-shelled, Dox-loaded MBs was shown when heating from the body temperature 37 °C to 39 °C; the cumulative release of Dox was elevated from ~20 to ~90% over a period of 18 hrs.

6) In addition to the temperature-responsiveness, the implementation of the polymer shell renders an excellent retention of Dox from MBs at the room temperature of 23 °C without leaking any appreciable amount of Dox over the examined period of 40 hrs. In comparison, the shell-free, Dox-loaded MBs showed a poor retention of Dox, releasing ~75% within 8 hrs to the IVRT media.

7) The successive loadings of Dox and poly(NIPAM-b-AAc) onto MBs were confirmed by SEM imaging, CLSM imaging, zeta potential measurement, FTIR, and QCM-D.

8) As AuNPs were reported to have a great affinity to Dox in the literature, the loading efficiencies of Dox on MBs were compared by using AuNPs as an intermediate layer from UV/Vis and fluorescent spectrophotometric measurements and found out to be higher when Dox was directly loaded onto the bare MBs. Other contributing factors were also investigated such as pH, the dosage of MBs, and temperature.

9) Based on the kinetic study, the release of Dox from the poly(NIPAM-b-AAc)-shelled MBs follows the Korsmeyer-Peppas model, where the Fickian diffusion and the conformational change of the polymer shell collectively regulate the release of Dox.

7.2 Contributions to the original knowledge

The short lifetime of proteinaceous MBs produced by conventional ultrasonic methods has been hindering their applications in many fields such as drug delivery and water purification. The

commercially available MBs mostly rely on either perfluorocarbon as the internal gas core or a certain type of proteins for stabilization. In the previous studies by other researchers, protein treatment by either chemical or physical denaturation was more often to be restricted to certain types of proteins. This work, on the other hand, introduced a facile, universal method of synthesizing proteinaceous MBs using only one single surface treatment, opening the routes for further studies and applications of proteinaceous MBs. The possibilities of using the synthesized MBs as a drug carrier were demonstrated by loading Dox onto the surface of MBs and subsequently encapsulated by a temperature sensitive shell. The drug retention and temperature responsiveness were both well represented.

Chapter 8 Future Work

8.1 Suggestions for Future work

1) The reactivities of several key functional groups were demonstrated in the current study, and further applications of using the synthesized MBs to collect metal nanoparticles or metal ions could be systematically investigated as a future work.

2) For the acoustic characterization, we were only managed to measure the attenuation coefficient at 3.3 MHz due to the limitation of our ultrasound transducer. If one or more transducers with a broad frequency range and strong backscattering response become available, we can start to measure the attenuation and backscattering response at high frequency. The attenuation and backscattering responses with respect to different

magnitudes of frequency are crucial eventually determining the application of using our synthesized MBs as an ultrasound contrast enhancer.

3) To demonstrate the universal method introduced in this work, we used BSA as our representative protein because of their unsuccessful synthesis of MBs reported in the literature. However, to be more convincing, other types of proteins could be used to synthesize different proteinaceous MBs. As a cross-check, their lifetime and surface reactivities could be probed as well to compare their performance to that of BSA-SH MBs.

4) The loading of Dox onto MBs was carried out through electrostatic interactions in our study; however, cross-linkers could be used instead to anchor Dox onto the surface of MBs. The cross-linkers could also be designed to be stimulus responsive. For example, tumor cells have more acidic pH environment than healthy tissue cells, and the release of Dox could be governed by pH-sensitive cross-linkers. Other site-specific releases of Dox could also be facilitated using ultrasound as a stimulus when the acoustic characterization of our MBs becomes available.

5) AFM studies of the successive loadings of Dox and poly(NIPAM-b-AAc) onto MBs could be carried out to gain the molecular-level understanding of the mechanism. In this work, we studied the interactions by optimizing different contributing factors and drew the preliminary conclusion. If Dox molecules could be anchored onto a modified AFM tip, then its interaction with MBs could be revealed using AFM studies. Analogously, the

interaction between the polymer shell and the Dox-loaded MBs could be also studied using similar setups in AFM studies.

6) The cellular toxicity and the in-vivo Dox distribution of the Dox-loaded MBs could be the next stage of our studies. To probe the in-vivo performance of the Dox-loaded MBs, different cancer cell lines could be introduced to react with these MBs under different conditions and visualized using fluorescent CLSM.

Bibliography

Abràmoff, M.D., P.J. Magalhães, and S.J. Ram, Image processing with ImageJ. Biophotonics international, 2004. 11(7): 36-42.

Amendola, V. and M. Meneghetti, Size evaluation of gold nanoparticles by UV− vis spectroscopy. The Journal of Physical Chemistry C, 2009. 113(11): 4277-4285.

Azmin, M., et al., Dissolution of coated microbubbles: the effect of nanoparticles and surfactant concentration. Materials Science and Engineering: C, 2012. 32(8): 2654-2658.

Bain, C.D., H.A. Biebuyck, and G.M. Whitesides, Comparison of self-assembled monolayers on gold: coadsorption of thiols and disulfides. Langmuir, 1989. 5(3): 723-727.

Barak, M. and Y. Katz, Microbubbles - Pathophysiology and clinical implications. Chest, 2005. 128(4): 2918-2932.

Barth, A., The infrared absorption of amino acid side chains. Progress in biophysics and molecular biology, 2000. 74(3): 141-173.

Binks, B.P., Modern aspects of emulsion science. 1998: Royal Society of Chemistry.

Blomley, M. and D. Cosgrove, Microbubble echo-enhancers: a new direction for ultrasound? The Lancet, 1997. 349(9069): 1855-1856.

Borden, M.A., et al., DNA and polylysine adsorption and multilayer construction onto cationic lipid-coated microbubbles. Langmuir, 2007. **23**(18): 9401-9408.

Brismar, T.B., et al., Magnetite nanoparticles can be coupled to microbubbles to support multimodal imaging. Biomacromolecules, 2012. **13**(5): 1390-1399.

Cai, W. and X. Chen, Multimodality molecular imaging of tumor angiogenesis. Journal of Nuclear Medicine, 2008. **49**(Suppl 2): 113S-128S.

Calliada, F., et al., *Ultrasound contrast agents: basic principles*. European journal of radiology, 1998. **27**: S157-S160.

Camarozano, A.C., et al., Effects of microbubbles and ultrasound on the microcirculation: observation on the hamster cheek pouch. Journal of the American Society of Echocardiography, 2010. 23(12): 1323-1330.

Castner, D.G., K. Hinds, and D.W. Grainger, X-ray photoelectron spectroscopy sulfur 2p study of organic thiol and disulfide binding interactions with gold surfaces. Langmuir, 1996. 12(21): 5083-5086.

Cavalieri, F., et al., *Antimicrobial and biosensing ultrasound-responsive lysozyme-shelled microbubbles.* ACS applied materials & interfaces, 2013. **5**(2): 464-471.

Cavalieri, F., et al., One-pot ultrasonic synthesis of multifunctional microbubbles and microcapsules using synthetic thiolated macromolecules. Chemical Communications, 2011. 47(14): 4096-4098.

Cavalieri, F., et al., Ultrasonic synthesis of stable, functional lysozyme microbubbles. Langmuir, 2008. 24(18): 10078-10083.

Chatterjee, D. and K. Sarkar, A Newtonian rheological model for the interface of microbubble contrast agents. Ultrasound in Medicine and Biology, 2003. 29(12): 1749-1757.

Cherry, S.R. Multimodality imaging: Beyond pet/ct and spect/ct. in Seminars in nuclear medicine. 2009. Elsevier.

Chomas, J.E., et al., Mechanisms of contrast agent destruction. IEEE transactions on ultrasonics, ferroelectrics, and frequency control, 2001. 48(1): 232-248.

Christiansen, C., et al., *Physical and biochemical characterization of Albunex, a new ultrasound contrast agent consisting of air-filled albumin microspheres suspended in a solution of human albumin.* Biotechnology and applied biochemistry, 1994. **19**(3): 307-320.

Christiansen, J.P., et al., Targeted tissue transfection with ultrasound destruction of plasmid-bearing cationic microbubbles. Ultrasound in medicine & biology, 2003. 29(12): 1759-1767.

Clark, A., et al., ELECTRON MICROSCOPY OF NETWORK STRUCTURES IN THERMALLY-INDUCED GLOBULAR PROTEIN GELS. International Journal of Peptide and Protein Research, 1981. 17(3): 380-392.

Cochran, M.C., et al., Doxorubicin and paclitaxel loaded microbubbles for ultrasound triggered drug delivery. International journal of pharmaceutics, 2011. **414**(1): 161-170.

Cosgrove, D. and C. Harvey, Clinical uses of microbubbles in diagnosis and treatment. Medical & biological engineering & computing, 2009. 47(8): 813-826.

Cosgrove, D., *Echo enhancers and ultrasound imaging.* European journal of radiology, 1997. **26**(1): 64-76.

Curry, D., et al., Adsorption of doxorubicin on citrate-capped gold nanoparticles: insights into engineering potent chemotherapeutic delivery systems. Nanoscale, 2015. 7(46): 19611-19619.

Dai, X., et al., Fluorescence intensity and lifetime imaging of free and micellar-encapsulated doxorubicin in living cells. Nanomedicine: Nanotechnology, Biology and Medicine, 2008. 4(1): 49-56.

Dash, S., et al., Kinetic modeling on drug release from controlled drug delivery systems. Acta Pol Pharm, 2010. 67(3): 217-23.

Dayton, P., et al., Acoustic radiation force in vivo: a mechanism to assist targeting of microbubbles. Ultrasound in medicine & biology, 1999. **25**(8): 1195-1201.

De Cock, I., et al., Sonoprinting and the importance of microbubble loading for the ultrasound mediated cellular delivery of nanoparticles. Biomaterials, 2016. 83: 294-307.

De Jong, N., et al., Absorption and scatter of encapsulated gas filled microspheres: theoretical considerations and some measurements. Ultrasonics, 1992. 30(2): 95-103.

De Jong, N., et al., Ultrasonic characterization of ultrasound contrast agents. Medical & biological engineering & computing, 2009. 47(8): 861-873.

Deligöz, H. and B. Tieke, QCM-D study of layer-by-layer assembly of polyelectrolyte blend films and their drug loading-release behavior. Colloids and Surfaces A: Physicochemical and Engineering Aspects, 2014. **441**: 725-736.

Desiraju, G.R. and T. Steiner, The weak hydrogen bond: in structural chemistry and biology. Vol. 9. 2001: Oxford University Press on Demand.

Dressaire, E., et al., *Interfacial polygonal nanopatterning of stable microbubbles.* Science, 2008. **320**(5880): 1198-1201.

Du, Z., et al., Outstanding stability of particle-stabilized bubbles. Langmuir, 2003. 19(8): 3106-3108.

Duncan, P.B. and D. Needham, *Test of the Epstein-Plesset model for gas microparticle dissolution in aqueous media: Effect of surface tension and gas undersaturation in solution.* Langmuir, 2004. **20**(7): 2567-2578.

Eby, D.M., et al., Probing the molecular structure of antimicrobial peptide-mediated silica condensation using X-ray photoelectron spectroscopy. Journal of Materials Chemistry, 2012. 22(19): 9875-9883.

Ekemen, Z., et al., Electrohydrodynamic bubbling: an alternative route to fabricate porous structures of silk fibroin based materials. Biomacromolecules, 2013. 14(5): 1412-1422.

Elbialy, N.S., M.M. Fathy, and W.M. Khalil, Preparation and characterization of magnetic gold nanoparticles to be used as doxorubicin nanocarriers. Physica Medica, 2014. 30(7): 843-848.

Epstein, c.e.P. and M.S. Plesset, On the Stability of Gas Bubbles in Liquid-Gas Solutions. The Journal of Chemical Physics, 1950. 18(11): 1505-1509.

Farook, U., et al., Preparation of microbubble suspensions by co-axial electrohydrodynamic atomization. Medical engineering & physics, 2007. 29(7): 749-754.

Farooqi, Z.H., et al., Stability of poly (N-isopropylacrylamide-co-acrylic acid) polymer microgels under various conditions of temperature, pH and salt concentration. Arabian Journal of Chemistry, 2013.

Farooqi, Z.H., et al., Synthesis, characterization and fabrication of copper nanoparticles in N-isopropylacrylamide based co-polymer microgels for degradation of p-nitrophenol. Materials Science-Poland, 2015. **33**(1): 185-192.

Ferrara, K., R. Pollard, and M. Borden, Ultrasound microbubble contrast agents: fundamentals and application to gene and drug delivery. Biomedical Engineering, 2007. **9**.

Ferrara, K.W., M.A. Borden, and H. Zhang, Lipid-shelled vehicles: engineering for ultrasound molecular imaging and drug delivery. Accounts of chemical research, 2009. **42**(7): 881-892.

Feshitan, J.A., et al., Microbubble size isolation by differential centrifugation. Journal of colloid and interface science, 2009. **329**(2): 316-324.

Fornari, F.A., et al., Interference by doxorubicin with DNA unwinding in MCF-7 breast tumor cells. Molecular pharmacology, 1994. **45**(4): 649-656.

Forsberg, F., W.T. Shi, and B. Goldberg, *Subharmonic imaging of contrast agents.* Ultrasonics, 2000. **38**(1): 93-98.

Frens, G., Controlled nucleation for the regulation of the particle size in monodisperse gold suspensions. Nature, 1973. 241(105): 20-22.

Galaev, I. and B. Mattiasson, Smart polymers: applications in biotechnology and biomedicine. 2007: CRC Press.

Gazzera, L., et al., Design of Highly Stable Echogenic Microbubbles through Controlled Assembly of Their Hydrophobin Shell. Angewandte Chemie, 2016. 128(35): 10419-10423.

Gedanken, A., Preparation and properties of proteinaceous microspheres made sonochemically. Chemistry–A European Journal, 2008. 14(13): 3840-3853.

Geers, B., et al., *Crucial factors and emerging concepts in ultrasound-triggered drug delivery.* Journal of controlled release, 2012. **164**(3): 248-255.

Giljohann, D.A., et al., *Gold nanoparticles for biology and medicine.* Angewandte Chemie International Edition, 2010. 49(19): 3280-3294.

Goldstein, J., et al., Scanning electron microscopy and X-ray microanalysis: a text for biologists, materials scientists, and geologists. 2012: Springer Science & Business Media.

Graf, K. and M. Kappl, Physics and chemistry of interfaces. 2006: John Wiley & Sons.

Grinstaff, M.W. and K.S. Suslick, Air-filled proteinaceous microbubbles: synthesis of an echo-contrast agent. Proceedings of the National Academy of Sciences, 1991. 88(17): 7708-7710.

Grönbeck, H., A. Curioni, and W. Andreoni, Thiols and disulfides on the Au (111) surface: The headgroup-gold interaction. Journal of the American Chemical Society, 2000. 122(16): 3839-3842.

Haiss, W., et al., Determination of size and concentration of gold nanoparticles from UV-vis spectra. Analytical chemistry, 2007. 79(11): 4215-4221.

Häkkinen, H., The gold-sulfur interface at the nanoscale. Nature chemistry, 2012. 4(6): 443-455.

Hayat, M.A., Principles and techniques of scanning electron microscopy. Biological applications. Volume 1. 1974: Van Nostrand Reinhold Company.

Heath, G.R., et al., Self-assembly of actin scaffolds on lipid microbubbles. Soft matter, 2014. 10(5): 694-700.

Hernot, S. and A.L. Klibanov, Microbubbles in ultrasound-triggered drug and gene delivery. Advanced drug delivery reviews, 2008. 60(10): 1153-1166.

Hortobagyi, G., Anthracyclines in the treatment of cancer. Drugs, 1997. **54**(4): 1-7.

Huang, B.X., H.-Y. Kim, and C. Dass, Probing three-dimensional structure of bovine serum albumin by chemical cross-linking and mass spectrometry. Journal of the American Society for Mass Spectrometry, 2004. 15(8): 1237-1247.

Ingle Jr, J.D. and S.R. Crouch, Spectrochemical analysis. 1988.

Instituion, S.R.E. Selective Permeability of Dialysis Tubing Lab Explained. [cited 2016 Dec. 31].

Ishida, T., et al., High resolution X-ray photoelectron spectroscopy measurements of octadecanethiol self-assembled monolayers on Au (111). Langmuir, 1998. 14(8): 2092-2096.

Ishikawa, H., et al., Inactivation of Bacillus spores by the supercritical carbon dioxide micro-bubble method. Bioscience, biotechnology, and biochemistry, 1997. 61(6): 1022-1023.

Jadzinsky, P.D., et al., Structure of a thiol monolayer-protected gold nanoparticle at 1.1 Å resolution. Science, 2007. 318(5849): 430-433.

Janib, S.M., A.S. Moses, and J.A. MacKay, Imaging and drug delivery using theranostic nanoparticles. Advanced drug delivery reviews, 2010. **62**(11): 1052-1063.

Janshoff, A., H.J. Galla, and C. Steinem, Piezoelectric Mass-Sensing Devices as Biosensors—An Alternative to Optical Biosensors? Angewandte Chemie International Edition, 2000. 39(22): 4004-4032.

Jue, R., et al., Addition of sulfhydryl groups of Escherichia coli ribosomes by protein modification with 2-iminothiolane (methyl 4-mercaptobutyrimidate). Biochemistry, 1978. 17(25): 5399-5406.

Júnior, J.A.A. and J.B. Baldo, The behavior of zeta potential of silica suspensions. New Journal of Glass and Ceramics, 2014. 4(02): 29.

Kabalnov, A., et al., Dissolution of multicomponent microbubbles in the bloodstream: 1. Theory. Ultrasound in medicine & biology, 1998. 24(5): 739-749.

Kaya, M. and P.A. Dayton, Changes in lipid-encapsulated microbubble population during continuous infusion and methods to maintain consistency. Ultrasound in medicine & biology, 2009. **35**(10): 1748-1755.

Kayal, S. and R. Ramanujan, Doxorubicin loaded PVA coated iron oxide nanoparticles for targeted drug delivery. Materials Science and Engineering: C, 2010. **30**(3): 484-490.

Keizer, H., et al., Doxorubicin (adriamycin): a critical review of free radical-dependent mechanisms of cytotoxicity. Pharmacology & therapeutics, 1990. **47**(2): p. 219-231.

Kiessling, F., et al., Ultrasound microbubbles for molecular diagnosis, therapy, and theranostics. Journal of nuclear medicine, 2012. 53(3): 345-348.

Kimling, J., et al., Turkevich method for gold nanoparticle synthesis revisited. The Journal of Physical Chemistry B, 2006. 110(32): 15700-15707.

Klibanov, A.L., Ligand-carrying gas-filled microbubbles: ultrasound contrast agents for targeted molecular imaging. Bioconjugate chemistry, 2005. 16(1): 9-17.

Kloek, W., T. van Vliet, and M. Meinders, Effect of bulk and interfacial rheological properties on bubble dissolution. Journal of Colloid and Interface Science, 2001. 237(2): 158-166.

Kobayashi, F., et al., Inactivation of Escherichia coli by CO2 microbubbles at a lower pressure and near room temperature. Transactions of the ASABE, 2009. 52(5): p. 1621-1626.

Koros, W., Y. Ma, and T. Shimidzu, Terminology for membranes and membrane processes. J. Membr. Sci, 1996. 120(2): 149-159.

Kosmulski, M., Chemical properties of material surfaces. Vol. 102. 2001: CRC press.

Krishna, P.D. and V.L. Newhouse, Second harmonic characteristics of the ultrasound contrast agents Albunex and FSO69. Ultrasound in medicine & biology, 1997. 23(3): 453-459.

Lajoinie, G., et al., In vitro methods to study bubble-cell interactions: Fundamentals and therapeutic applications. Biomicrofluidics, 2016. 10(1): 011501.

Lemlich, R., Prediction of changes in bubble size distribution due to interbubble gas diffusion in foam. Industrial & Engineering Chemistry Fundamentals, 1978. 17(2): 89-93.

Lentacker, I., et al., Design and evaluation of doxorubicin-containing microbubbles for ultrasound-triggered doxorubicin delivery: cytotoxicity and mechanisms involved. Molecular Therapy, 2010. **18**(1): 101-108.

Lentacker, I., et al., *Ultrasound-responsive polymer-coated microbubbles that bind and protect DNA*. Langmuir, 2006. **22**(17): 7273-7278.

Lentacker, I., S.C. De Smedt, and N.N. Sanders, Drug loaded microbubble design for ultrasound triggered delivery. Soft Matter, 2009. **5**(11): 2161-2170.

Leong-Poi, H., et al., Therapeutic arteriogenesis by ultrasound-mediated VEGF165 plasmid gene delivery to chronically ischemic skeletal muscle. Circulation research, 2007. **101**(3): 295-303.

Li, T., et al., Characterization of floc size, strength and structure under various coagulation mechanisms. Powder technology, 2006. 168(2): 104-110.

Lindner, J.R., Microbubbles in medical imaging: current applications and future directions. Nature Reviews Drug Discovery, 2004. **3**(6): 527-533.

Lue, S.J., C.-H. Chen, and C.-M. Shih, Tuning of lower critical solution temperature (LCST) of poly (N-isopropylacrylamide-co-acrylic acid) hydrogels. Journal of Macromolecular Science, Part B, 2011. **50**(3): 563-579.

Lum, A.F., et al., Ultrasound radiation force enables targeted deposition of model drug carriers loaded on microbubbles. Journal of controlled release, 2006. **111**(1): 128-134.

Ma, X., Bussonniere, A., & Liu, Q. (2017). A facile sonochemical synthesis of shell-stabilized reactive microbubbles using surface-thiolated bovine serum albumin with the Traut's reagent. *Ultrasonics Sonochemistry*, *36*, 454-465.

Mahalingam, S., et al., Formation of protein and protein–gold nanoparticle stabilized microbubbles by pressurized gyration. Langmuir, 2014. 31(2): 659-666.

Mahalingam, S., M. Meinders, and M. Edirisinghe, Formation, stability, and mechanical properties of bovine serum albumin stabilized air bubbles produced using coaxial electrohydrodynamic atomization. Langmuir, 2014. 30(23): 6694-6703.

Martin, K.H. and P.A. Dayton, *Current status and prospects for microbubbles in ultrasound theranostics*. Wiley Interdisciplinary Reviews: Nanomedicine and Nanobiotechnology, 2013. **5**(4): 329-345.

Maske, S.K., et al., INTERNATIONAL JOURNAL OF PHARMACY & LIFE SCIENCES. Int. J. of Pharm. & Life Sci.(IJPLS), 2012. 3(12): 2228-2235.

Masuda, N., et al., Influence of microbubbles on free radical generation by ultrasound in aqueous solution: dependence of ultrasound frequency. The Journal of Physical Chemistry B, 2015. 119(40): 12887-12893.

McClellan, S.J. and E.I. Franses, Effect of concentration and denaturation on adsorption and surface tension of bovine serum albumin. Colloids and Surfaces B: Biointerfaces, 2003. 28(1): 63-75.

McEwan, C., et al., Oxygen carrying microbubbles for enhanced sonodynamic therapy of hypoxic tumours. Journal of Controlled Release, 2015. 203: 51-56.

Meinders, M.B. and T. van Vliet, The role of interfacial rheological properties on Ostwald ripening in emulsions. Advances in colloid and interface science, 2004. 108: 119-126.

Mejac, I., et al., Visualizing the Lower Critical Solution Temperature Phase Transition of Individual Poly (Nipam)-Based Hydrogel Particles Using Near-Infrared Multispectral Imaging Microscopy. Analytical chemistry, 2010. **82**(5): 1698-1704.

Mhlanga, N., et al., Polylactide-based Magnetic Spheres as Efficient Carriers for Anticancer Drug Delivery. ACS applied materials & interfaces, 2015. **7**(40): 22692-22701.

Mirza, A.Z. and H. Shamshad, Preparation and characterization of doxorubicin functionalized gold nanoparticles. European journal of medicinal chemistry, 2011. 46(5): 1857-1860.

Mohamedi, G., et al., Effects of gold nanoparticles on the stability of microbubbles. Langmuir, 2012. 28(39): 13808-13815.

Mohan, P. and N. Rapoport, Doxorubicin as a molecular nanotheranostic agent: effect of doxorubicin encapsulation in micelles or nanoemulsions on the ultrasound-mediated intracellular delivery and nuclear trafficking. Molecular pharmaceutics, 2010. 7(6): 1959-1973.

Momparler, R.L., et al., Effect of adriamycin on DNA, RNA, and protein synthesis in cell-free systems and intact cells. Cancer research, 1976. **36**(8): 2891-2895.

Mulvagh, S.L., et al., Contrast echocardiography: current and future applications. Journal of the American Society of Echocardiography, 2000. 13(4): 331-342.

Mura, S., J. Nicolas, and P. Couvreur, Stimuli-responsive nanocarriers for drug delivery. Nature materials, 2013. **12**(11): 991-1003.

Nazari, A.M., P.W. Cox, and K.E. Waters, Copper ion removal from dilute solutions using ultrasonically synthesised BSA-and EWP-coated air bubbles. Separation and Purification Technology, 2014. 132: 218-225.

Nemati, F., et al., Some parameters influencing cytotoxicity of free doxorubicin and doxorubicin-loaded nanoparticles in sensitive and multidrug resistant leucemic murine cells: incubation time, number of nanoparticles per cell. International journal of pharmaceutics, 1994. **102**(1-3): 55-62.

Nigam, S., K. Barick, and D. Bahadur, Development of citrate-stabilized Fe_3O_4 nanoparticles: conjugation and release of doxorubicin for therapeutic applications. Journal of Magnetism and Magnetic Materials, 2011. 323(2): 237-243.

Pang, B., et al., Drug-induced histone eviction from open chromatin contributes to the chemotherapeutic effects of doxorubicin. Nature communications, 2013. **4**: 1908.

Park, J.I., et al., *Microbubbles loaded with nanoparticles: a route to multiple imaging modalities.* Acs Nano, 2010. **4**(11): p. 6579-6586.

Parks, G.A., The isoelectric points of solid oxides, solid hydroxides, and aqueous hydroxo complex systems. Chemical Reviews, 1965. 65(2): 177-198.

Perelman, L.A., et al., Preparation and Characterization of a pH-and Thermally Responsive Poly (N-isopropylacrylamide-co-acrylic acid)/Porous SiO2 Hybrid. Advanced functional materials, 2010. **20**(5): 826-833.

Perkampus, H.-H., H.-C. Grinter, and T. Threlfall, UV-VIS Spectroscopy and its Applications. 1992: Springer.

Peyman, S.A., et al., Expanding 3D geometry for enhanced on-chip microbubble production and single step formation of liposome modified microbubbles. Lab on a Chip, 2012. 12(21): 4544-4552.

Phan, H.T., et al., Investigation of bovine serum albumin (BSA) attachment onto self-assembled monolayers (SAMs) using combinatorial quartz crystal microbalance with dissipation (QCM-D) and spectroscopic ellipsometry (SE). PloS one, 2015. 10(10): e0141282.

Qin, S., C.F. Caskey, and K.W. Ferrara, Ultrasound contrast microbubbles in imaging and therapy: physical principles and engineering. Physics in medicine and biology, 2009. 54(6): R27.

Qiu, F., et al., Real-time monitoring of anticancer drug release with highly fluorescent star-conjugated copolymer as a drug carrier. Biomacromolecules, 2014. 15(4): 1355-1364.

Quaia, E., Microbubble ultrasound contrast agents: an update. European radiology, 2007. **17**(8): 1995-2008.

Rajan, Y.C., B.S. Inbaraj, and B.H. Chen, Synthesis and characterization of poly (γ-glutamic acid)-based alumina nanoparticles with their protein adsorption efficiency and cytotoxicity towards human prostate cancer cells. RSC Advances, 2015. 5(20): 15126-15139.

Rapoport, N., Z. Gao, and A. Kennedy, Multifunctional nanoparticles for combining ultrasonic tumor imaging and targeted chemotherapy. Journal of the National Cancer Institute, 2007. **99**(14): 1095-1106.

Raymond, J.L., et al., Broadband attenuation measurements of phospholipid-shelled ultrasound contrast agents. Ultrasound in medicine & biology, 2014. 40(2): 410-421.

Reimhult, E., et al., Simultaneous surface plasmon resonance and quartz crystal microbalance with dissipation monitoring measurements of biomolecular adsorption events involving structural transformations and variations in coupled water. Analytical chemistry, 2004. 76(24): 7211-7220.

Rezwan, K., et al., Bovine serum albumin adsorption onto colloidal Al2O3 particles: A new model based on Zeta potential and UV-Vis measurements. Langmuir, 2004. 20(23): 10055-10061.

Ritger, P.L. and N.A. Peppas, A simple equation for description of solute release I. Fickian and non-Fickian release from non-swellable devices in the form of slabs, spheres, cylinders or discs. Journal of controlled release, 1987. 5(1): 23-36.

Rodahl, M., et al., Quartz crystal microbalance setup for frequency and Q-factor measurements in gaseous and liquid environments. Review of Scientific Instruments, 1995. 66(7): 3924-3930.

Rodahl, M., F. Höök, and B. Kasemo, QCM operation in liquids: an explanation of measured variations in frequency and Q factor with liquid conductivity. Analytical Chemistry, 1996. 68(13): 2219-2227.

Rovers, T.A., et al., Temperature is key to yield and stability of BSA stabilized microbubbles. Food Hydrocolloids, 2016. 52: 106-115.

Samah, N.H.A. and C.M. Heard, Enhanced in vitro transdermal delivery of caffeine using a temperature-and pH-sensitive nanogel, poly (NIPAM-co-AAc). International journal of pharmaceutics, 2013. **453**(2): 630-640.

Sandison, D.R., et al., Quantitative fluorescence confocal laser scanning microscopy (CLSM), in Handbook of biological confocal microscopy. 1995, Springer. 39-53.

Sanson, C., et al., A simple method to achieve high doxorubicin loading in biodegradable polymersomes. Journal of Controlled Release, 2010. 147(3): 428-435.

Sauerbrey, G., Verwendung von Schwingquarzen zur Wägung dünner Schichten und zur Mikrowägung. Zeitschrift für physik, 1959. 155(2): 206-222.

Schutt, E.G., et al., Injectable microbubbles as contrast agents for diagnostic ultrasound imaging: the key role of perfluorochemicals. Angewandte Chemie International Edition, 2003. 42(28): 3218-3235.

Shchukina, E.M. and D.G. Shchukin, LbL coated microcapsules for delivering lipid-based drugs. Advanced drug delivery reviews, 2011. **63**(9): 837-846.

Shuai, X., et al., Micellar carriers based on block copolymers of poly (ε-caprolactone) and poly (ethylene glycol) for doxorubicin delivery. Journal of Controlled Release, 2004. 98(3): 415-426.

Singhvi, G. and M. Singh, Review: in-vitro drug release characterization models. Int J Pharm Stud Res, 2011. 2(1): 77-84.

Sirsi, S. and M. Borden, Microbubble compositions, properties and biomedical applications. Bubble Science, Engineering & Technology, 2009. **1**(1-2): 3-17.

Sirsi, S., et al., Lung surfactant microbubbles. Soft Matter, 2009. 5(23): 4835-4842.

Sirsi, S.R. and M.A. Borden, Advances in ultrasound mediated gene therapy using microbubble contrast agents. Theranostics, 2012. 2(12): 1208-1222.

Socrates, G., Infrared and Raman characteristic group frequencies: tables and charts. 2004: John Wiley & Sons.

Spencer, S.S., The relative contributions of MRI, SPECT, and PET imaging in epilepsy. Epilepsia, 1994. 35(s6): S72-S89.

Sprycha, R., Electrical double layer at alumina/electrolyte interface: I. Surface charge and zeta potential. Journal of colloid and interface science, 1989. 127(1): 1-11.

Stewart, J.E., Vibrational spectra of primary and secondary aliphatic amines. The Journal of Chemical Physics, 1959. 30(5): 1259-1265.

Storhoff, J.J., et al., One-pot colorimetric differentiation of polynucleotides with single base imperfections using gold nanoparticle probes. Journal of the American Chemical Society, 1998. 120(9): 1959-1964.

Subedi, R.K., K.W. Kang, and H.-K. Choi, Preparation and characterization of solid lipid nanoparticles loaded with doxorubicin. European journal of pharmaceutical sciences, 2009. 37(3): 508-513.

Subramaniam, A.B., et al., Colloid science: Non-spherical bubbles. Nature, 2005. 438(7070): 930-930.

Suslick, K.S., Sonochemistry. science, 1990. 247(4949): 1439-1445.

Suslick, K.S., Ultrasound: its chemical, physical, and biological effects. 1988: VCH Publishers.

Swinehart, D., The beer-lambert law. J. Chem. Educ, 1962. 39(7): 333.

Takeda, K., et al., Conformational change of bovine serum albumin by heat treatment. Journal of protein chemistry, 1989. 8(5): p. 653-659.

Talu, E., et al., Long-term stability by lipid coating monodisperse microbubbles formed by a flow-focusing device. Langmuir, 2006. 22(23): 9487-9490.

Talu, E., Lipid-stabilized monodisperse microbubbles produced by flow focusing for use as ultrasound contrast agents and targeted drug delivery. 2007: ProQuest.

Tarbell, D., The mechanism of oxidation of thiols to disulfides. Organic sulfur compounds, 1961. 1: 97-102.

Taylor, P., Ostwald ripening in emulsions. Advances in colloid and interface science, 1998. 75(2): 107-163.

Thomsen, H., *Contrast Media in Ultrasonography Basic Principles and Clinical Applications.* 2005.

Thomson, L.M., et al., Manufacture of concentrated, lipid-based oxygen microbubble emulsions by high shear homogenization and serial concentration. Journal of visualized experiments: JoVE, 2014(87).

Tian, Y., et al., Complexation and release of doxorubicin from its complexes with pluronic P85-b-poly (acrylic acid) block copolymers. Journal of Controlled Release, 2007. 121(3): 137-145.

Ting, C.-Y., et al., Concurrent blood–brain barrier opening and local drug delivery using drug-carrying microbubbles and focused ultrasound for brain glioma treatment. Biomaterials, 2012. **33**(2): 704-712.

Ting, C.-Y., et al., Concurrent blood–brain barrier opening and local drug delivery using drug-carrying microbubbles and focused ultrasound for brain glioma treatment. Biomaterials, 2012. 33(2): 704-712.

Tingaut, P., R. Hauert, and T. Zimmermann, Highly efficient and straightforward functionalization of cellulose films with thiol-ene click chemistry. Journal of Materials Chemistry, 2011. 21(40): 16066-16076.

Touch, V., S. Hayakawa, and K. Saitoh, Relationships between conformational changes and antimicrobial activity of lysozyme upon reduction of its disulfide bonds. Food chemistry, 2004. 84(3): 421-428.

Traut, R.R., et al., Methyl 4-mercaptobutyrimidate as a cleavable crosslinking reagent and its application to the Escherichia coli 30S ribosome. Biochemistry, 1973. 12(17): 3266-3273.

Tripp, B.C., J.J. Magda, and J.D. Andrade, Adsorption of globular proteins at the air/water interface as measured via dynamic surface tension: concentration dependence, mass-transfer considerations, and adsorption kinetics. Journal of colloid and interface science, 1995. 173(1): 16-27.

Trongsatitkul, T. and B.M. Budhlall, Microgels or microcapsules? Role of morphology on the release kinetics of thermoresponsive PNIPAm-co-PEGMa hydrogels. Polymer Chemistry, 2013. 4(5): 1502-1516.

Vaupel, P., F. Kallinowski, and P. Okunieff, Blood flow, oxygen and nutrient supply, and metabolic microenvironment of human tumors: a review. Cancer research, 1989. 49(23): 6449-6465.

Vernon-Parry, K., Scanning electron microscopy: an introduction. III-Vs Review, 2000. 13(4): 40-44.

Villarraga, H.R., et al., Destruction of contrast microbubbles during ultrasound imaging at conventional power output. Journal of the American Society of Echocardiography, 1997. 10(8): 783-791.

Vogi, R. and D. Oreopoulos, Amino acid sequence in bovine serum albumin. Clin. Chim. Acta, 1973. 48: 353.

Voinova, M.V., et al., Viscoelastic acoustic response of layered polymer films at fluid-solid interfaces: continuum mechanics approach. Physica Scripta, 1999. 59(5): 391.

Vong, F., et al., A comparison of the physical properties of ultrasonically synthesized lysozyme- and BSA-shelled microbubbles. Ultrasonics sonochemistry, 2014. 21(1): 23-28.

Wang, S., et al., Doxorubicin induces apoptosis in normal and tumor cells via distinctly different mechanisms intermediacy of H2O2-and p53-dependent pathways. Journal of Biological Chemistry, 2004. **279**(24): 25535-25543.

Weiss, R.B. The anthracyclines: will we ever find a better doxorubicin? in Seminars in oncology. 1992.

Westwood, M., et al., Combined QCMD and AFM studies of lysozyme and poly-l-lysine–poly-galacturonic acid multilayers. Carbohydrate polymers, 2012. **89**(4): 1222-1231.

Xu, Q., et al., A comparative study of microbubble generation by mechanical agitation and sonication. Innovative Food Science & Emerging Technologies, 2008. 9(4): 489-494.

Yamasaki, M., H. Yano, and K. Aoki, Differential scanning calorimetric studies on bovine serum albumin: II. Effects of neutral salts and urea. International journal of biological macromolecules, 1991. 13(6): p. 322-328.

Yang, F., et al., Superparamagnetic iron oxide nanoparticle-embedded encapsulated microbubbles as dual contrast agents of magnetic resonance and ultrasound imaging. Biomaterials, 2009. 30(23): 3882-3890.

Yeh, Y.-C., B. Creran, and V.M. Rotello, Gold nanoparticles: preparation, properties, and applications in bionanotechnology. Nanoscale, 2012. 4(6): 1871-1880.

Yu, B., et al., Functionalized graphene oxide/phosphoramide oligomer hybrids flame retardant prepared via in situ polymerization for improving the fire safety of polypropylene. RSC Advances, 2014. 4(60): 31782-31794.

Yuan, Q., et al., Controlled and extended drug release behavior of chitosan-based nanoparticle carrier. Acta biomaterialia, 2010. **6**(3): 1140-1148.

Zhang, F. and M. Srinivasan, Self-assembled molecular films of aminosilanes and their immobilization capacities. Langmuir, 2004. 20(6): 2309-2314.

Zhang, X., et al., Targeted delivery and controlled release of doxorubicin to cancer cells using modified single wall carbon nanotubes. Biomaterials, 2009. 30(30): 6041-6047.

Zhao, P., N. Li, and D. Astruc, State of the art in gold nanoparticle synthesis. Coordination Chemistry Reviews, 2013. 257(3): 638-665.

Zhou, M., F. Cavalieri, and M. Ashokkumar, Tailoring the properties of ultrasonically synthesised microbubbles. Soft Matter, 2011. 7(2): 623-630.

Zhou, Y., Principles and Applications of Therapeutic Ultrasound in Healthcare. 2015: CRC Press.